

Université Fédérale



Toulouse Midi-Pyrénées

# THÈSE

En vue de l'obtention du

## DOCTORAT DE L'UNIVERSITÉ DE TOULOUSE

Délivré par

Institut National des Sciences Appliquées de Toulouse (INSA de Toulouse)

Discipline ou spécialité :

Dynamique des fluides

---

Présentée et soutenue par

GAO Yanfeng

Le mardi 9 mai 2017

**Titre :**

Inertial Migration of Particles in Microchannel Flows

---

**JURY :**

Jean-Philippe MATAS, Professeur, Université Claude Bernard Lyon 1, Rapporteur

Farzam ZOUESHTIAGH, Professeur, Université de Lille 1, Rapporteur

Jean-Luc ACHARD, Directeur de recherche, Laboratoire des Ecoulements Géophysique et Industriels,  
Examinateur

Stéphane COLIN, Professeur, INSA de Toulouse, Examinateur

Lucien BALDAS, Maître de Conférences, INSA de Toulouse, Directeur de Thèse

Pascale MAGAUD, Maître de Conférences, Université de Limoges, Directrice de Thèse

---

**Ecole doctorale :** Mécanique, Energétique, Génie civil et Procédés (MEGeP)

**Unité de recherche :** Institut Clément Ader (ICA, CNRS UMR 5312)

**Directeur(s) de Thèse :**

Lucien BALDAS, Maître de Conférences, INSA de Toulouse, Directeur de Thèse

Pascale MAGAUD, Maître de Conférences, Université de Limoges, Directrice de Thèse



# Remerciements

Je tiens avant tout à exprimer mes remerciements à mes deux directeurs de thèse, Pascale Magaud et Lucien Baldas, pour la confiance, le temps et la patience qu'ils m'ont prodigués tout au long de ces quatre années. Je remercie en particulier Pascale Magaud pour son accueil, sa bienveillance et son encadrement scientifique (ses conseils pendant les expérimentations et son aide pour développer le programme), et Lucien Baldas pour ses encouragements dans tous les moments difficiles, ses conseils pendant la rédaction du manuscrit et son aide pour réussir ma 1ère publication.

J'exprime ensuite mes remerciements à M. Stéphane Colin, Professeur à l'INSA de Toulouse qui a accepté de présider mon jury de thèse. Je le remercie par ailleurs pour son enseignement enrichissant sur la microfluidique, son accueil et son encadrement au sein de l'équipe microfluidique et les discussions scientifiques que nous avons eues.

J'adresse ma reconnaissance à M. Jean-Philippe Matas, Professeur à l'Université Claude Bernard Lyon 1 et M. Farzam Zoueshtiagh, Professeur à Université de Lille 1 qui ont accepté d'être les rapporteurs et de lire minutieusement ma thèse. Je les remercie d'avoir mis leur expertise à ma disposition et d'avoir ainsi enrichi mon travail au travers des corrections, suggestions et échanges que nous avons eus.

Je remercie chaleureusement M. Jean-Luc Achard, Directeur de recherche à LEGI pour avoir accepté d'examiner ma thèse. Son éclairage complémentaire sur le sujet a été très instructif. Je le remercie également pour ses recommandations en vue d'un post-doc aux USA avec Dino Di Carlo et Elodie Sollier.

J'adresse également quelques lignes ici à Mme Christine Lafforgue pour son accueil chaleureux et son aide lors des expériences réalisées au LISBP et pour l'éclairage biologique qu'elle a apporté à ce travail. Je remercie sincèrement Mme Micheline Abbas pour les comparaisons numérique/expérimentale que nous avons pu faire grâce à ses simulations numériques et pour

son apport théorique sur le sujet.

Je remercie également toutes les personnes de l'ICA qui m'ont aidé au quotidien, à un moment ou à un autre – en particulier Christine Barrot, Marcos Rojas-Cardenas, Nicolas Laurien, Stéphane Orieux, Jie Chen, Jian Fu, Shiqi Wang, Tao Li, Yiwei Wang, Donghai Qiu, Tohme Tohme, Hacene Si-Hadj-Mohand, Guillermo López-Quesada, Dominique Fratantonio, Daniel Mariuta, Varun-Kumar Yeachana – ainsi que toutes les personnes que je n'ai pas citées et qui m'ont encouragé.

Enfin, je remercie mes parents qui m'ont toujours soutenu et ont toujours cru en moi et bien sur ma femme Yanping pour sa compréhension et son aide tout au long de la réalisation de ces travaux. Elle m'a donné le plus beau des cadeaux, notre fils Nolan.

# Abstract

This thesis aims to better understand the physical mechanism controlling the trajectories of particles in confined flows in order to improve predictive models. In the first step we have developed experimental tools based on microscopy and image analysis in order to identify the particles positions in confined flows in square section microchannels. These tools have then permitted to obtain original results on the lateral migration of spherical particles in flows at low inertia. In particular, we have shown that neutrally buoyant particles in square channels are focused at channel center at low Reynolds number and at four channel faces at high Reynolds, and that there is a co-existence of the two regimes for intermediate Reynolds. In addition to their lateral migration, under certain conditions, particles can also align in the flow direction to form trains of evenly spaced particles. This work has thus been devoted to the statistical study on the quantification and localization of the train formation and configuration. It has been shown that the formation of trains is controlled by the flow configuration in the wake of the particles, and that the train characteristics, i.e., the fraction of particles in trains and the interparticle distance, are functions of the particle Reynolds number. Finally, preliminary results on flows of bidisperse suspensions have been obtained. To conclude, the perspectives and future developments of this work are presented.

## **Keywords:**

inertial focusing; microfluidics; hydrodynamic interaction; suspensions; microscopy



# French Summary

## Migration Inertielle de Particules en Écoulement dans des Microcanaux

### Introduction

Dans de nombreux domaines tels le diagnostic clinique, la recherche biologique, le traitement de l'eau, de l'air, l'industrie pharmaceutique ou encore l'analyse chimique, il est très important de détecter, compter, concentrer ou séparer les particules d'un mélange. Les systèmes microfluidiques permettant de manipuler des particules dans un micro-écoulement peuvent répondre à ce besoin. De nombreux dispositifs de micro-séparation ont été développés, certains basés sur la présence d'un ou deux écoulements secondaires (méthode dite « par flux pincé »), d'autres sur l'utilisation de champs externes. Récemment, une méthode passive sans flux pincé appelée méthode de focalisation inertielle a attiré beaucoup d'attention car elle ne repose que sur l'action de forces hydrodynamiques sans utiliser ni écoulements supplémentaires ni champ externe.

La focalisation inertielle s'appuie sur les mécanismes naturels de migration inertielle des particules au sein d'un fluide. En effet, des forces de portance inertielles apparaissent au sein d'un micro-canal dans certaines conditions d'écoulement ; ces forces poussent les particules à la fois à se déplacer latéralement vers des positions d'équilibre spécifiques et à s'organiser longitudinalement pour former des trains. Les caractéristiques de ces deux phénomènes (positions d'équilibre, longueur de focalisation, distance inter-particule ...) dépendent des conditions d'écoulement, de la géométrie du canal et des propriétés des particules. L'existence conjointe de ces deux manifestations (déplacement latéral et organisation longitudinale) est très porteuse car elle laisse envisager la possibilité de développer des dispositifs où la position des particules est contrôlée dans les trois dimensions de l'écoulement.

Cette thèse présente une étude expérimentale de la migration inertielle de particules sphériques dans des canaux droits de section carrée principalement. Les résultats obtenus permettent d'une part d'accroître la compréhension des mécanismes de migration et d'autre part d'avancer sur le développement de nouveaux dispositifs de séparation.

## **Etude bibliographique**

Le phénomène de migration inertiel a été mis en évidence en premier par Poiseuille (1836) ; il a observé des distributions non homogènes des cellules dans des vaisseaux capillaires. En 1961 Segré et Silberberg ont expérimentalement analysé ce phénomène et trouvé que des sphères en écoulement dans un canal de section circulaire s'accumulaient à une distance du centre du tube proche de 0,6 fois le rayon du canal. Ce phénomène de migration appelé « Tubular pinch effect » est dépendant de la géométrie du canal. Dans un canal de section carrée, il est maintenant connu que les particules se concentrent sur quatre positions d'équilibre localisées à proximité du centre des parois du canal et dans un canal de section rectangulaire sur deux positions d'équilibre proches du centre des grandes parois.

D'après l'analyse des travaux de la littérature, de nombreuses forces peuvent agir sur des particules en écoulement. Nous nous sommes intéressés dans cette thèse à l'étude de particules sphériques rigides iso-denses en écoulement dans des canaux carrés droits. Les particules subissent dans ce cas à la fois une force de traînée parallèle à l'écoulement qui ne participe pas à la migration latérale, et des forces de portance perpendiculaires à l'écoulement: la force de répulsion des parois qui pousse les particules vers le centre du canal, la force due au gradient de cisaillement qui les dirige vers les parois du canal et la force de Magnus due à la rotation des particules qui les mène vers la zone où le cisaillement est faible. L'équilibre entre ces 3 forces conduit les particules à se concentrer sur des positions d'équilibre spécifiques. Dans des configurations plus complexes, d'autres forces peuvent intervenir : une force de Saffman apparaît par exemple lorsque la particule n'a pas la même vitesse que le fluide ; des forces liées aux propriétés rhéologiques du fluide ou encore à la présence d'écoulements secondaires induits par la courbure du canal peuvent aussi s'ajouter. La migration inertuelle est aussi influencée par de nombreux paramètres liés aux propriétés des particules, comme leur taille, leur concentration, leur déformabilité, leur forme ou leur densité.

## Méthodologie et dispositif expérimental

Deux méthodes ont été choisies et développées pour étudier la migration de particules dans nos conditions d'écoulement: la méthode de visualisation *in situ* et la méthode de projection axiale.

Le premier dispositif et le plus utilisé est basé sur la visualisation *in situ*. L'écoulement est généré au sein de microcanaux en borosilicate carrés de 80 µm de côté et de longueur allant de 10 à 60 cm par un pousse-seringue et est observé à l'aide d'un microscope optique traditionnel. Une camera CCD permet la capture des images. La suspension de particules de polystyrène est rendue isodense par un mélange de glycérol et d'eau ultrapure. A chaque position, 2000 images sont prises pour permettre une analyse statistique satisfaisante.

Dans ces conditions expérimentales, la profondeur de mesure est estimée à 10 µm. Nous avons donc partitionné le canal en 8 couches de mesure. L'observation des distributions des particules dans les différentes couches d'une même configuration permet de déduire la distribution probable des particules dans la section transversale.

Pour déterminer les distributions de particules à partir des images capturées, un programme de post-traitement sur Matlab a été développé. En premier lieu, les parois du canal sont identifiées sur l'image initiale, afin de réaliser la rotation et le recadrage sur l'intérieur du canal. Puis nous procédons à la soustraction du bruit de fond. L'image en niveaux de gris est ensuite convertie en image binaire par seuillage. Enfin, les particules sont filtrées selon leur forme et la présence d'un point brillant. Le résultat final, correspondant à l'accumulation des particules identifiées sur les 2000 images est présenté sur une même figure pour visualiser la distribution spatiale statistique.

La deuxième méthode optique est basée sur la projection axiale. Dans ce dispositif, le micro-écoulement est projeté sur une membrane placée perpendiculairement au canal. Les particules fluorescentes sont capturées sur la membrane et observées sous microscope à fluorescence. L'image obtenue permet de déterminer la distribution des particules en sortie du canal. Cette méthode sert dans cette thèse de méthode complémentaire permettant de visualiser la

distribution des particules dans la section transversale.

### **Migration latérale dans des suspensions mono-disperses**

Nous avons distingué dans notre étude le cas des écoulements à Reynolds modérés (compris entre 10 et 200 pour les configurations étudiées), celui des écoulements faiblement inertIELS ( $Re < 1$ ), ainsi qu'une zone intermédiaire ( $1 < Re < 10$ ) dite « de transition ».

Dans le cas des écoulements à Reynolds modérés, plusieurs résultats intéressants ont été mis en évidence.

- A un Reynolds donné, au fur et à mesure de l'éloignement de l'entrée du canal, la distribution en particules varie d'un anneau carré lâche à un anneau carré plus étroit puis à 4 tâches situées à proximité du centre de chaque face. Ces distributions montrent que la focalisation se développe le long du canal en deux étapes : dans un premier temps, les particules migrent latéralement, c'est-à-dire perpendiculairement aux iso-vitesse, pour former un anneau. Dans un deuxième temps, elles migrent cross-latéralement, c'est-à-dire parallèlement aux parois, au sein de l'anneau vers les 4 positions d'équilibre. Ce phénomène de migration en deux étapes a été confirmé numériquement par Micheline Abbas. Les trajectoires simulées des particules ont de plus mis en évidence que la première étape où les particules traversent les contours d'iso-vitesse et atteignent un anneau d'équilibre est rapide alors que la deuxième étape où elles se déplacent le long de l'anneau d'équilibre vers les centres des faces nécessite une importante longueur de canal.
- A distance fixée de l'entrée du canal, plus le nombre de Reynolds est élevé plus la focalisation est développée. Nous pouvons donc conclure que le  $Re$  favorise la focalisation dans la gamme de Reynolds modérés considérée.
- A distance de l'entrée du canal et Reynolds fixés, la migration cross-latérale est plus avancée pour les grosses particules que pour les petites. Nous pouvons alors conclure que l'augmentation de la taille des particules favorise la focalisation.

- La localisation exacte de la position d'équilibre est un élément clé pour la conception de micro-dispositifs de concentration et de séparation. Nous avons mis en évidence qu'elle se rapproche des parois lorsque  $Re$  augmente et qu'elle est plus proche des parois pour les petites particules que pour les plus grosses.
- Pour tenter de quantifier le niveau de développement de la focalisation, nous avons introduit un paramètre adimensionnel appelé degré de focalisation, défini comme le rapport entre le nombre de particules présentes dans quatre zones déterminées centrées sur les positions d'équilibre sur le nombre total de particules. A Reynolds donné, le degré de focalisation augmente au fur et à mesure de l'avancée dans le canal. A distance de l'entrée fixée, le degré de focalisation augmente avec le Reynolds, atteint un maximum aux environs de  $Re = 150$  puis diminue. De fait, l'observation fine des distributions à  $Re = 280$ , semble montrer une plus grande dispersion, les particules formant à nouveau un anneau proche du périmètre du canal. Ce phénomène est cohérent avec le dernier article de Nakagawa datant de 2015 qui montre numériquement que des positions d'équilibre supplémentaires apparaissent au-delà d'un  $Re$  critique proche de 260.

Dans le cas des écoulements faiblement inertIELS ( $Re < 1$ ), un nouveau régime de migration a été observé où les particules migrent vers le centre du canal. La migration vers le centre est un phénomène lent et des canaux de grande longueur sont nécessaires pour amener la focalisation à son terme.

Pour les Reynolds intermédiaires ( $1 < Re < 10$  dans notre configuration expérimentale), les deux régimes de migration cohabitent ; nous retrouvons donc simultanément des particules focalisées au centre du canal et d'autres proches des parois. Une augmentation de la concentration en particules décale la zone de transition vers des Reynolds plus élevés et favorise la migration vers le centre. Une augmentation de la taille des particules quant à elle, favorise la focalisation quel que soit le régime de migration : vers le centre ou vers les parois.

## **Formation des trains**

La migration inertielle des particules engendre simultanément le déplacement des particules vers des positions d'équilibre spécifiques et leur organisation longitudinale pour former des trains. Matas en 2004 suggère que la formation des trains est liée à la présence de lignes de courant inversées autour des particules. Lee en 2010 propose un mécanisme de formation des paires de particules. Il suggère que forces de traînées liées aux lignes de courant inversées et forces inertielles contribuent à générer des interactions hydrodynamiques entre particule suiveuse et particule de tête aboutissant à la formation d'une paire.

Notre dispositif expérimental, en combinaison avec le programme de post-traitement Matlab élargi, a permis de localiser les trains et d'évaluer statistiquement deux paramètres fondamentaux : la fraction de particules en trains et la distance entre particules d'un même train.

La localisation des trains a permis de montrer que la formation des trains se mettait en place uniquement une fois les particules sur leurs positions d'équilibre et uniquement sur les positions d'équilibre proches des parois. La migration faiblement inertielle observée à faible nombre de Reynolds ( $Re < 1$ ) vers le centre du canal, ne semble pas être accompagnée par l'organisation longitudinale des particules. La fraction de particules en trains augmente en fonction du Reynolds dans la gamme de Reynolds modérés étudiée, passe par un maximum pouvant atteindre 80% puis diminue. Nous avons montré que ce pourcentage était directement corrélé à la fraction de particules ayant déjà atteint leurs positions d'équilibre autrement dit au degré de focalisation. La distance entre particules d'un même train quant à elle, diminue avec le nombre de Reynolds indépendamment de la concentration, sauf lorsque la limite d'encombrement est atteinte. Dans ce dernier cas (i.e., lorsque le nombre de particules présentes dans la suspension dépasse le nombre maximum de particules alignables sur les lignes d'équilibre), la distance inter-particulaire diminue pour que toutes les particules puissent prendre place sur les positions d'équilibre.

## **Migration dans des suspensions bidisperses**

Nous avons commencé de manière exploratoire à étudier la migration latérale (à la fois le déplacement latéral et l'organisation longitudinale) d'un mélange de particules sphériques de deux tailles différentes déjà étudiées en suspensions mono-disperses. Les distributions de particules obtenues en suspension mono- et bidisperse pour chacune des tailles de particules sont similaires, tendant à prouver que, la bidispersité ne modifie pas la migration latérale dans nos conditions expérimentales. Elle semble par contre influencer la formation des trains. Nous avons observé à la fois des trains mixtes et des trains monodisperses, 80% d'entre eux commençant par une grosse particule et 60% se terminant par une petite. La fraction de particules en trains augmente, passe par un maximum puis diminue de manière similaire pour les deux tailles de particules mélangées mais les maximums atteints sont supérieurs en suspension bidisperse à ceux atteints en suspension monodisperse. Il semblerait donc que la bidispersité favorise la formation de trains.

## **Conclusion et perspectives**

Ce travail de thèse apporte une avancée significative sur la compréhension du phénomène de migration inertielle. Il permet ainsi à la communauté scientifique de mieux appréhender et prédire le transport de particules en micro-écoulement liquide. Il ouvre aussi de très nombreuses perspectives. A court terme, il s'agirait d'approfondir la modification du phénomène de migration latérale à  $Re > 200$ , d'étudier la robustesse des trains formés et de creuser l'influence de la bidispersité sur la migration inertielle. A plus long terme, les connaissances acquises devrait permettre le développement de nouveaux dispositifs de détection, concentration ou séparation de particules à micro-échelle et donc intégrables sur un laboratoire sur puce.



# Table of Contents

<b>Remerciements.....</b>	<b>I</b>
<b>Abstract .....</b>	<b>III</b>
<b>French Summary .....</b>	<b>V</b>
<b>Table of Contents.....</b>	<b>XIII</b>
<b>List of Figures .....</b>	<b>XVII</b>
<b>List of Tables .....</b>	<b>XXV</b>
<b>Nomenclature.....</b>	<b>XXVII</b>
<b>Introduction .....</b>	<b>1</b>
<b>Chapter 1. Bibliographic Study.....</b>	<b>5</b>
1.1 Focusing techniques .....	5
1.1.1 Sheath flow focusing techniques .....	5
1.1.2 Sheathless flow focusing techniques .....	7
1.2 Phenomenon of inertial migration .....	11
1.3 Mechanisms of inertial migration for neutrally buoyant particles .....	14
1.3.1 Wall-induced lift force .....	15
1.3.2 Shear-induced lift force .....	15
1.3.3 Rotation-induced lift force.....	16
1.3.4 Secondary-flow drag force .....	17
1.4 Influence of channel, particle and fluid characteristics on inertial focusing .....	18
1.4.1 Channel properties .....	18
1.4.2 Particle properties .....	22
1.4.3 Fluid and flow properties.....	27
1.5 Applications .....	30

1.5.1	Particle separation.....	30
1.5.2	Volume reduction.....	32
1.5.3	Particle alignment .....	32
1.5.4	Solution exchange.....	33
1.6	Summary .....	34

## **Chapter 2. Methodology Development and Experimental Design.....37**

2.1	Introduction to currently existing techniques.....	37
2.1.1	Tomographic techniques .....	37
2.1.2	Ultrasonic technique .....	39
2.1.3	Optical techniques .....	39
2.2	<i>In situ</i> visualization method .....	42
2.2.1	Materials .....	43
2.2.2	Experimental setup .....	47
2.2.3	Implementation .....	48
2.3	Particle projection method .....	58
2.3.1	Materials .....	59
2.3.2	Experimental setup and implementation .....	60
2.3.3	Data processing.....	61
2.4	Summary .....	62

## **Chapter 3. Lateral Migration in Monodisperse Suspensions.....63**

3.1	Particle migration at moderate inertia.....	64
3.1.1	Influence of the distance from channel inlet $z/H$ .....	64
3.1.2	Influence of Reynolds number $Re$ .....	67
3.1.3	Influence of particle to channel size ratio.....	69
3.1.4	Equilibrium positions localization.....	70
3.1.5	Outermost edge of particle distributions .....	72
3.1.6	Focusing degree .....	73

3.2	Particle migration at low inertia.....	77
3.2.1	Influence of Reynolds number $Re$ .....	77
3.2.2	Influence of channel length $z/H$ .....	79
3.2.3	Influence of particle volume fraction .....	81
3.2.4	Influence of particle to channel size ratio.....	86
3.3	Preliminary study on biological particles.....	89
3.4	Summary .....	92
<b>Chapter 4.</b>	<b>Particle Alignment.....</b>	<b>95</b>
4.1	Bibliographic study.....	95
4.2	Characterization of particle trains .....	98
4.2.1	Identification of trains .....	98
4.2.2	Effect of $Re_p$ and $d_p$ .....	100
4.2.3	Low inertia.....	105
4.2.4	Effect of solid volume fraction .....	106
4.2.5	Particle trains in rectangular channels: preliminary results.....	108
4.3	Dynamics of particle self-ordering .....	110
4.4	Summary .....	114
<b>Chapter 5.</b>	<b>Migration in Bidisperse Suspension: Preliminary Results .....</b>	<b>115</b>
5.1	Suspension .....	116
5.2	Lateral migration.....	116
5.2.1	Particle distribution.....	117
5.2.2	Equilibrium position localization .....	120
5.2.3	Outermost edge of particle distribution .....	121
5.2.4	Focusing degree .....	122
5.3	Longitudinal ordering of bidisperse particles .....	123
5.3.1	Fraction of particles in trains .....	124
5.3.2	Sequential ordering.....	126

5.3.3 Interparticle spacing .....	128
5.4 Summary .....	130
<b>Conclusions &amp; Perspectives.....</b>	<b>133</b>
Conclusions .....	133
Perspectives .....	135
<b>Bibliography .....</b>	<b>137</b>
<b>Résumé .....</b>	<b>149</b>

# List of Figures

Fig. 1-1	Schematic drawing of symmetric sheath flow focusing (top view of microchannel): the sample flow supplied from the inlet channel at left is constrained laterally within the center of the microchannel by two neighboring sheath flows from the top and down side channels. (Reprinted from Lee et al. (2006).)	6
Fig. 1-2	Schematic of a typical active sheathless flow focuser. (Reprinted from Pamme (2007).)	8
Fig. 1-3	Cross-sectional schematic of the device for hydrophoretic separation. (Reprinted from Choi et al. (2012).)	9
Fig. 1-4	Scheme of the Deterministic Lateral Displacement method. (Reprinted from Loutherback et al. (2010).)	10
Fig. 1-5	Scheme of a gravity-driven separation device. (Reprinted from Huh et al. (2007).)	10
Fig. 1-6	Tubular pinch effect. The left image shows the experimental results of Segre and Silberberg (1962b), showing how radial migration develops in a cylindrical tube along channel. (Reprinted from Segre and Silberberg (1962b).) The right image shows the experimental distribution of particles in the cross section of a cylindrical tube at $Re = 350$ . (Reprinted from Matas et al. (2004c).)	12
Fig. 1-7	Inertial focusing of particles in a cylindrical channel, a square channels and a rectangular channel, from left to right in the image, respectively. (Reprinted from Di Carlo (2009) and Amini et al. (2014).)	13
Fig. 1-8	Schematic drawing of inertial focusing in a rectangular microchannel. (Reprinted from Zhou and Papautsky (2013).)	14
Fig. 1-9	Wall-induced lift force.	15
Fig. 1-10	Shear-induced lift force.	16
Fig. 1-11	Rotation-induced lift force.	17
Fig. 1-12	Secondary-flow drag force, i.e., Stokes' drag.	18
Fig. 1-13	Simulated velocity profiles, normalized Dean flow vectors and idealized particle equilibrium positions at $Re = 419$ , for three different confinements ( $d_p/D_h = 0.066$ blue,	

$d_p/D_h = 0.149$ green, $d_p/D_h = 0.225$ red) in a straight channel ( $\delta = 0$ ) and increasing in curvature left to right. (Reprinted from Martel and Toner (2013).)	20
Fig. 1-14 Inertial focusing in non-rectangular channels, from left to right, half-circular channel, narrow triangular channel and wide triangular channel, respectively. (Reprinted from Kim et al. (2016).)	21
Fig. 1-15 Schematic of spiral channel with trapezoid cross-section indicating the inertial focusing of 10 $\mu\text{m}$ (white) and 6 $\mu\text{m}$ (red) beads. (Reprinted from Wu et al. (2012).)	21
Fig. 1-16 Schematic diagram describing Hur's device composed of expansion-contraction reservoirs for particle separation. (Reprinted from Hur et al. (2011c).)	22
Fig. 1-17 Saffman's force. $V$ is the relative velocity of the sphere. $V > 0$ , the sphere moves faster than the fluid; $V < 0$ , the sphere goes slower than the fluid.	23
Fig. 1-18 Distance between the equilibrium position and the closest wall in function of normalized particle maximum diameter for various shapes. (Reprinted from Hur et al. (2011b).)	24
Fig. 1-19 Schematic and overlaid micrographs illustrating the inertial focusing of randomly distributed ellipsoid particles. (Reprinted from Masaeli et al. (2012).)	25
Fig. 1-20 Distance between equilibrium position and the closest wall in rectangular microchannels for viscous droplet and elastic particles of different particle diameter to channel width ratios and various viscosity ratio. (Reprinted from Hur et al. (2011b).)	26
Fig. 1-21 Equilibrium positions within the rectangular channel cross section as a function of $Re$ . (Reprinted from Ciftlik et al. (2013).)	27
Fig. 1-22 Migration regimes in a tube as a function of particle volume fraction $\Phi$ and Reynolds number $Re$ . (Reprinted from Han et al. (1999).)	28
Fig. 1-23 Cancer cell distribution in a half of rectangular channel cross section at different flow and concentration conditions. (Reprinted from Lim et al. (2012).)	29
Fig. 1-24 Schematic diagram of size-dependent particle separation using elasto-inertial characteristics of non-Newtonian fluid flow. (Reprinted from Nam et al. (2012).)	30
Fig. 1-25 Schematic of equilibrium separation in a straight channel with an expansion zone. (Reprinted from Mach and Di Carlo (2010).)	31

Fig. 1-26	Schematic of kinetic separation in a rectangular channel with modulation of aspect ratio. (Reprinted from Zhou et al. (2014).)	31
Fig. 1-27	Sequential images along a fluidic path in a double spiral channel showing the enrichment of particles. (Reprinted from Seo et al. (2007).)	32
Fig. 1-28	Schematic of Hur's design for particle alignment. (Reprinted from Hur et al. (2011c)..)	33
Fig. 1-29	Schematic of Egg's design to control single-cell encapsulation. (Reprinted from Edd et al. (2008).)	33
Fig. 1-30	Schematic of Gossett's device for rapid inertial solution exchange. (Reprinted from Gossett et al. (2012).)	34
Fig. 2-1	Scanning Electron Microscope (SEM) image of the microchannel cross section (80 $\mu\text{m}$ $\times$ 80 $\mu\text{m}$ ).	45
Fig. 2-2	Experimental setup of <i>in situ</i> visualization method.	48
Fig. 2-3	Image of 8.7- $\mu\text{m}$ particles flowing in an 80 $\mu\text{m}$ $\times$ 80 $\mu\text{m}$ square channel with the focus at the channel midplane.	48
Fig. 2-4	Observation of a bright spot with the focal plane at the top of the particle.	49
Fig. 2-5	Displacement of the objective focal plane. (Barrot Lattes et al. 2008)	50
Fig. 2-6	Calibration of the displacement of the focal plane.	51
Fig. 2-7	Illustration of the localization process of the midplane of the channel	52
Fig. 2-8	Depth of the focus field calibrated by static particles with a step size of 1 $\mu\text{m}$ .	53
Fig. 2-9	Depth of measurement calibrated by static particles in suspension with a step of 1 $\mu\text{m}$ ...	54
Fig. 2-10	Illustration of measurement layer in a microchannel	55
Fig. 2-11	Complete image post-processing. (a) Detection of channel edges and inclination; (b) Rotation of the microchannel; (c) Choice of the region of interest (d) Image after subtraction of background noise; (e) Conversion to a binary image; (f) Identification of real particles; (g) Selection of in-focus particles; (h) Overall in-focus particle positions summed from 2,000 images.	56
Fig. 2-12	PDF calculation method. (a) Measurement planes. (b) Example of a PDF histogram. (c) Example of a 3D histogram.	58

Fig. 2-13	Experimental setup of particle projection method. ①: microchannel; ②: membrane; ③: stainless steel syringe; ④: syringe pump; ⑤: membrane holder; ⑥: manometer; ⑦: pump; ⑧: liquid outlet; ⑨: filtered water; ⑩: micrometric screw. (Lafforgue-Baldas et al. 2013).....	61
Fig. 2-14	Fluorescent image illustrating the distribution of particles in the cross section.....	61
Fig. 3-1	Spatial distributions (PDFs) of 8.7- $\mu\text{m}$ test particles over normalized lateral positions at fixed $Re = 11.2$ for various measurement positions $z/H$ .....	64
Fig. 3-2	Spatial distributions (PDFs) of 8.7- $\mu\text{m}$ test particles over normalized lateral positions at fixed $Re = 28$ for various measurement positions $z/H$ . Schematics of the particle distributions in the cross section are also sketched at the bottom of the figures. ....	66
Fig. 3-3	Spatial distributions (PDFs) of 8.7- $\mu\text{m}$ test particles over normalized lateral positions at fixed $Re = 56$ for various measurement positions $z/H$ . Schematics of the particle distributions in the cross section are also sketched at the bottom of the figures. ....	66
Fig. 3-4	Simulated trajectories of individual particles for a quarter of the channel cross section. The thick black lines are the particle trajectories for $Re = 120$ ; the red, blue and green dashed lines are the trajectories from the same initial position for $Re = 12, 60$ and $120$ , respectively. (Abbas et al. 2014) .....	67
Fig. 3-5	Spatial distributions (PDFs) of 8.7- $\mu\text{m}$ test particles over normalized lateral positions at finite inertia for various $Re$ at a fixed entry length $z/H = 1,000$ .....	68
Fig. 3-6	Spatial distributions (PDFs) of 5.3- $\mu\text{m}$ test particles over normalized lateral positions for various $Re$ at a fixed entry length $z/H = 1,000$ . ....	69
Fig. 3-7	Cross-sectional distributions of 8.7- $\mu\text{m}$ (red) and 4.8- $\mu\text{m}$ (green) test particles on a membrane at $Re = 8.3$ and $16.6$ , respectively. ....	70
Fig. 3-8	Particle equilibrium position $X_{eq}$ as a function of $Re$ .....	72
Fig. 3-9	Particle outermost edge $X_{out}$ as a function of $Re$ for different $d_p/H$ . ....	73
Fig. 3-10	Focusing degree as a function of channel length $z/H$ for 8.7- $\mu\text{m}$ particles at $Re = 11.2$ ...	74
Fig. 3-11	Degree of migration at fixed channel length $z/H = 1,000$ with respect to $Re$ .....	75
Fig. 3-12	Overall particle distributions (left) and in-focus particle distributions (right) at channel	
XX		

midplane at $Re = 112, 210$ and $280$ .	76
Fig. 3-13 Particle distributions obtained experimentally at $Re = 144$ (left side), $Re = 260$ (middle) and $Re = 514$ (right side). (Reprinted from Nakagawa et al. (2015).)	76
Fig. 3-14 Spatial distributions (PDFs) of $8.7\text{-}\mu\text{m}$ test particles over normalized lateral positions at low and finite inertia at a fixed entry length $z/H = 7,125$ for various $Re$ . Schematics of the particle distributions in the cross section are also sketched at the bottom of the figures.	78
Fig. 3-15 Spatial distributions (PDFs) of $8.7\text{-}\mu\text{m}$ test particles over normalized lateral positions at fixed $Re = 1.4$ for various measurement position $z/H$ .	80
Fig. 3-16 Spatial distributions (PDFs) of $8.7\text{-}\mu\text{m}$ test particles over normalized lateral positions at fixed $Re = 5.6$ for various measurement position $z/H$ .	81
Fig. 3-17 Spatial distributions (PDFs) of $8.7\text{-}\mu\text{m}$ test particles over normalized lateral positions at a fixed entry length $z/H = 7,125$ for various $Re$ at a concentration $\Phi = 0.2\%$ .	82
Fig. 3-18 Spatial distributions (PDFs) of $8.7\text{-}\mu\text{m}$ test particles over normalized lateral positions at a fixed entry length $z/H = 7,125$ for various $Re$ at a high concentration $\Phi = 0.4\%$ .	83
Fig. 3-19 Particle cluster formation at high concentration.	84
Fig. 3-20 Spatial distributions (PDFs) of $8.7\text{-}\mu\text{m}$ test particles over normalized lateral positions at fixed $Re = 1.4$ and $5.6$ for various entry length $z/H$ at a high concentration $\Phi = 0.4\%$	85
Fig. 3-21 Spatial distributions (PDFs) of $5.3\text{-}\mu\text{m}$ test particles over normalized lateral positions at a fixed entry length $z/H = 7,125$ for various $Re$ .	87
Fig. 3-22 Spatial distributions (PDFs) of $5.3\text{-}\mu\text{m}$ test particles over normalized lateral positions at a fixed entry length $z/H = 7,125$ for various $Re$ . (Aggregations are taken into account)	88
Fig. 3-23 Cross-sectional distributions of $8.7\text{-}\mu\text{m}$ test particles on a membrane at $Re = 1.0, 2.1$ and of $4.8\text{-}\mu\text{m}$ test particles at $Re = 2.1$ , from left to right respectively.	89
Fig. 3-24 Microscopic observation of the yeasts and the bacteria. ( $\times 1,000$ magnification)	90
Fig. 3-25 Cross-sectional distributions of yeasts on a membrane at $Re = 8.3, 12.5$ and $16.6$ , respectively.	91
Fig. 3-26 Cross-sectional distributions of bacteria on a membrane at $Re = 12.5$ and $16.6$ , respectively.	

Fig. 3-27	Microscopic image of the yeast cells in a micro channel at $Re = 56$ and $z/H = 1,000$ .....	91
Fig. 4-1	Simulated streamlines around an isolated sphere for $Re = 48$ . (Reprinted from (Lee et al. 2010).) .....	96
Fig. 4-2	Schematic drawing of the interaction between two aligned particles. (Reprinted from (Lee et al. 2010).) .....	97
Fig. 4-3	(a) Schematic drawing of the experimental setup. Examples of image recorded of particle trains at mid height ( $y/H = 0.5$ ), $z/H = 1,000$ , $\Phi = 0.1\%$ and (b) $Re = 210$ ( $Re_p = 2.48$ ), (c) $Re = 112$ ( $Re_p = 1.32$ ). ....	98
Fig. 4-4	(a) Original gray-scaled image horizontally rotated. (b) Post-processed image where particles in trains are highlighted by rectangles. (c) PDFs of the normalized interparticle spacing for $Re_p = 0.33$ and $3.31$ , $\Phi = 0.1\%$ and $z/H = 1,000$ .....	100
Fig. 4-5	(a) Fraction of particles in trains $\psi$ as a function of particle Reynolds numbers $Re_p$ and channel Reynolds numbers $Re$ (inset) for $d_p/H = 0.11$ and $d_p/H = 0.066$ . (b) Normalized interparticle distance $l/d_p$ as a function of particle Reynolds numbers $Re_p$ for $d_p/H = 0.11$ and $d_p/H = 0.066$ .....	103
Fig. 4-6	Normalized separation distance $(l-d_p)/H$ as a function of particle Reynolds numbers $Re_p$ for $d_p/H = 0.11$ and $d_p/H = 0.066$ . ....	104
Fig. 4-7	Images of the suspension at $y/H = 0.5$ , $z/H = 1,000$ , $\Phi = 0.4\%$ and (a) $Re_p = 8 \times 10^{-4}$ ( $Re = 0.07$ ) (b) $Re_p = 8 \times 10^{-3}$ ( $Re = 0.7$ ). ....	105
Fig. 4-8	(a) Fraction of particles in trains $\psi$ and (b) normalized interparticle distance $l/d_p$ as a function of particle Reynolds number $Re_p$ for $d_p/H = 0.11$ , $z/H = 1,000$ and $\Phi = 0.02\%$ , $0.05\%$ , $0.1\%$ , $0.2\%$ , $0.3\%$ , $0.8\%$ and $1\%$ . ....	106
Fig. 4-9	Staggered particle trains in rectangular channels. ....	108
Fig. 4-10	Streamlines around an isolated particle computed using lattice Boltzmann simulations. The solid and dotted circles suggest positions of adjacent particles (reprinted from (Humphry et al. 2010)). ....	109
Fig. 4-11	Fraction of particles in trains $\psi$ as a function of Reynolds number for $z/H = 1,000$ and $\Phi = 0.01\%$ .....	110

Fig. 4-12	(a) Fraction of particles in trains $\psi$ and (b) normalized interparticle distance $l/d_p$ as a function of normalized distance from channel inlet for $d_p/H = 0.11$ , $\Phi = 0.1 \%$ and different particle Reynolds numbers $Re_p$ .....	111
Fig. 4-13	PDFs of particles at $y/H = 0.5$ (midplane), $\Phi = 0.1 \%$ , for different $Re_p$ and $z/H$ . Bold red lines correspond to particles in the focal plane and dotted blue ones to particles present in the whole section. Schematics of the particle distributions are proposed at the bottom of the figures.....	112
Fig. 4-14	Numbers of particles in trains at different vertical heights ( $y/H = 0.15, 0.3$ and $0.5$ ) at $Re_p = 0.13$ and $Re_p = 1.32$ for $d_p/H = 0.11$ , $\Phi = 0.1 \%$ .....	113
Fig. 5-1	Microscopic observation ( $50 \times$ ) of a mixture of $5.3\text{-}\mu\text{m}$ and $8.7\text{-}\mu\text{m}$ particles.....	116
Fig. 5-2	Particle identification in the bidisperse suspension ( $Re = 5.6$ ). $8.7\text{-}\mu\text{m}$ and $5.3\text{-}\mu\text{m}$ particles are surrounded by blue and red circles, respectively, and the in-focus and out-of-focus particles by bold and thin circles, respectively.....	117
Fig. 5-3	Overall particle distributions at different vertical positions at $Re = 5.6$ and $112$ .....	118
Fig. 5-4	Particle distributions (PDFs) of bidisperse $8.7\text{-}\mu\text{m}$ (blue) and $5.3\text{-}\mu\text{m}$ (red) particles as a function of $Re$ , at different $y/H$ positions and at $z/H = 1,000$ .....	119
Fig. 5-5	$X_{eq}$ (normalized distance between the equilibrium position and the channel wall) as a function of $Re$ , for bidisperse and monodisperse $8.7\text{-}\mu\text{m}$ and $5.3\text{-}\mu\text{m}$ particles.....	120
Fig. 5-6	$X_{out}$ (normalized distance between the outmost edge and the channel centerline) as a function of $Re$ , for bidisperse and monodisperse $8.7\text{-}\mu\text{m}$ and $5.3\text{-}\mu\text{m}$ particles.....	122
Fig. 5-7	Focusing degree as a function of $Re$ , for bidisperse $8.7\text{-}\mu\text{m}$ and $5.3\text{-}\mu\text{m}$ particles and monodisperse $8.7\text{-}\mu\text{m}$ particles.....	122
Fig. 5-8	Particle trains are identified at the centers of the channel front wall and of the channel bottom wall ( $Re = 112$ , $z/H = 1,000$ , $y/H = 0.5$ ). The $8.7\text{-}\mu\text{m}$ and $5.3\text{-}\mu\text{m}$ particles are encircled by blue and red squares, respectively.....	123
Fig. 5-9	Fraction of particles in trains as a function of $Re$ , for bidisperse and monodisperse $8.7\text{-}\mu\text{m}$ and $5.3\text{-}\mu\text{m}$ particles.....	124
Fig. 5-10	Fraction of particles in trains as a function of $Re_p$ , for bidisperse and monodisperse particles	

and monodisperse 8.7- $\mu\text{m}$ and 5.3- $\mu\text{m}$ particles. ....	126
Fig. 5-11 Examples of bidisperse particle trains, often beginning with a large particle and ending with a small one. ( $Re = 112$ ).....	127
Fig. 5-12 Fraction of trains beginning with large particles and the fraction of trains ending with small particles as a function of $Re$ .....	127
Fig. 5-13 Mean interparticle spacing for bidisperse particles as a function of $Re$ , compared to the interparticle spacings for 8.7- $\mu\text{m}$ and 5.3- $\mu\text{m}$ monodisperse particles.....	129

## List of Tables

Table 2-1	Summary of monodisperse particles.....	44
Table 2-2	List of microchannels used in our experimental studies.....	45
Table 2-3	Summary of stainless steel syringe used in the experiment. ....	46



# Nomenclature

## Roman Symbols

$H$  Channel height

$W$  Channel width

$D_h$  Hydraulic diameter

$d_p$  Particle diameter

$l$  Interparticle distance (particle center-to-center distance)

$l-d_p$  Separation distance (particle surface-to-surface distance)

$Re$  Reynolds number

$Re_p$  Particle Reynolds number

$x$  Horizontal distance in the channel perpendicular to the flow

$y$  Vertical distance in the channel perpendicular to the flow

$z$  Distance in the channel parallel to the flow

$Q$  Flow rate

$U$  Mean flow velocity

$U_m$  Maximum flow velocity

$X_{eq}$  Equilibrium position

$X_{out}$  Outermost edge of particle cluster

$M$  Magnification of lens

$\lambda$  Wavelength

$n_i$  Refractive index of the immersion medium

$n_f$  Refractive index of the studied object

### Greek Symbols

$\lambda$  Particle axial number density

$\Phi$  Particle volume fraction

$\psi$  Fraction of particles in trains

$\rho$  Density

$\mu$  Viscosity

$\delta_{obj}$  Displacement of objective

$\delta$  Displacement of focal plane

$\delta_w$  Errors in determining channel walls

$\delta_p$  Errors in determining particle centers

$\Delta$  Errors in determine equilibrium positions

# Introduction

Particle detection, identification and separation in fluids are essential for society. For example, the search for contaminants in food fluids, the detection of pathogens in bodily fluids and the water filtration are some major environment and public health issues. The need of particle manipulation on the micro-scale is rapidly expanding due to the more stringent industrial standards and the more heightened public health awareness. Particularly, many specific fields like pharmaceuticals, clinical diagnostics, chemical analysis, medical diagnostics, and tissue engineering require high-purity processing since even slight traces of contaminants may cause a dramatic adverse impact.

To satisfy these demands, a variety of particle separation technologies have been developed in the last decades. The commonly used conventional methods (centrifugation and mechanical filtration) often requiring large volumes are less than optimal and are expensive for separating a wide range of particle sizes (Bhagat et al. 2008c). Various miniaturized techniques have thus been proposed based on microfluidics. Sheath flows or external force fields such as magnetic, acoustic, electrical and optical forces are applied to drive the particle migration and separation. However, the requirement of sheath flows or external forces complicates the device fabrication, increases the cost and makes the miniaturization difficult.

More recently, inertial focusing techniques have gained significant attention since they only rely on the hydrodynamic forces and do not require any sheath flows, outer forces or complex channel geometries. These techniques are thus very appealing as they could allow continuous high-throughput and low-cost processing, non-invasive and label-free manipulation, and simple operation (Xiang et al. 2013), and thus could be suitable for a broad range of applications from filtration & enrichment to cytometry of cells (Lim et al. 2012; Zhou et al. 2013a). These techniques also permit the automatization, parallelization and miniaturization in the field of particle manipulation (Kim and Yoo 2008; Lee et al. 2010).

The inertial focusing techniques are indeed based on the inertial migration of the particles in

the fluid. It has been reported that flowing particles can naturally move and focus on some distinct equilibrium positions in the channel cross section, depending on the flow conditions and the channel geometry (Di Carlo 2009). Aside from the lateral focusing, particles are found to order longitudinally along the main flow direction (Edd et al. 2008; Lee et al. 2010). This self-ordering phenomenon suggests the possibility of manipulating particle positions not only in the transverse but also in the flow direction. Understanding the inertial lateral migration and the longitudinal ordering phenomena is actually essential to predict the trajectories of particles flowing in microchannels.

The present thesis aims at experimentally investigating the inertial focusing of spherical particles flowing in square straight microchannels. Straight channels and spherical particles are chosen because of their high simplicity allowing the study of the basic mechanisms. Square channels are used due to their easy manufacturing process and the sharp location of the particle equilibrium positions at moderate Reynolds numbers. This dissertation consists of the following five chapters:

**Chapter 1** Firstly, we introduce the different existing focusing techniques. Then we focus on the inertial migration phenomenon, by reviewing the main works published on the subject, involving its fundamental mechanisms, the essential parameters that influence the inertial migration and the applications.

**Chapter 2** We firstly reviewed the current experimental techniques to study the particle positions in two-phase flows. Then the *in situ* visualization method developed in this work is described, along with the experimental setup design, the implementation, and the post-processing algorithms to estimate the three dimensional particle distributions. The particle projection method is also presented, for direct visualization of particle distribution in the channel cross section, to give a complementarity to the *in situ* visualization method results.

**Chapter 3** This chapter is devoted to the investigation of the lateral migration phenomenon of monodisperse particles in square channels. The migration process and the final equilibrium positions are studied through the observation of the particle distribution at different distances

from the channel inlet for various Reynolds numbers, particle volume fractions and particle to channel size ratios.

**Chapter 4** We delve into the particle longitudinal ordering phenomenon. The fraction of particles in trains and the interparticle spacing are evaluated for various Reynolds numbers, particle volume fractions, particle to channel size ratios and distances from channel inlet. A discussion on the possible mechanism for this longitudinal ordering is also proposed.

**Chapter 5** We present a preliminary study on the migration of particles of two different sizes mixed into a suspension. Both lateral focusing behaviors and longitudinal ordering are studied and compared with the results obtained for monodisperse suspensions of the same particles, in order to show the effect of bidispersity.

Finally, conclusions on the thesis work and perspectives for future work are proposed.



# **Chapter 1. Bibliographic Study**

Recent advances in microfluidic technology have led to the emergence of micro total analysis systems ( $\mu$ -TAS) or lab-on-a-chip (LOC) devices. Such devices have shown a considerable potential for a wide variety of applications in biochemistry, biophysics and medical fields, including biological and chemical assays, drug delivery, drug screening and so on (Lee et al. 2006). The ability to precisely focus particles on specific positions is essential in some of these devices, particularly when the objective is to separate cells, functionalized beads, or other particles from a solution which may contain other undesirable elements (Loutherback et al. 2010).

In this chapter, we first thoroughly describe the existent methods for particle focusing, including sheath flow focusing and sheathless flow focusing among which we highlight the inertial focusing as the most potential solution. Secondly we present the current state of the art in the understanding of the fundamental mechanisms controlling the phenomenon of inertial focusing, including the wall-induced lift force, the shear-induced lift force, the rotation-induced lift force and the secondary-flow drag force. Then the important parameters, involving the channel properties, particle properties and fluid properties, that influence the inertial migration are discussed. Finally, different applications of inertial focusing are presented.

## **1.1 Focusing techniques**

The particle focusing methods can be divided into two types: sheath flow and sheathless flow techniques. Sheath flow focusers use one or more particle-free fluids to pinch the particle-rich fluid in order to focus particles. Sheathless flow focusers use inertial fluid dynamics or externally applied fields (electrical, magnetic or acoustic).

### **1.1.1 Sheath flow focusing techniques**

Sheath flow focusing is probably the most commonly used approach in microfluidic devices (Zhao et al. 2007) and has been demonstrated in a wide variety of applications, including flow

cytometers for cell counting and sorting, cell patterning, diffusion-based mixers, microfluidic injection systems and micro flow switches (Yang et al. 2005).

Two types of sheath flows are usually used: hydrodynamically driven (Lee et al. 2006) sheath flows delivered by external pumps (e.g., syringe pumps) and electrokinetically driven (Yang et al. 2005) sheath flows generated by electrokinetic forces. An example to illustrate the principle of a common hydrodynamic sheath flow focusing device is given in Fig. 1-1. One or more sheath flows are fed via the side channels into a main channel to direct the main sample flow into a specific position within the channel as shown in Fig. 1-1. By adjusting the density, viscosity, and flow rate of the sheath flows with respect to the sample flow, this one can be focalized into the desired region with a controlled width (Lee et al. 2006). Here the width of the focused stream is in the same order of magnitude as the suspended cells or particles. Hence, the cells or particles are ordered and pass through the detection region one by one, which is suitable for cells/particles counting and sorting. Various designs of sheath flow focusing microsystem have been reported and recently reviewed (Howell et al. 2008; Huh et al. 2007; Xuan and Li 2005).

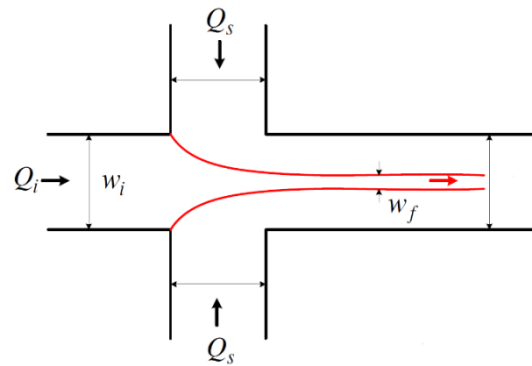


Fig. 1-1 Schematic drawing of symmetric sheath flow focusing (top view of microchannel): the sample flow supplied from the inlet channel at left is constrained laterally within the center of the microchannel by two neighboring sheath flows from the top and down side channels. (Reprinted from Lee et al. (2006).)

Sheath flow focusers show numerous advantages. The focused stream can be easily tuned with

different widths and in various positions (Scott et al. 2008). Moreover, the focusing result is independent of the particles size, thus a same device can be used for a wide range of particles. Until now, this method is commonly used in most of the commercial flow cytometers where the width of the focused stream is of the same order of magnitude as the cell size.

However, some disadvantages can be emphasized. The need of accurately maintained sheath flows complicates the device fabrication, increases the cost and makes the miniaturization difficult. Furthermore, the addition of sheath flow leads to the dilution of the sample flow and sometimes to a modification of its properties. Finally, the high flow rates needed to pinch the particles could damage them in case of living bio-cells.

### **1.1.2 Sheathless flow focusing techniques**

The sheathless flow focusing techniques manipulate the sample flow only relying on external or internal forces, without introduction of accompanying sheath flows in the channel. Thus the major advantage of sheathless flow focusing is avoiding the dilution of sample flow and the change of solution properties. The sheathless flow focusing can be classified into two types according to the nature of the force involved: active when the force is externally applied and passive when the force is internally induced.

#### **1.1.2.1 Active sheathless flow focusing techniques**

In active sheathless techniques, the sample suspension is subjected to a force that is often perpendicular to the direction of the flow, as shown in Fig. 1-2, to focus the particles in a well-defined location. Forces of different nature can be used, as for example electrical forces (Gascoyne and Vykovakal 2002; Voldman 2006; Zhu et al. 2010), acoustic radiation forces (Petersson et al. 2007), magnetic forces (Liu et al. 2009; Miltenyi et al. 1990) or even optical forces (Zhao et al. 2007). A recent review can be found in (Pamme 2007).

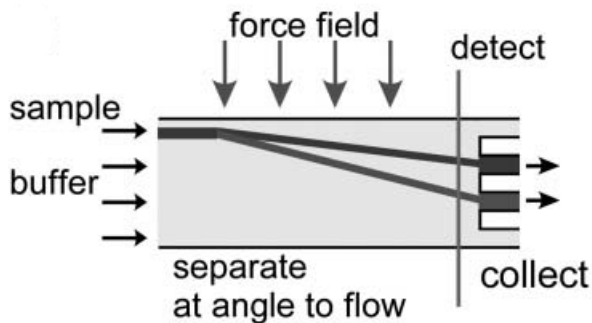


Fig. 1-2 Schematic of a typical active sheathless flow focuser. (Reprinted from Pamme (2007).)

Immunomagnetic separation (IMS) for example is an active sheathless flow technique commonly used for the separation of pathogenic organisms. The magnetic particles (MP), linked to specific antibodies, can be coupled to the target cells through antibody-antigen interactions forming MP-coated cells, and then removed from the suspension using a magnet (Hinds et al. 2003; Liu et al. 2009; Miltenyi et al. 1990). The main advantage of the magnetic actuation is that the magnetic field has no effect on biological samples that are usually diamagnetic, leading to excellent separation sensitivity.

Although these active microfluidic techniques are approved to be a successful biological application, the requirement of an outer force field increases the cost of fabrication, complicates the manipulation and decreases the throughput, thus giving an impediment to their widespread use.

### 1.1.2.2 Passive sheathless flow focusing techniques

Passive sheathless flow focusing techniques manipulate the particles without applying external forces, taking only advantage of the geometry of the microchannels and the hydrodynamic forces. These techniques involve mainly hydrophoresis (Choi and Park 2008), deterministic lateral displacement (Huang et al. 2004), gravitational methods (Huh et al. 2007) and inertial focusing (Di Carlo 2009).

Hydrophoresis utilizes slanted obstacles in a microchannel to guide and focus particles, as

illustrated in Fig. 1-3. The anisotropic fluidic resistance of the slanted obstacles generates a lateral pressure gradient which sets up a transverse flow. This secondary flow focuses particles depending on the size difference between the gap of the obstacle and the particle on specific positions (Choi and Park 2008; Choi et al. 2007).

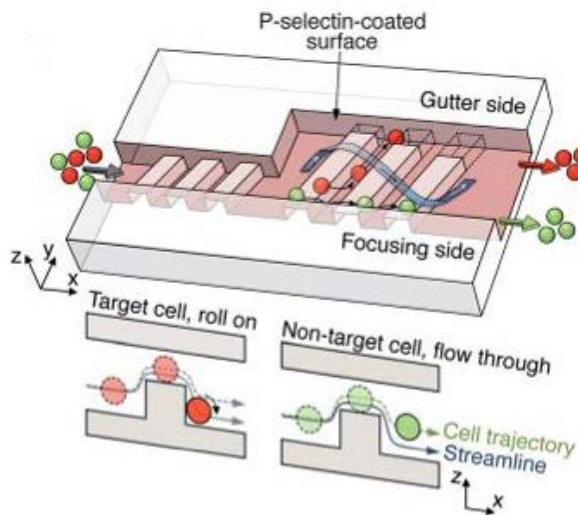


Fig. 1-3 Cross-sectional schematic of the device for hydrophoretic separation. (Reprinted from Choi et al. (2012).)

Deterministic lateral displacement uses an array composed of aligned triangular or circular posts to guide particles. Columns of posts are slightly offset in the direction perpendicular to the flow direction, making the array axis tilted an angle with respect to the fluid flow, as shown in Fig. 1-4. The tilt angle determines a critical diameter above which the particles will pass along angled array axis (red dashed trajectory) and below which particles will go straight following their initial streamline (green dashed trajectory) (Devendra and Drazer 2012; Loutherback et al. 2010).

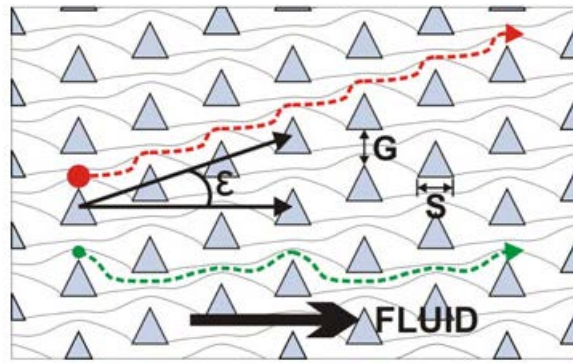


Fig. 1-4 Scheme of the Deterministic Lateral Displacement method. (Reprinted from Loutherback et al. (2010).)

Gravity-driven separation is based on the density difference between the particles and the carrier fluid. Although gravitational separation applies an external force field, it is considered passive because no other external active field is applied or modulated (Huh et al. 2007). Fig. 1-5 shows the gravity-driven device developed by Huh et al. (2007).

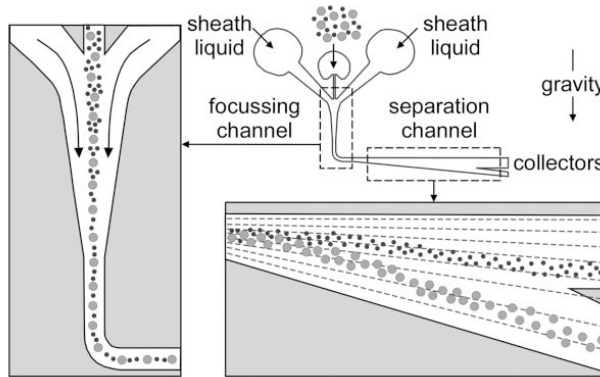


Fig. 1-5 Scheme of a gravity-driven separation device. (Reprinted from Huh et al. (2007).)

The particles are initially focused in the vertical direction and then are guided into a horizontal separation channel with gradually widening cross section where the flow velocity decreases and sedimentation starts to take effect. The sedimentation velocity of large particles is greater than that of small particles, resulting in a difference of vertical positions which makes it possible to separate the two particles.

Hydrophoresis and Deterministic Lateral Displacement methods, using the interaction between

the particles and the anisotropic geometry, can focus rapidly and in parallel a large number of different-sized particles. They present, however, a high risk of clogging because of the presence of obstacles and narrow gaps between them lead to high pressure drop across the device. Gravity can also be coupled to hydrodynamic flow (Huh et al. 2007), deterministic lateral displacement (Devendra and Drazer 2012) or acoustic field for particle separation (Petersson et al. 2007). But it is a mass-dependent sorting method, which cannot contribute to the manipulation of neutrally buoyant particles.

More recently, several sheathless passive focusing techniques based on differential inertial migration have been developed. Inertial microfluidic approach takes advantage of the regime of inertial fluid dynamics to focus suspended particles to predictable equilibrium positions within a microchannel. The inertial focusing rapidly expands due to the robust, simple, rapid, low-cost, and power-efficient operations involved (Di Carlo 2009). The last part of this chapter reviews the main works published in the literature in this field.

## 1.2 Phenomenon of inertial migration

Poiseuille (1836) was the first one to note the inhomogeneous radial distribution of blood corpuscles in capillary vessel. The corpuscles seemed to concentrate in an annulus close to the walls of the tube, indicating a lateral migration phenomenon.

These observations were quantitatively confirmed by the experiments of Segre and Silberberg (1962b) in the 1960s, whose work is considered as a milestone and triggered the interest of the scientific community in the inertial microfluidic field. They conducted experiments in a straight cylindrical tube (inner radius  $\sim 5.6$  mm) with rigid particles (diameter  $\sim 1$  mm) and observed that initially randomly dispersed particles were focused at a given distance from the channel inlet, on an annulus with a radius of about 0.6 times the tube radius, as shown in Fig. 1-6a. This phenomenon is known as the Segré–Silberberg effect or tubular pinch effect because of the tube-like shape of the annular region to which particles migrate (Segre and Silberberg 1962a). With the advancement in microfluidics, the observations of the same phenomenon have been

confirmed experimentally in microchannels in the recent years (Matas et al. 2004b).

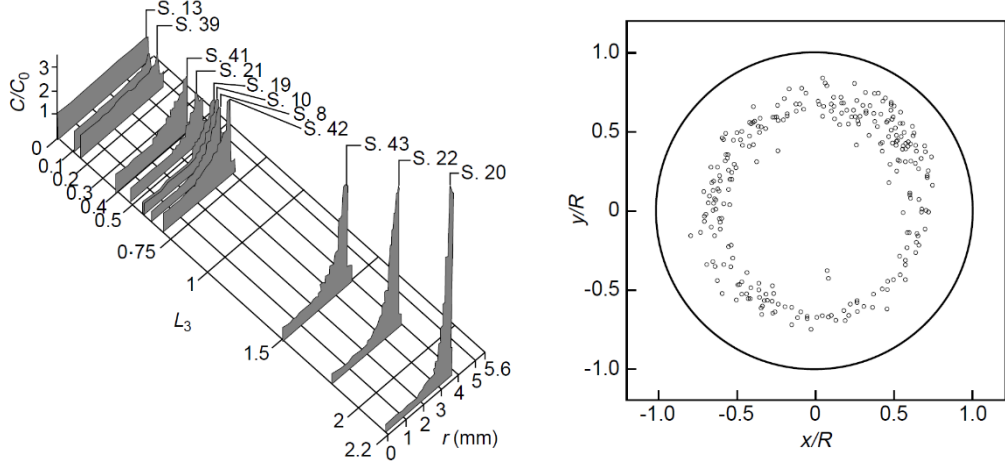


Fig. 1-6 Tubular pinch effect. The left image shows the experimental results of Segre and Silberberg (1962b), showing how radial migration develops in a cylindrical tube along channel. (Reprinted from Segre and Silberberg (1962b).) The right image shows the experimental distribution of particles in the cross section of a cylindrical tube at  $Re = 350$ . (Reprinted from Matas et al. (2004c).)

Following the observations of Segre and Silberberg (1962b), many investigators tackled the problem of inertia-induced particle migration theoretically (Asmolov 1999; Rubinow and Keller 1961; Saffman 1965; Schonberg and Hinch 1989), numerically (Abbas et al. 2014; Chun and Ladd 2006; Di Carlo et al. 2009; Nakagawa et al. 2015) and experimentally (Bhagat et al. 2008a; Bhagat et al. 2008c; Choi et al. 2011; Di Carlo et al. 2007; Kim and Yoo 2008).

Particle migrations in straight cylindrical channel and square channel were reported by Di Carlo (Di Carlo 2009). The initially randomly distributed particles focused on an annulus (known as the Segré-Silberberg annulus) in a cylindrical channel (Fig. 1-7a) and on four equilibrium lines located near the center of each channel face in a square channel for moderate values of Reynolds number (Fig. 1-7b), built on the average flow velocity  $U$  and the channel hydraulic diameter  $D_h$ :

$$Re = \rho U D_h / \mu \quad (1-1)$$

where  $\rho$  is the fluid density,  $\mu$  is the dynamic viscosity of fluid and  $D_h$  is defined as:

$$D_h = \frac{2HW}{(H + W)} \quad (1-2)$$

with  $H$  and  $W$  the channel height and width, respectively.

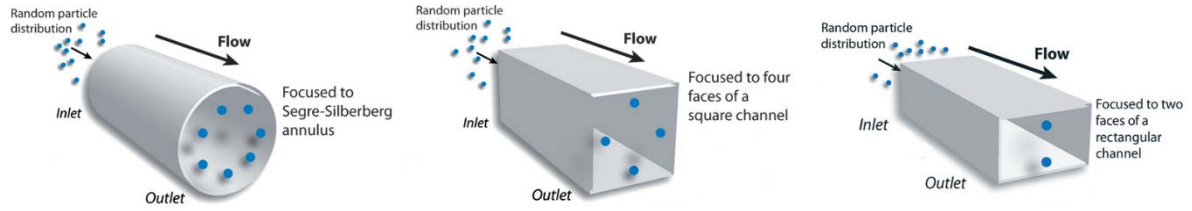


Fig. 1-7 Inertial focusing of particles in a cylindrical channel, a square channels and a rectangular channel, from left to right in the image, respectively. (Reprinted from Di Carlo (2009) and Amini et al. (2014).)

This result is however controversial: Bhagat et al. (2008c) experimentally and Chun and Ladd (2006) numerically proved that eight equilibrium positions coexist in square channels located at the four corners and near the four centers of each channel face.

It has been highlighted that the migration process takes place in two stages: the particles migrate first in the lateral direction forming a ring parallel to velocity iso-contours (pseudo Segré-Silberberg annulus) and then move cross-laterally toward the four equilibrium positions near the center of each channel face (Abbas et al. 2014; Choi et al. 2011; Zhou and Papautsky 2013). The second stage of migration, i.e., the cross-lateral migration, occurs only after that the first one is fully developed and is not significant at low  $Re$  (Abbas et al. 2014; Choi et al. 2011).

Depending on the aspect ratio of the cross-section and on the flow Reynolds number  $Re$ , particles in rectangular microchannels focus to two equilibrium positions centered on the large face of the channel as shown in Fig. 1-8 (Zhou and Papautsky 2013). In a similar two-stage way, particles first migrate towards the walls then towards the centerlines of the walls.

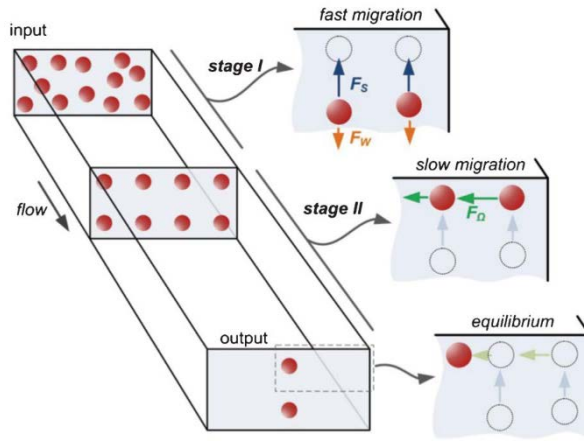


Fig. 1-8 Schematic drawing of inertial focusing in a rectangular microchannel. (Reprinted from Zhou and Papautsky (2013).)

### 1.3 Mechanisms of inertial migration for neutrally buoyant particles

Particles flowing in a microchannel are subjected to two types of forces: drag forces parallel to the flow and lift forces perpendicular to the flow. The drag forces act to accelerate the particles until they reach the fluid velocity and the lift forces related to viscosity and flow inertia carry the particles across the streamlines (Di Carlo 2009; Zhou and Papautsky 2013).

In straight channel flows, three primary lift forces contribute to the particle inertial lateral migration: a wall-induced lift force, a shear-induced lift force and a rotation-induced lift force (Zeng et al. 2009; Zhou and Papautsky 2013). In the case of a curved channel, a second-flow drag force must be taken into account (Martel and Toner 2013; Martel and Toner 2014). The balance of all the lift forces mentioned above will determine the migration process for a given channel flow.

The aim of this section is to present the different lift forces involved in the inertial migration process of neutrally buoyant particles.

### 1.3.1 Wall-induced lift force

A particle flowing through a microchannel interacts with the walls of the channel, unless the particle is extremely small or the wall is incredibly far away from the particle (Feng et al. 1994b; Martel and Toner 2014; Matas et al. 2004c). These interactions tend to repel the particle away from the wall. A sample streamline schematic is shown in Fig. 1-9. With the introduction of a particle close to the wall, the streamlines are diverted towards the side of the particle away from the wall and, which results in accelerated streamlines there. This asymmetric streamlines cause an imbalance of pressure on two sides of the particle, which generates a repulsive force, as shown in Fig. 1-9 (Feng et al. 1994b; Martel and Toner 2014). This force increases inversely with the normalized particle-to-wall distance (Zeng et al. 2009).

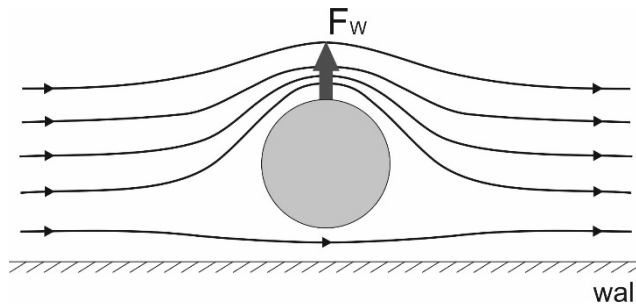


Fig. 1-9 Wall-induced lift force.

Di Carlo et al. (2009) gave an empirical equation based on numerical simulations (COMSOL Multi-physics) for estimating the wall-induced lift force  $F_W$ :

$$F_W = C_W \rho U_m^2 d_p^6 / D_h^4 \quad (1-3)$$

where  $C_W$  is a non-dimensional wall-induced lift coefficient, function of Reynolds number and position,  $\rho$  is the fluid density,  $U_m$  is the maximum flow velocity,  $d_p$  is the particle diameter and  $D_h$  is the channel hydraulic diameter.

### 1.3.2 Shear-induced lift force

In the case of quadratic velocity (Poiseuille) flow, the particle experiences a force produced by the curvature of the velocity profile (Feng et al. 1994b; Ho and Leal 1974). In a flow with a

typical parabolic velocity profile, it is generally assumed that the mean velocity of the neutrally buoyant particle relative to the fluid is null. But the relative velocity in the reference frame of the particle is higher on the wall side than on the centerline side as shown in Fig. 1-10. This dissymmetry causes a lower pressure on the wall side of the particle, directing the particle towards the wall (in fact, towards the area with increasing shear gradient) (Feng et al. 1994b; Ho and Leal 1974; Matas et al. 2004c).

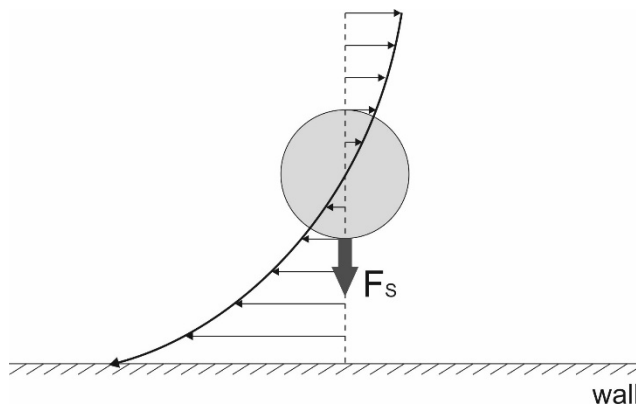


Fig. 1-10 Shear-induced lift force.

Di Carlo et al. (2009) also gave an empirical equation for the shear-induced lift force  $F_S$ :

$$F_S = C_S \rho U_m^2 d_p^3 / D_h \quad (1-4)$$

where  $C_S$  represents a coefficient of shear-induced lift, depending strongly on the Reynolds number and the particle position.

The balance of the shear-induced lift force and the wall-induced lift force successfully explains the first stage of inertial focusing in square and rectangular channel where the particles migrate towards the channel perimeter.

### 1.3.3 Rotation-induced lift force

The fact that in a square and rectangular channel, particles undergo a second stage of migration where they travel parallel to the walls towards the centers of the four faces implies that an additional lift force takes place. According to Zhou and Papautsky (2013), a third lift force is

attributed to the rotation of the particles, known as Magnus effect. Indeed, the rotation of a sphere in a flow creates a reduced pressure at the side where the rotation tends to increase the velocity of the fluid, in consistence with the perfect fluid mechanism suggested by Bernoulli's theorem (Feng et al. 1994b; Matas et al. 2004c). This imbalance in pressure causes a force as shown in Fig. 1-11.

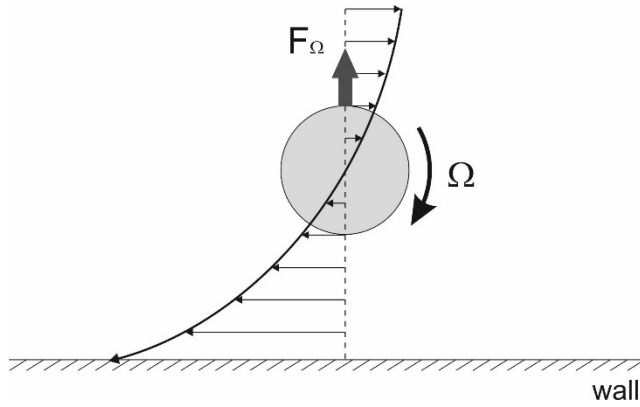


Fig. 1-11 Rotation-induced lift force.

Rubinow and Keller (1961) gave an equation to estimate the rotation-induced force  $F_\Omega$ :

$$F_\Omega = \frac{1}{8} \pi d_p^3 \rho \boldsymbol{\Omega} \times \mathbf{V} \quad (1-5)$$

where  $\boldsymbol{\Omega}$  is its angular velocity vector and  $\mathbf{V}$  is its relative velocity vector in the rest frame of the fluid. It acts against the flow velocity gradient in the direction of the center of the channel and its magnitude scales with the particle diameter cubed.

This rotation-induced lift force is negligible in comparison with the shear-induced lift force when the particles are far from the channel walls, i.e., during their first stage of migration (Feng et al. 1994b; Loth and Dorgan 2009) but becomes predominant in the wall region where the shear-induced and the wall-induced forces cancel each other, i.e., during their second stage of migration (Zhou and Papautsky 2013).

### 1.3.4 Secondary-flow drag force

In geometries more complex than straight microchannels, for example in a curved microchannel,

secondary flows (known as Dean recirculation flows) perpendicular to the main flow direction can occur. These secondary flows impart a drag force  $F_D$  (i.e., Stokes' drag) on the particle due to the difference between the particle velocity and the fluid velocity. This drag force is directed in the direction of the secondary flows (Martel and Toner 2013), as illustrated in Fig. 1-12.

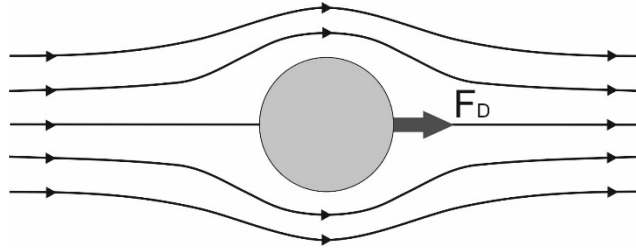


Fig. 1-12 Secondary-flow drag force, i.e., Stokes' drag.

In a Dean flow (a non-zero-Reynolds cured flow allows for a secondary flow), Zhang et al. (2016) utilized the Stokes' drag equation to calculate the secondary-flow drag force  $F_D$ :

$$F_D = 3\pi\mu d_p U_{SF} \quad (1-6)$$

where  $U_{SF}$  is the secondary flow velocity.

## 1.4 Influence of channel, particle and fluid characteristics on inertial focusing

The inertial focusing of particles in microfluidic devices strongly depends on the characteristics of the channel, the particles and the fluid (Di Carlo 2009). In this section a brief review of the literature dealing with the influence of these different parameters on the migration is presented.

### 1.4.1 Channel properties

Several physical parameters of straight channel that affect inertial focusing are mentioned in the literature and are reviewed here.

#### 1.4.1.1 Channel length required for focusing to equilibrium positions

Channel length required for particles to reach equilibrium positions is a crucial criterion for the

design of separation devices. However there is no consensus in the literature concerning the way to estimate this length.

Bhagat et al. (2008c) used the net lift force expression from the theory of Asmolov (1999) to propose an estimation of the microchannel length  $L_f$  required for particles to reach their equilibrium positions:

$$L_f = \frac{3\pi\mu}{2C_L\rho U_m} \left( \frac{H_R}{d_p} \right)^3 \quad (1-7)$$

where  $H_R$  is the narrowest channel dimension and  $C_L$  is the lift coefficient which is a function of particle position and Reynolds number ( $C_L \sim 0.5$ ).

Di Carlo (2009) gave another expression of this length calculated from the balance of the shear-induced lift force and the Stokes' drag in a straight rectangular channel:

$$L_f = \frac{\pi\mu W_R^2}{\rho U_m d_p^2 C_L} \quad (1-8)$$

where  $W_R$  is the longer channel dimension and  $C_L$  is the lift coefficient (the average  $C_L$  varies from about 0.02 to 0.05 for aspect ratios ( $H_R/W_R$ ) from 0.5 to 2).

However, both of these expressions only quantify the channel length required for the particles to fully-develop their first stage of migration, i.e., to reach the initial equilibrium annulus close to the walls. Zhou and Papautsky (2013) completed Bhagat's expression to take into account the second stage of migration inside the initial the center points of walls:

$$L_f = \frac{3\pi\mu D_h^2}{2\rho U_m d_p^3} \left( \frac{H_R}{C_L^-} + \frac{W_R}{C_L^+} \right) \quad (1.9)$$

where  $H_R$  is the shorter channel dimension,  $W_R$  is the longer channel dimension,  $C_L^-$  is the lift coefficient during the lateral migration and  $C_L^+$  is the lift coefficient during the cross-lateral migration.

### 1.4.1.2 Curved channel

As seen in Section 1.3.4, secondary flows called Dean recirculation flows can be generated in curved channels. Particle migration in such channels is found either towards or away from the center of curvature depending on the Reynolds number, curvature ratio and particle confinement ratio. The curvature ratio is defined as  $\delta = D_h/2R$  where  $R$  is the radius of curvature of the channel and the particle confinement ratio is defined by the ratio of particle diameter to the channel hydraulic diameter  $d_p/D_h$ . Fig. 1-13 is a representation of inner and outer focusing at a given Reynolds number ( $Re = 419$ ) for various curvature ratios and different particle confinements (Martel and Toner 2013).

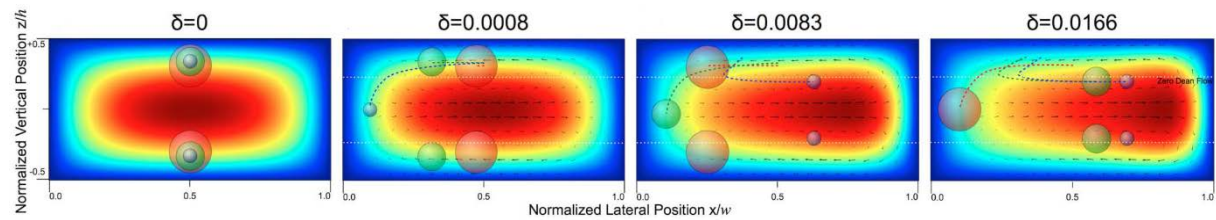


Fig. 1-13 Simulated velocity profiles, normalized Dean flow vectors and idealized particle equilibrium positions at  $Re = 419$ , for three different confinements ( $d_p/D_h = 0.066$  blue,  $d_p/D_h = 0.149$  green,  $d_p/D_h = 0.225$  red) in a straight channel ( $\delta = 0$ ) and increasing in curvature left to right. (Reprinted from Martel and Toner (2013).)

According to Martel and Toner (2013), these various particles distributions could be explained by the fact that the addition of curvature not only adds Dean drag to the force balance but also changes the shear gradient lift force through the redistribution of the velocity profile.

### 1.4.1.3 Cross-sectional shape

Circular, square and rectangular cross-sections are the most commonly used shapes for inertial focusing.

Particles focus to an annulus in a circular channel due to the radial symmetry of the channel and to the center of each channel face in a square channel because of the 4-fold channel

symmetry, as illustrated previously in Fig. 1-7 (Di Carlo 2009).

In the rectangular channels, the equilibrium positions have been shown to be the centers of the two long faces (Fig. 1-8) (Zhou and Papautsky 2013), but may also vary between these two positions and the four centers of each channel face, depending on the channel aspect ratio and the particle Reynolds number (Amini et al. 2014). Kim et al. (2016) studied the non-rectangular cross section channels and Fig. 1-14 illustrates the number and location of equilibrium positions in non-rectangular cross section channels.

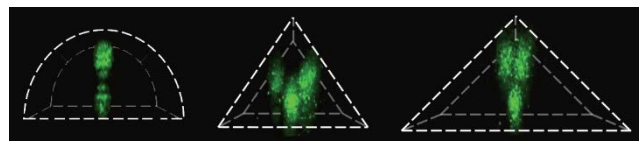


Fig. 1-14 Inertial focusing in non-rectangular channels, from left to right, half-circular channel, narrow triangular channel and wide triangular channel, respectively. (Reprinted from Kim et al. (2016).)

More recently, a trapezoidal cross-sectional channel has been studied in a curved channel (Wu 2012; Guan 2013). The trapezoid cross section modifies the velocity field in a Dean flow and amplifies the difference in equilibrium positions for particles of different sizes, thus resulting in higher separation resolution as compared to rectangular cross sections. Consequently, the large particles are focused close to the inner wall and the small ones are focused at the core of Dean vortices towards the outer wall, as illustrated in Fig. 1-15.

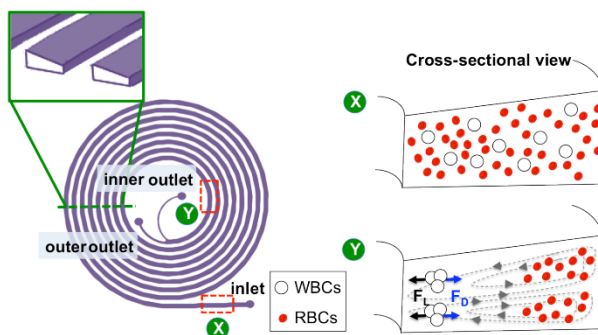


Fig. 1-15 Schematic of spiral channel with trapezoid cross-section indicating the inertial focusing of 10  $\mu\text{m}$  (white) and 6  $\mu\text{m}$  (red) beads. (Reprinted from Wu et al. (2012).)

#### 1.4.1.4 Cross section Variation along channel

The presence of any type of irregularity in the channel can induce secondary flows that act in addition to the inertial lift forces and modify the inertial focusing behaviors. Hur et al. (2011c), for example, developed a device consisting in an array of expansion-contraction reservoirs placed in series as illustrated in Fig. 1-16. Such a device utilizes microscale laminar vortices combined with inertial effects to achieve a size-selective trapping. At a sufficiently high Reynolds number, particles whose diameter is larger than a critical value are isolated in the reservoirs; while below the cutoff diameter, particles freely pass through the reservoir region. The particle isolation mechanism can be attributed to the fact that as the entrained particles enter the expanded sections, they are only subject to the shear-induced lift force, in the direction toward the vortex core because the neighboring wall is far away, as shown in Fig. 1-16. Large particles experience a larger lateral lift force, resulting in greater lateral migration compared to the one sustained by the small particles (Mach et al. 2011; Zhou et al. 2013b). So the particles above the critical diameter pass the detached boundary toward the vortex core where they remain isolated, orbiting in the vortex, whereas the particles below the critical value do not migrate sufficiently and remain in the focused streams, being flushed out of the device. This device was used for successful isolation of larger cancer cells from dilute blood (Hur et al. 2011c; Mach et al. 2011).

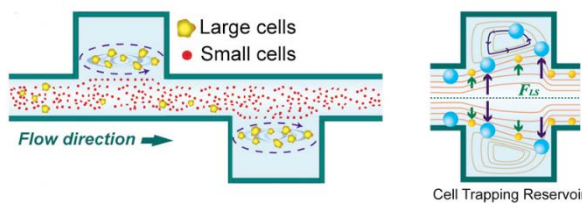


Fig. 1-16 Schematic diagram describing Hur's device composed of expansion-contraction reservoirs for particle separation. (Reprinted from Hur et al. (2011c).)

#### 1.4.2 Particle properties

Particle properties (e.g., size, shape or deformability) play an important role in inertial focusing. The detection and separation of particles from heterogeneous suspensions is of interest to

various research areas. Here some important particle properties that affect the inertial focusing are reviewed.

#### 1.4.2.1 Density

Although particle density can be assumed to be equal to that of the fluid for many cell-based applications, many industrial applications (e.g., industrial water filtration) may involve particles having density significantly different from that of the buffer solution (Martel and Toner 2014).

The study of Feng et al. (1994a) on vertical pipe flow demonstrated that in a Poiseuille flow with slightly buoyant particles, heavier particles which lag the flow will migrate towards the channel center and lighter ones which lead the flow will move towards the wall. For larger buoyancy, however, the final equilibrium position moves back toward the centerline. For non-neutrally buoyant particles, the migration is quite different from the neutrally buoyant particles mainly due to the presence of a significant Saffman's lift force (Matas et al. 2004c). This force, illustrated in Fig. 3-21, is due to the interaction of slip velocity and shear, arises when any force generates a slip velocity between particle and fluid (Saffman 1965) and is directed towards the side where the fluid velocity relative to the particle is the largest.

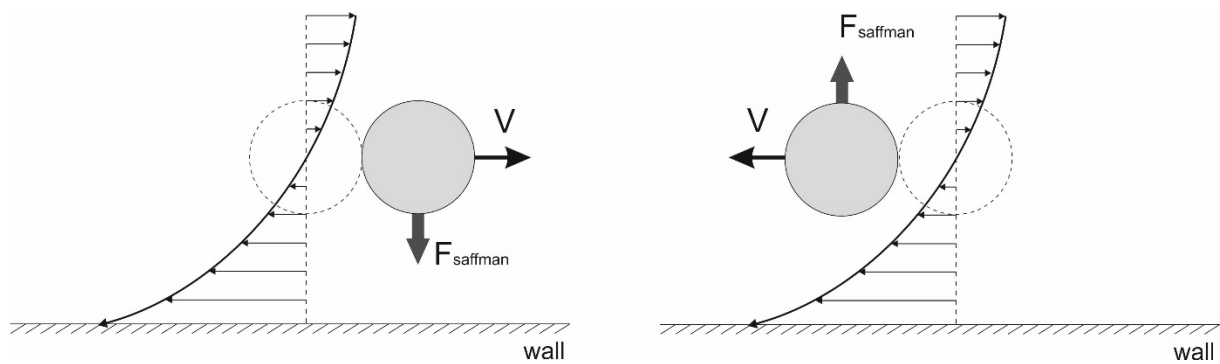


Fig. 1-17 Saffman's force.  $V$  is the relative velocity of the sphere.  $V > 0$ , the sphere moves faster than the fluid;  $V < 0$ , the sphere goes slower than the fluid.

#### 1.4.2.2 Shape

Although spherical particles are often used in inertial focusing studies for simplification, in

many of the real systems, non-spherical particles exist. Non-spherical particles can freely rotate and present different orientations while being sorted. Recently, some researchers (Hur et al. 2011a; Masaeli et al. 2012) have experimentally demonstrated that the inertial effects allow for the control and separation of non-spherical particles.

Hur et al. (2011a) investigated arbitrarily shaped particles with various sizes, cross-sectional shapes and asymmetries, in a straight rectangular microchannel. Nonspherical particles are found to be focused at distinct positions by inertial effects. The different cross-sectional shape of particles does not show a great influence to their equilibrium position, whereas the maximum diameter significantly affects the migration behavior and determines the final focusing location.

The particle maximum diameter is called the “rotational diameter” and the axis following this maximum diameter is the “rotational axis”. For a particle symmetric with respect to its rotational axis, focusing position was found to be determined by the rotational diameter regardless of its cross-sectional shape as shown in Fig. 1-18. While for highly asymmetric particles, focusing was found closer to the wall.

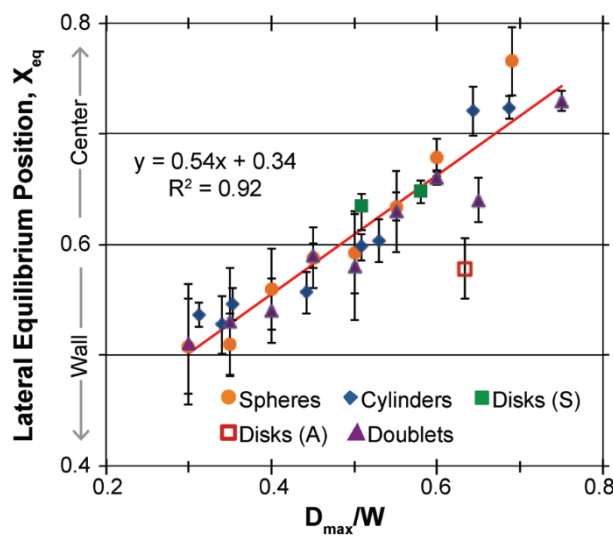


Fig. 1-18 Distance between the equilibrium position and the closest wall in function of normalized particle maximum diameter for various shapes. (Reprinted from Hur et al. (2011b).)

Masaeli et al. (2012) investigated the inertial focusing with ellipsoids of different aspect ratios

(as shown in Fig. 1-19) and developed a shape-based device using the particle's largest cross-sectional dimension as a distinguishing criterion, independently of the smallest particle dimension. They found that the particle focusing positions depend on the particle's largest cross-sectional dimension, being consisted with the results of Hur et al. (2011a). Rod-like particles (i.e., higher-aspect-ratio particles) are focused closer to the channel center than spherical particles with the same volume. Indeed, rod-shaped particles with 180° rotational symmetry follow the focusing trend of spheres with similar rotational diameter. This phenomenon is originated from the particle rotation: wall-induced lift force is strongly dependent on the particle-to-wall distance and becomes much stronger than the shear-induced lift force when the particles move away from the equilibrium position towards the wall. Therefore, for a rotating ellipsoid, when the major axis is perpendicular to the wall, it will be pushed away from the wall, contrarily, when the major axis is aligned with the flow, wall-induced lift force significantly decreases and the particle migrates back towards the wall.

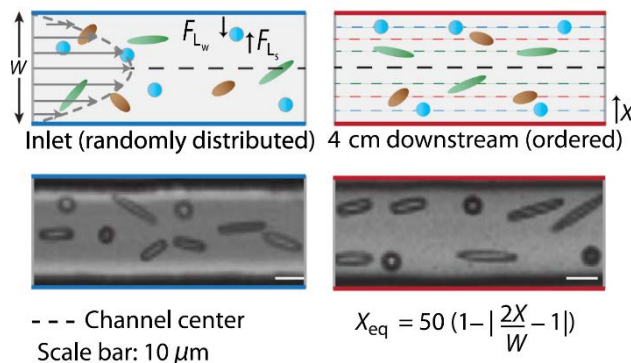


Fig. 1-19 Schematic and overlaid micrographs illustrating the inertial focusing of randomly distributed ellipsoid particles. (Reprinted from Masaeli et al. (2012).)

#### 1.4.2.3 Deformability

The study of inertial focusing of deformable particles shows great importance in biological applications since bioparticles such as cells, vesicles, and two-phase emulsion droplets are not rigid. In fact, the deformability strength of single cells is identified as an indicator of the cellular phenotype (e.g., various diseases are associated with cell deformability alterations including

cancer, blood diseases and inflammation.) (Hur et al. 2011b). Recently, single-cell deformability, recognized as a distinguishing marker, showed practical potential for cell separation to obtain target cells of interest in clinical and biological applications.

Recently, Hur et al. (2011b) demonstrated that the focusing equilibrium positions are affected by the deformability of cells and viscous droplets. The experiments were conducted with elastic particles and viscous oil droplets in a wide range of deformability (represented by the internal-to-external viscosity ratio  $\lambda = \mu_{in}/\mu_{ex}$ , where  $\mu_{in}$  is the dynamic viscosity of the fluid inside the droplet and  $\mu_{ex}$  the one of the continuous phase fluid). Fig. 1-20 shows that increasing deformability makes the particles move much closer to the channel centerline. This phenomenon is due to the balance of the inertial lift force (directed to the channel wall) and deformability-induced lift force (directed to the center of the channel). Hur et al. (2011b) took advantage of these separate lateral equilibrium positions to successfully classify cells of various size and deformability.

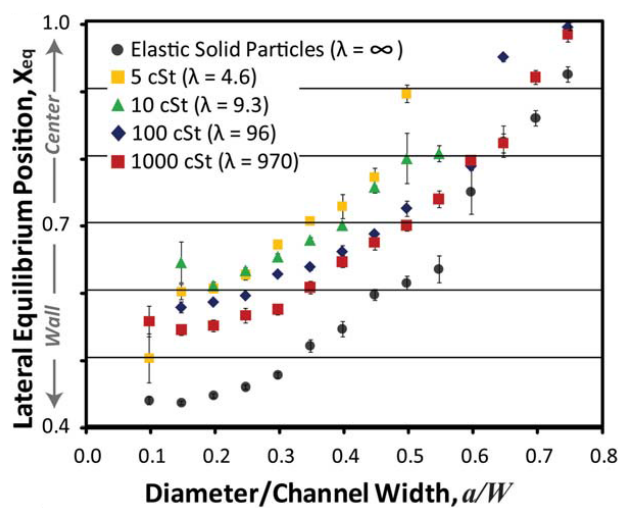


Fig. 1-20 Distance between equilibrium position and the closest wall in rectangular microchannels for viscous droplet and elastic particles of different particle diameter to channel width ratios and various viscosity ratio. (Reprinted from Hur et al. (2011b).)

### 1.4.3 Fluid and flow properties

#### 1.4.3.1 Effect of Reynolds number

Reynolds number, (i.e., ratio of inertial to viscous effect) can greatly influence the shear gradient force, resulting in the change of focusing behavior. Specifically, with  $Re$  increasing, the equilibrium positions in square or rectangular channels shift slightly towards the channel walls. Besides, in rectangular channel, two unstable equilibrium positions near the centers of the shorter channel faces become stable at high  $Re$  (Amini et al. 2014).

Ciftlik et al. (2013) investigated the focusing behavior of 10- $\mu\text{m}$  particles in a  $50 \times 80 \mu\text{m}^2$  rectangular channel for a wide range of  $Re$  (from 75 to 2,000). Both number and localization of the equilibrium positions change depending on  $Re$  as illustrated in Fig. 1-21. The equilibrium positions are located at the centers of the long faces when  $Re < 100$ , move to the centers of the four channel faces around  $Re = 150$ , are reduced to the initial two positions but slightly farther away from the walls when  $Re$  increases to 750, and finally disappear for  $Re > 2,000$ .

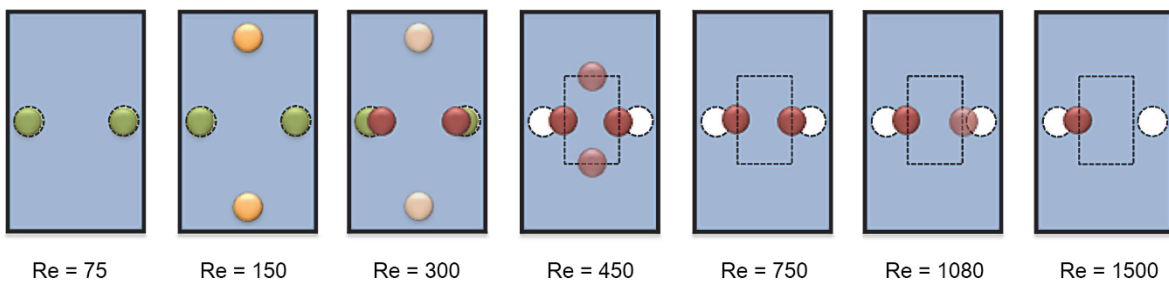


Fig. 1-21 Equilibrium positions within the rectangular channel cross section as a function of  $Re$ . (Reprinted from Ciftlik et al. (2013).)

#### 1.4.3.2 Concentration

Both the location and the number of equilibrium positions depend on the particle volume fraction, resulting in a large increase of particle-to-particle interaction (Amini et al. 2014).

Han et al. (1999) investigated extremely high concentrated monodisperse spheres in a tube flow with a solid volume fraction  $\Phi$  varying from 0.06 to 0.4. Two types of migration regimes have

been identified depending on  $\Phi$  and on the Reynolds number: the migration towards the channel walls and the migration towards the channel centerline caused by interparticle interactions. The different migration regimes in a tube as a function of  $\Phi$  and  $Re$  are illustrated in Fig. 1-22.

For diluted suspensions with high Reynolds numbers, pinch effect is dominant. Only the migration toward the channel wall is observed. For higher concentrated suspension (volume fraction = 0.2) and small Reynold numbers, only the migration towards channel centerline is observed. For even higher concentrated suspensions within all range of Reynolds numbers, both the migrations toward channel center and channel wall are observed, so the particles are found to be concentrated both at the center of the tube and on the Segré-Siberberg annulus.

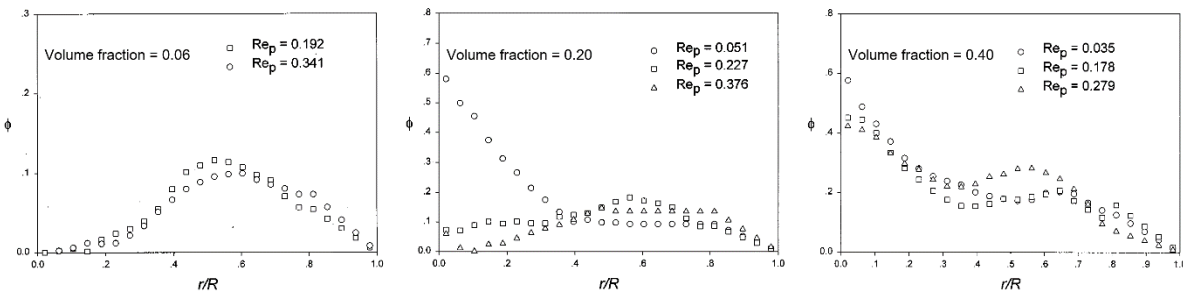


Fig. 1-22 Migration regimes in a tube as a function of particle volume fraction  $\Phi$  and Reynolds number  $Re$ . (Reprinted from Han et al. (1999).)

In rectangular straight channels, Lim et al. (2012) noticed that the equilibrium positions of cancer cells ( $d_p = 17.8 \mu\text{m}$ ) change from the center of the long faces for diluted blood suspension ( $\Phi < 0.15$ , i.e.,  $f_{RBC} < 0.33$ ) to the center of the short faces for original blood ( $\Phi = 0.45$ , i.e.,  $f_{RBC} = 1$ ), highlighting that the particle concentration seems to have a great influence on the particle focusing behavior, and thus is worth to be further studied.

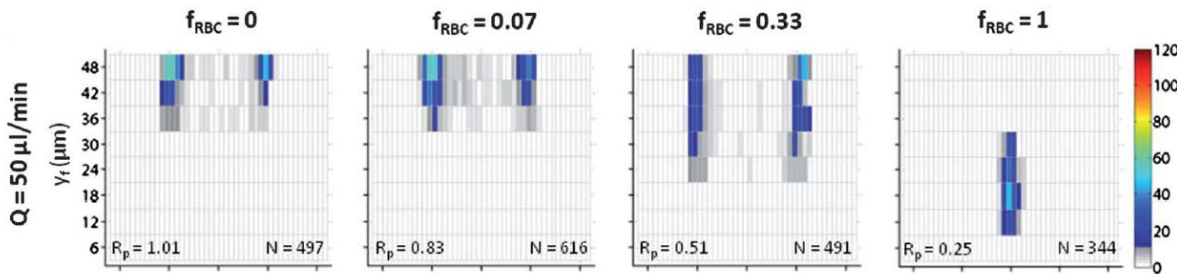


Fig. 1-23 Cancer cell distribution in a half of rectangular channel cross section at different flow and concentration conditions. (Reprinted from Lim et al. (2012).)

#### 1.4.3.3 Non-Newtonian fluid

Particles in viscoelastic fluids migrate in the direction of decreasing shear rate, which is toward the center of the channel for a Poiseuille flow. This modification in the migration behavior is due to the presence of a viscoelasticity-induced lift force acting on the particles. The inertial lift forces and the viscoelastic lift forces can be carefully balanced to make the particles focusing in a single line along the channel centerline, by controlling flow rate (Amini et al. 2014). The migration behaviors of neutrally buoyant particles in a non-Newtonian viscoelastic flow depends strongly on the volume fraction of solids, the blockage ratio of the channel, the effects of inertia and elasticity, and the effects of shear thinning. Since the intensity of the viscoelastic force acting on the particle increases with its diameter, large particles are more rapidly driven toward the centerline than the small ones. This different migration rates have been used by Nam et al. (2012) to successfully separate particles, as shown in Fig. 1-24.

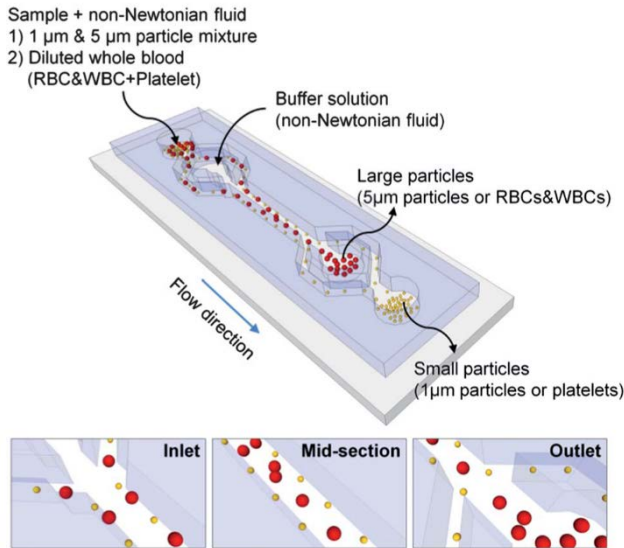


Fig. 1-24 Schematic diagram of size-dependent particle separation using elasto-inertial characteristics of non-Newtonian fluid flow. (Reprinted from Nam et al. (2012).)

## 1.5 Applications

Works conducted during the last two decades on inertial focusing have shown that this technique had a great potential in terms of practical applications. A variety of new applications based on this phenomenon is continuously developed and are mainly categorized into four types: particle separation, volume reduction, particle alignment, and solution exchange.

In this section, we will give a brief presentation of the recent progress and successful achievements for each type of application.

### 1.5.1 Particle separation

The most developed application of inertial focusing is the particle separation. In that case, different particles in a mixture have to be focused separately only based on their mechanical properties such as size, shape, and deformability. The difference in focusing can be due to a difference in the particles equilibrium positions (equilibrium separation) or in the particle migration velocity (kinetic separation).

It has been reported that the particle separation can be accomplished by using specific channel

geometry designs at a certain flowing conditions. For example, Mach and Di Carlo (2010) utilized a rectangular channel containing an expansion region with gradually increasing channel width to separate red blood cells (RBCs) from bacteria, as shown in Fig. 1-25. Zhou et al. (2013a) developed a rectangular microchannel with the modulation of aspect ratio whereby the fractionation of a mixture of 10- $\mu\text{m}$  and 20- $\mu\text{m}$  particles was realized, as demonstrated in Fig. 1-26.

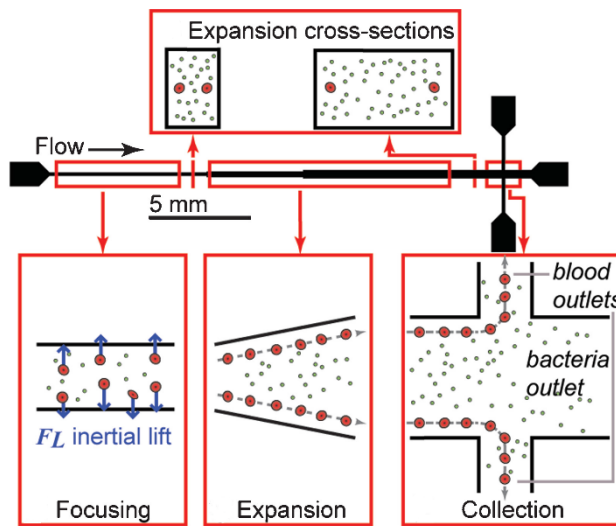


Fig. 1-25 Schematic of equilibrium separation in a straight channel with an expansion zone. (Reprinted from Mach and Di Carlo (2010).)

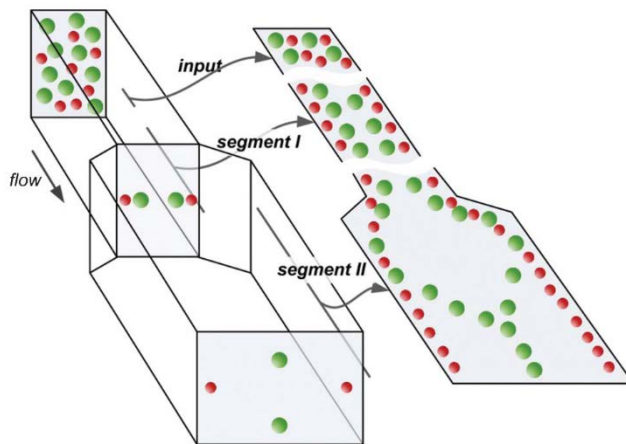


Fig. 1-26 Schematic of kinetic separation in a rectangular channel with modulation of aspect ratio. (Reprinted from Zhou et al. (2014).)

### 1.5.2 Volume reduction

Many of the separation methods can enrich particles at the same time. It is also possible to use inertial focusing to reduce the volume of a sample fluid, separately collecting the concentrated particle-rich streams and the remaining liquid. This technique shows great potential in water filtration (Martel and Toner 2014) and blood plasma separation from cells (Faivre et al. 2006; Yang et al. 2006). Some researchers take advantage of spiral channel geometry to achieve this volume reduction. For example, Seo et al. (2007) designed a double spiral channel (Fig. 1-27) with a transitional point near the center (P#3), resulting in a sharper and narrower band finally diverted into the inside outlet and the filtered water collected from the outside outlet.

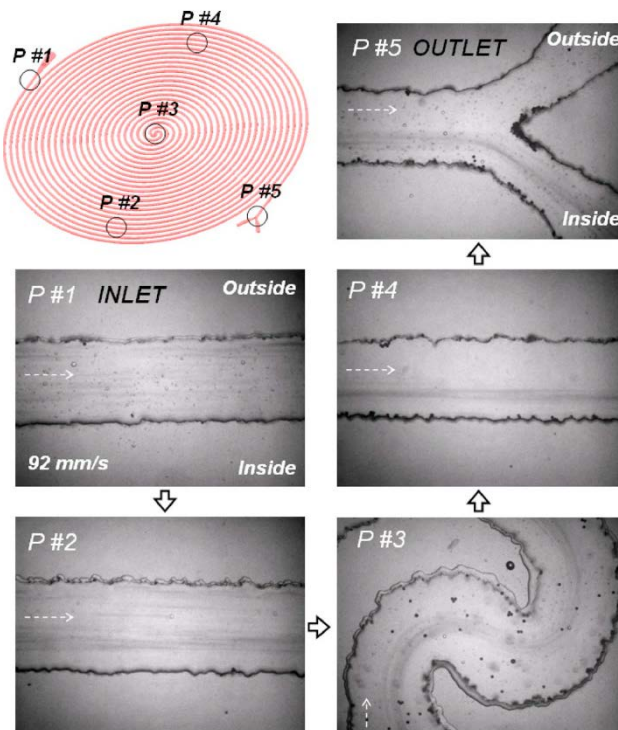


Fig. 1-27 Sequential images along a fluidic path in a double spiral channel showing the enrichment of particles. (Reprinted from Seo et al. (2007).)

### 1.5.3 Particle alignment

For many biological applications, especially cytometry, the precise positioning of cells near a detector with even spacing is of great importance to achieve accurate detection and analysis. Different from current commercial technologies based on sheath flows, technologies based on

inertial focusing to align particles show great advantages of high throughput and low cost, reducing the probability of overlap and out-of-focus blur. Although the fundamentals of particle streamwise ordering in microfluidic systems remain elusive (Zhou and Papautsky 2013), some applications based on this phenomenon have been reported. Hur (2010) developed a device consisting of 256 parallel high aspect ratio rectangular channels for flow cytometry with extreme throughput as illustrated in Fig. 1-28. Consequently, the cells are uniformly ordered along the channel walls at the outlet, allowing for an easiest detection. Edd et al. (2008) also developed a purely passive method using particle inertial focusing and alignment to control encapsulation of single-cells in a high aspect ratio microchannel. The cells are self-organized into two evenly-spaced streams, as depicted schematically in Fig. 1-29.

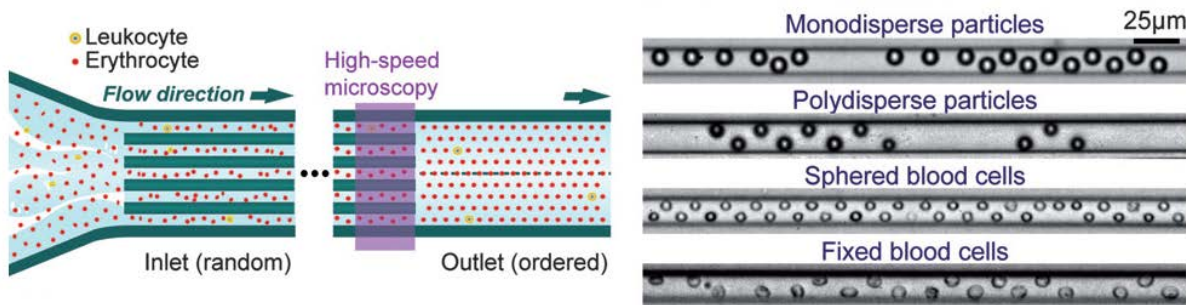


Fig. 1-28 Schematic of Hur's design for particle alignment. (Reprinted from Hur et al. (2011c).)

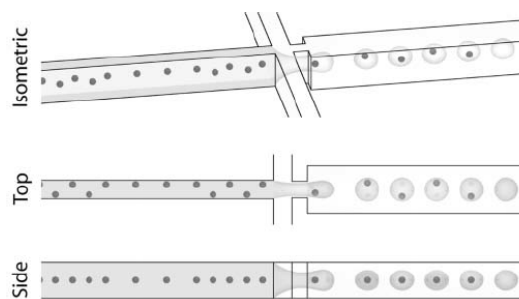


Fig. 1-29 Schematic of Egg's design to control single-cell encapsulation. (Reprinted from Edd et al. (2008).)

#### 1.5.4 Solution exchange

The technology to transfer particles quickly between disparate solutions is of great importance

in cell analysis studies. Several investigators have developed a new purely hydrodynamic approach based on inertial focusing for rapid inertial solution exchange with minimal mixing. Gossett et al. (2012) established a coflow by joining the cell-rich suspension with the exchange solution, in the way that the particles initially focused at the center of the suspension solution migrate across the fluid streamlines within the exchange solution at the center of co-flowing rectangular channel downstream. An illustration of this approach is depicted in Fig. 1-30. Finally the particles successfully cross the streams without significant disturbance of the interface at high rates.

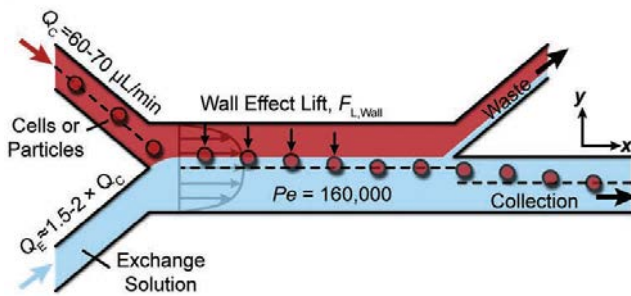


Fig. 1-30 Schematic of Gossett's device for rapid inertial solution exchange. (Reprinted from Gossett et al. (2012).)

## 1.6 Summary

We have first briefly reviewed the commonly used particle focusing techniques and highlighted the most promising passive sheathless techniques, that is, the inertial focusing. Then, after illustrating the inertial focusing phenomenon, the essential part of this chapter was dedicated to explain the fundamental dynamics of the particle motions: the inertial focusing is attributed to a balance of the lift forces involving the wall-induced force that pushes the particle away from the wall, the shear-induced force that drags the particle close to the wall, the rotation-induced force that forces the particle to move to the center of the channel face when it is close to the wall, and in some particular geometries the secondary-flow drag force. Various channel properties (length, curvature, cross-section shape, and variation of cross section), particle

properties (density, shape and deformability) and fluid and flow properties (Reynolds number, concentration and Non-Newtonian viscoelasticity) have also been separately discussed. Finally, we gave some important application examples, among which the particle separation is the principal application target of our work.

This chapter serves as a basis of the whole thesis work, providing the state-of-art of the inertial migration and also figuring out some inconsistency reported in literature such as the number of equilibrium positions in a square channel. To better understand the inertial migration mechanisms, the following chapters of this dissertation will be focused on the inertial migration of monodisperse neutrally buoyant rigid spherical particles in square channels, on the longitudinally ordered particle trains in both square and rectangular channels, and on a preliminary study of the migration of bidisperse particles in square channels.



# **Chapter 2. Methodology Development and Experimental Design**

Generally, the technologies for investigating particle migration in suspensions in microfluidic systems aim to determine the particle concentration or velocity profiles; and the spatial and temporal resolutions of a given technique determine the range of experimental conditions (e.g., flow rate, concentration, and particle dispersion) that can be appropriately investigated.

This chapter focuses on the methods for investigating the particle migration phenomena in microchannels, and on the experimental setups designed to implement these methods. This part of our work is based on a systematic study on currently available experimental techniques reported in literature.

We first give a brief introduction to the different existing techniques presenting their principles, pros and cons, as well as their range of application. Based on these, we then choose and develop two methods suitable for studying the particles in our flow conditions: the *in situ* visualization method and the particle projection method. For each of these two methods, the used materials, the experimental setup and the implementation are presented in detail.

## **2.1 Introduction to currently existing techniques**

In this section, several commonly used techniques (tomographic, ultrasonic and optical techniques) for studying suspensions in microfluidic devices are briefly presented, along with their suitability to measure and monitor particle behaviors (Van Dinther et al. 2012). The optical methods suitable for our experimental configurations are then highlighted.

### **2.1.1 Tomographic techniques**

#### **2.1.1.1 Electrical Impedance Tomography**

Electrical Impedance Tomography (EIT) is a technique where the difference in electrical conductivity is measured to determine the particle volume fraction profile using a relationship

between the local conductivity and the local suspension concentration (Ayliffe et al. 1999).

EIT is known as a relatively inexpensive technique with a good time resolution limit down to even 5 ms (Reinecke et al. 1998), but with a poor spatial resolution. It is hence capable of investigating the suspensions with high flow rates but is less capable of determining the particle focusing positions. It can also be used to measure the concentration profiles of concentrated suspensions (up to 40 % solid volume fraction (Butler and Bonnecaze 1999)). However, this technique it is not for frequent use due to the need of large difference in electrical conductivity between the particles and the fluid (Williams and Jia 2003).

#### 2.1.1.2 Nuclear Magnetic Resonance/Magnetic Resonance Image

Nuclear Magnetic Resonance (NMR) is able to distinguish the physical magnetic properties of the nuclei of different atoms and uses the so-called NMR relaxation times to probe the phase transitions and the molecular motions in solids and in liquids (Bonn et al. 2008; Caprihan and Fukushima 1990; Fukushima 1999; Han et al. 1999; Majors et al. 1989).

The main advantage of NMR and MRI is its capacity of measuring simultaneously various parameters such as concentration, velocity, chemical constituents, and diffusivity (McCarthy and Kerr 1998; Powell 2008; Van Dinther et al. 2012). These techniques have a common temporal resolution limit of 32 ms (Raguin and Ciobanu 2007) but relatively low spatial resolution (Altobelli et al. 1991). Suitable for both transparent and opaque media, they are able to detect the volume fraction, the physical behaviors and other properties even in highly concentrated suspensions (Brown et al. 2009; Lee et al. 2009; Raguin and Ciobanu 2007; Tallarek et al. 1998). However, NMR requires expensive equipment and trained staff (Altobelli et al. 1997).

#### 2.1.1.3 Neutron/X-ray Radiographies

Neutron Radiography (NRG) is one of the radiographic techniques which makes use of the difference of the attenuation characteristics of neutrons in material (Hibiki et al. 1994; Takenaka et al. 1993). X-ray Radiography is the act of obtaining a shadow image of an object using X-

ray attenuation (David et al. 2008; Heindel 2011).

These two techniques are noninvasive and have significant advantages when the visible light is not applicable like in complex geometry, opaque and multiphase flows (Mishima and Hibiki 1998). With neutron and X-ray radiographies, both concentration profile and velocity profile can be measured (Wu et al. 2007). The temporal resolution is found to be high; on the contrary, their spatial resolution are generally not high, e.g., less than 0.5 mm for X-ray computed tomography (CT) imaging (Heindel et al. 2008). However, they are not abundantly used because of the expensive equipment, specialized facilities and trained staff (Merlin et al. 2011).

## **2.1.2 Ultrasonic technique**

### **2.1.2.1 Ultrasonic Pulsed Doppler Velocimetry**

Ultrasonic Pulsed Doppler Velocimetry (UPDV) and Ultrasonic Velocity Profiler (UVP) are the most commonly used ultrasonic techniques, based on the measurement of the Doppler shift in the frequency of an ultrasonic wave that is scattered by a moving particle (Christopher et al. 1997; Wang et al. 2003).

Compared to the tomographic methods, the ultrasonic counterpart is cost-efficient in equipment and training. Spatial resolution limit is low (about 40 µm) and the temporal resolution can reach 0.02 s (Manneville et al. 2004). This technique can be used for opaque fluid flows (Manneville 2008), but only permits obtaining velocity profiles (Yamanaka et al. 2003). Moreover, it is impossible to study neither concentrated suspensions nor polydisperse suspensions, due to the multiple scattering and adsorption of ultrasonic waves (Yamanaka et al. 2003).

## **2.1.3 Optical techniques**

### **2.1.3.1 Laser Doppler Velocimetry/Laser Doppler Anemometry**

Laser Doppler Velocimetry (LDV) and Laser Doppler Anemometry (LDA) determine the particle velocity by comparing the frequency of the light scattered by particles with the interference patterns of two laser beams (Andersson and Rasmuson 2000; Bachalo 1994).

The spatial resolution of LDV can reach 4  $\mu\text{m}$  (Voigt et al. 2008) and the temporal resolution can be 10 ms (Di Leonardo et al. 2006). Both the concentration and the velocity profiles can be measured by LDA when the suspension is dilute enough (Chen et al. 1997; Koh et al. 1994; Lyon and Leal 1998a; Lyon and Leal 1998b). Another advantage is that the particle size can also be obtained simultaneously (Ayrancı et al. 2007). However, the refractive index of the particles needs to be matched with that of the fluid, leading to the use of a model suspension. The cost of this technique is high because of the laser equipment (Maru and Fujii 2010).

#### 2.1.3.2 Particle Tracking Velocimetry

Particle Tracking Velocimetry (PTV) is a technique to determine the particle velocity vectors by tracking the displacement and the trajectory of marker particles in consecutive images within an observation volume (Maas et al. 1993; Williams et al. 2010).

PTV typically uses low particle seeding density in order to avoid particle misidentification. One major advantage of this technique is that complicated flow fields can be analyzed (Adamczyk and Rimai 1988). Recently, the spatial resolution of PTV is improved to 2  $\mu\text{m}$  and the temporal resolution can reach 10 ms (Kikura et al. 2004; Lima et al. 2009; Williams et al. 2010). This technique is expensive and time-consuming due to the immense image data that must be stored and post treated (Adamczyk and Rimai 1988).

#### 2.1.3.3 Micro Particle Image Velocimetry

The Particle Image Velocimetry (PIV) is a method that utilizes correlation analysis of the position of particles in different images to visualize the flow structures where large numbers of instantaneous velocity vectors are yielded (Elsinga et al. 2006; Keane et al. 1995; Westerweel 1997; Williams et al. 2010).

The main advantage of micro-PIV is that it can give detailed information on instantaneous and ensemble-averaged flow fields in microfluidic devices (Lindken et al. 2006; Santiago et al. 1998). The in-plane resolution has been improved to the order of 1  $\mu\text{m}$  and the temporal resolution limit is 2  $\mu\text{s}$ , both depending on the camera characteristics (Meinhart et al. 1999).

The PIV is a high-image-density method, which is expensive and even more time intensive than the PTV (Keane et al. 1995; Stitou and Riethmuller 2001). Besides, it is not capable of measuring the concentration profile (Meinhart et al. 1999).

#### 2.1.3.4 Confocal Scanning Laser Microscopy

Confocal Scanning Laser Microscopy (CSLM) receives emitted light from a fluorescent sample excited by laser in a small volume, whereby tightly focused illumination and spatially filtered detection are combined to reduce the out-of-focus background and to produce high-quality images that display thin optical sections within thick fluorescent specimens (Choi et al. 2011; Derks et al. 2004; Dinsmore et al. 2001; Prasad et al. 2007; Sandison and Webb 1994; Webb 1996).

The more important feature of the confocal microscopy is its ability to deliver extremely thin in-focus images, and to allow gathering 3-D reconstructed information (Besseling et al. 2009; Isa et al. 2006). For most commercially available confocal microscopes, the optical resolutions are of the order of 180-nm laterally and 500-nm axially (Frank et al. 2003; Park et al. 2004; Prasad et al. 2007), and the temporal resolution limit is about 10 ms (Semwogerere et al. 2007). Concentration profiles and velocity profiles can both be determined by CSLM for polydisperse suspensions using different fluorescent dyes. This technique becomes limited for high particle concentration fluid (Besseling et al. 2009; Park et al. 2004; Sandison and Webb 1994).

#### 2.1.3.5 Fluorescence Correlation Spectroscopy

Fluorescence Correlation Spectroscopy (FCS) is a method where the fluctuations of the fluorescence signals from a particle in an observation volume are measured to obtain information about the processes (Bhagat et al. 2008b; Lumma et al. 2003; Magde et al. 1972; Thompson et al. 2002).

FCS has excellent spatial resolution in all 3 dimensions (~ 300 nm laterally, and 1.5  $\mu\text{m}$  along the optic axis) (Brister et al. 2005), and the temporal resolution is down to 10  $\mu\text{s}$  to access short time scales (Hashmi et al. 2007). Investigation of the dynamics of the flow at short time scales

can be achieved by simultaneously employing a high-speed camera. The concentration and velocity profiles as well as the particle sizes can be derived by FCS; however in high concentrated suspensions, scattering may limit the applicability of this method (Berland et al. 1995).

#### 2.1.3.6 Brightfield Microscopy

Brightfield microscopy is a conventional two-dimensional optical microscopy that utilizes the defocusing occurring as the particles move out of the objective focal plane, in order to extract the particle three-dimensional motion (Tasadduq et al. 2015).

This method is the simplest technique to depict the particle motion. The lateral spatial resolution cannot exceed  $0.2 \mu\text{m}$  and the temporal resolution is determined by the associated high-speed camera, usually  $\sim 2 \mu\text{s}$ . The main difficulty is to gather information along the optic direction. Recently, algorithms were proposed to achieve the localization of particles in this dimension by using the contrast and incremental change in blurriness of the particle image obtained when the particle moves in relation to the focal plane (Kim and Yoo 2008; Kloosterman et al. 2010; Rogers et al. 2007; Winer et al. 2014). However, this is only available in diluted suspension, to limit the heavy work in image analysis and data processing required for the three-dimensional localization (Lim et al. 2012).

This technique is adopted in our methodology development due to the capability of obtaining 3D particle information. Two methods depending respectively on high-speed brightfield imaging and fluorescence imaging are developed and described in the subsequent sections.

## 2.2 *In situ* visualization method

In this section a defocusing-based *in situ* visualization method is developed for identifying particle locations. The main principle of this technique is to first capture the particle migration images at different vertical positions, then to extract the particle distribution at each vertical position by identifying the in-focus and out-of-focus particles in the image, and finally to

reconstruct a 3D particle distribution within the whole microchannel.

In the following, we will detail the essential materials used in this technique (including the particles, the suspensions, the microchannels, the pump & syringe and the optical devices), illustrate the design of the experimental setup, and explain the implementation and data processing.

## 2.2.1 Materials

This section describes the materials along with their properties that are essential for the experiments design. The role of these parameters will be analyzed and discussed in the subsequent chapters devoted to the experimental results.

### 2.2.1.1 Particles

For particles, all the different properties such as material nature, shape, size, and density play an important role in the focusing behavior. Solid spherical particles of diameter ranging from 2 to 15  $\mu\text{m}$ , that is, in the range of microorganisms size, are selected. They are provided by the manufacturer in the form of a suspension with different particle volume fractions. Table 2-1 lists the monodisperse spherical particles used in this study. Indeed, the most important parameter that will be taken into consideration in the following experimental discussions is the particle diameter ( $d_p$ ). The majority of the experimental works are conducted using the 8.7- $\mu\text{m}$  latex spherical particles, to mimic the size of many typical particles found in microfluidic assays such as yeast cells (Sugaya et al. 2011).

Table 2-1 Summary of monodisperse particles.

Catalog No.	19814	PS/Q-R-L2580	A37307	18328
Mean diameter ( $\mu\text{m}$ )	1.925	5.31	8.7	15.66
Solids content (%), w/v)	2.56	10	4.1	2.75
Particle concentration (particles/ml)	$6.53 \times 10^9$	$1.22 \times 10^9$	$1.13 \times 10^8$	$1.30 \times 10^7$
Standard deviation ( $\mu\text{m}$ )	0.042	0.10	0.89	1.43
Coefficient of variation (%)	2.2	1.9	10.2	9.1
Material	Polystyrene	Polystyrene	Aldehyde/Sulfate latex	Polystyrene
Manufacturer	polysciences, Inc®	Microparticles GmbH®	Interfacial Dynamics	polysciences, Inc® Corporation®

### 2.2.1.2 Suspension

Neutrally buoyant particles have been used for all the experiments done in this work. The density of the polystyrene particles being  $\rho = 1,050 \text{ kg m}^{-3}$ , the density of the fluid is matched to that of the polystyrene particles by mixing deionized water ( $\rho=998.3 \text{ kg m}^{-3}$ ) with glycerol ( $\rho = 1,260.4 \text{ kg m}^{-3}$ ) in the volume ratio of 76.46 % / 23.54 % (v/v). The neutral buoyancy of the particles is confirmed by the fact that they neither settle down nor float on the surface after 24 hours in a container at room temperature.

The volume fraction of particles  $\Phi$ , indicating the particle concentration in suspension, is also an important parameter to be studied. The volume fraction used in this study ranges from 0.05 % to 1 % (and 0.1 % is the most frequently used, sufficiently low to get rid of the particle-to-particle interactions). In these conditions, the dynamic viscosity of the water-glycerol mixture is  $1.45 - 1.55 \pm 0.03 \text{ cP}$  at room temperature (Matas et al. 2004b).

### 2.2.1.3 Microchannels

In order to observe the particle positions by an *in situ* visualization method, hollow glass tubing (VitroTubes™) made of borosilicate have been used. The channels with different cross sections including square and rectangle, and different lengths used in this thesis work are summarized

in Table 2-2.

Table 2-2 List of microchannels used in our experimental studies.

No.	Section ( $\mu\text{m}^2$ )	Wall ( $\mu\text{m}$ )	Length (cm)
1	50 × 50	25	10
2	80 × 80	40	10, 30, 60
3	100 × 100	50	10, 30
4	300 × 300	150	30
5	50 × 500	50	30

The most commonly used channel in our study is the  $80 \mu\text{m} \times 80 \mu\text{m}$  square channel. Its cross section geometry has been visualized by a Scanning Electron Microscope (SEM), as shown in Fig. 2-1. The cross section has been prepared by a snap cut at the end of the channel to obtain a flat surface. The mean inner dimension (ID) and the mean wall thickness of the channel are measured on this image to be  $79.43 \mu\text{m}$  and  $39.42 \mu\text{m}$ . A fillet radius of  $4.19 \mu\text{m}$  is also visible at each inner corner. The channel cross section is thus considered to be square and was also verified with the CFD code Ansys-Fluent. Two numerical simulations have been conducted to analyze a simple Poiseuille flow (single phase flow) reproducing one of our experimental configurations, for two channels: the first one having a perfectly square cross section, the second one exhibiting the real cross-section as shown in Fig. 2-1. No significant differences in the flow structure have been observed between these two simulations.

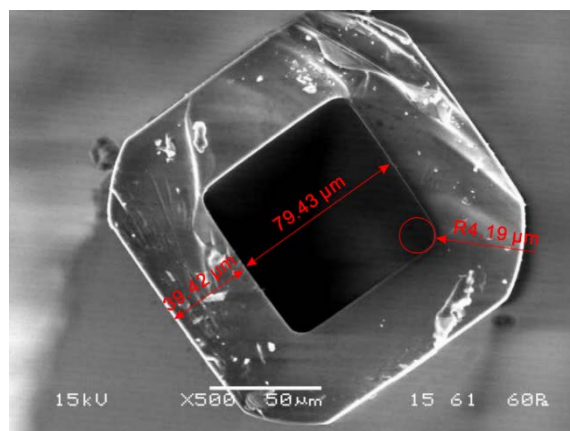


Fig. 2-1 Scanning Electron Microscope (SEM) image of the microchannel cross section ( $80 \mu\text{m} \times 80 \mu\text{m}$ ).

### 2.2.1.4 Pump and syringe

A syringe pump PHD 4400 (Harvard Apparatus) with three different sizes of stainless steel syringe (as listed in Table 2-3) has been used to generate flow rates ranging from 0.02 to 2,000  $\mu\text{L}/\text{min}$  with a precision of 1 %.

Table 2-3 Summary of stainless steel syringe used in the experiment.

Syringe No.	Size (mL)	Diameter (mm)
1	8	9.525
2	20	19.130
3	50	28.600

The flow rates in our studies were set between 0.5  $\mu\text{L}/\text{min}$  to 2,000  $\mu\text{L}/\text{min}$ , corresponding to a Reynolds number Re from 0.07 to 280 in a  $80 \mu\text{m} \times 80 \mu\text{m}$  square microchannel.

### 2.2.1.5 Optical devices

Two sets of optical devices (microscope with camera) have been used to observe the particles in the flow and to acquire the images.

The first set uses a Leica DM RXA2 microscope equipped with an external light source (Leica EL6000). An objective lens  $\times 20$  with a numerical aperture (NA) of 0.4 was used in most of our experiments, and an objective lens  $\times 10$  with a NA of 0.25 was used when the channel dimension was too large. The smallest increment in the focusing direction is 0.015  $\mu\text{m}$ .

The acquisition of images is ensured by using a CCD camera (pco.sensicam camera) and the corresponding software Camware. The camera has a high resolution of  $1376 \times 1040$  pixels and provides a wide range of exposure times from 500 ns to 3600 s, which makes it possible to take high quality pictures at great flow rate. The camera has a constant frame rate of 10 frames per second (fps).

The second set consists in an Olympus BX51 microscope equipped with a built-in Koehler illumination. The same objective lenses  $\times 10$  and  $\times 20$  were used in the same way as the above microscope. The smallest increment in the focusing direction is 1  $\mu\text{m}$ .

A Photron FASTCAM SA3 camera with its software Photron FASTCAM Viewer was used here. The camera has a resolution of  $1024 \times 1024$  pixels, a wide imaging frequency from 50 to 120,000 fps, and a smallest exposure time of  $2 \mu\text{s}$  independent of frame rate, which could make it possible to track the particles migration trajectory.

## 2.2.2 Experimental setup

The experimental setup of the *in situ* visualization method is illustrated in Fig. 2-2. The straight square/rectangular channel bonded to a planar glass substrate was connected via a 15 cm long Teflon tubing (ID = 0.81 mm) to the syringe at its inlet and to the atmosphere at its downstream end. A small cone was introduced between the tubing and the microchannel inlet to limit clogging problems.

Samples with particles were prepared by diluting the suspension to various concentrations (from 0.05 % to 1.0 %, v/v). The microchannel was horizontally held so as to get rid of the influence of the gravity. Suspensions containing microparticles were injected into the microchannel by the syringe at the wanted flow rates. The syringe with solution was agitated before to be mounted on the pump in order to maintain a uniform concentration. Before injection, the microchannel and the tubing were filled with deionized water to remove all air bubbles. In order for the flow to reach a steady state, we start to capture images 2 minutes after the start of the syringe pump. 2 minutes are enough whatever the tested flow rate and the channel length, according to the experimental work of Zerrouki (2012) realized in our laboratory.

The particle migration was observed under the microscope with the focal plane located at different vertical positions within the microchannel and at different positions along the channel. The exposure times varied from  $2 \mu\text{s}$  to  $5 \mu\text{s}$  depending on the flow rate, and the image intervals depend on the flow conditions and on the cameras. At least 2,000 images were captured to yield satisfactory results. The detailed implementation is presented in the next section.

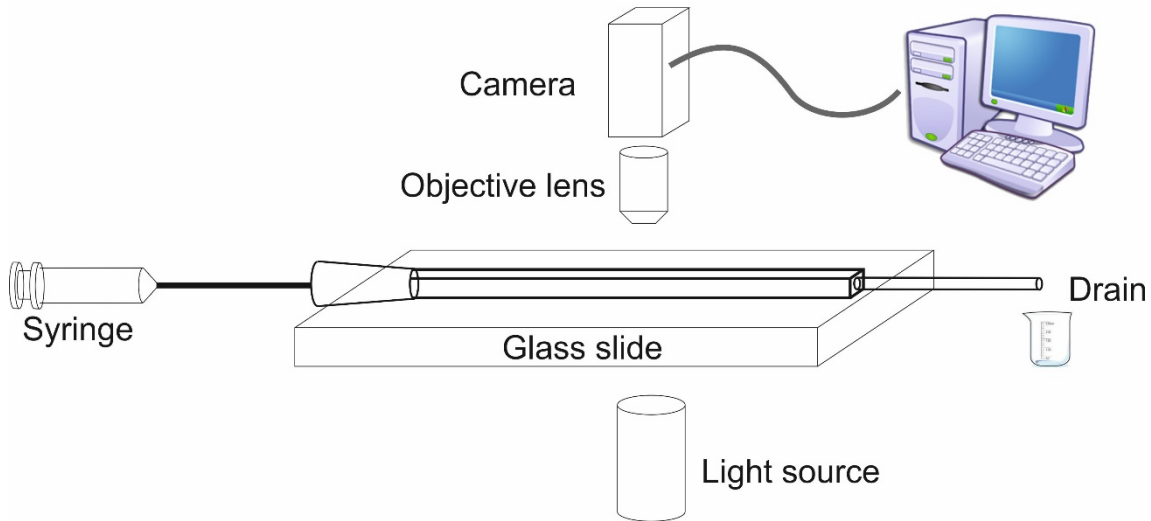


Fig. 2-2 Experimental setup of *in situ* visualization method.

### 2.2.3 Implementation

#### 2.2.3.1 Particle position relative to the focal plane

Fig. 2-3 shows an image of 8.7- $\mu\text{m}$  diameter particles flowing in a  $80 \mu\text{m} \times 80 \mu\text{m}$  square channel, at  $Re = 11.2$ , obtained near the channel outlet and at the channel midplane.

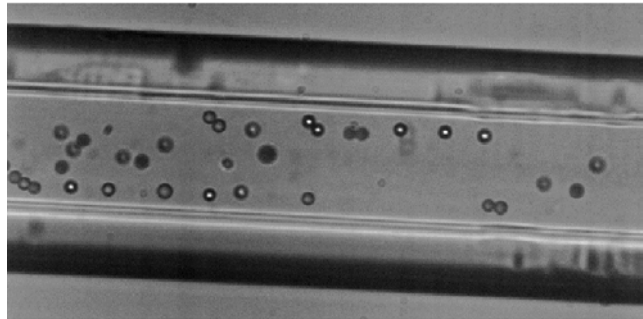


Fig. 2-3 Image of 8.7- $\mu\text{m}$  particles flowing in an  $80 \mu\text{m} \times 80 \mu\text{m}$  square channel with the focus at the channel midplane.

Particles with and without central bright points are observed in this figure. According to several previous experimental works (e.g., (Tasadduq et al. 2015)), particles with a bright point are in focus and those without a bright point are out of focus. However, the position of the bright point particles relative to the focal plane was not precisely known.

To answer this question, a drop of particle suspension was placed on a glass slide. After the

complete evaporation of the fluid, a large amount of particles were affixed onto the top of the glass slide. A line has been traced with a mark pen on the surface of the glass slide in order to accurately identify this surface under microscope. Fig. 2-4 illustrates this test and the corresponding images taken under the microscope.  $8.7 \mu\text{m}$  diameter particles were used. The fine-focusing knob of the microscope has a  $1 \mu\text{m}$  resolution along the vertical direction, ensuring a good distinction of the particle vertical position.

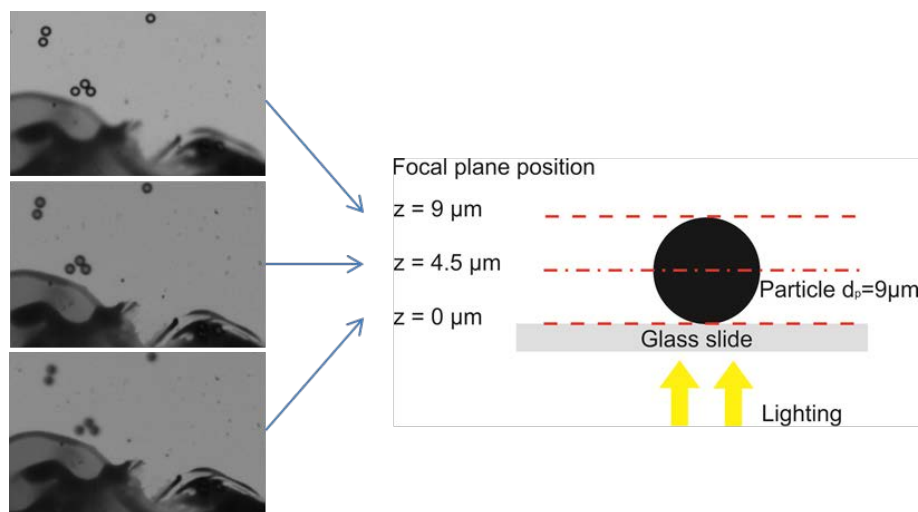


Fig. 2-4 Observation of a bright spot with the focal plane at the top of the particle.

First, the focal plane was adjusted to find out the glass slide surface, where the traced mark is most distinct, as shown in the left-bottom image of Fig. 2-4. In this position, the focal plane was at the bottom of the particle and the particles had blurred outline. Then we moved up the focal plane of  $4.5 \mu\text{m}$  to put it at the vertical center of the particles. The particles having well-defined outlines with a spot at the center were observed (Fig. 2-4 left-middle). We continued to move the focal plane up to the top of the particles and the visualized particles displayed well-defined outlines with high contrast, the outline and the center bright spots being easily distinguishable. We can thus conclude that the bright point is observed when the focal plane is located at the top of the particles.

#### 2.2.3.2 Localization process of the channel midplane

Now let us consider how to locate the focal plane in the microchannel. This is of great interest

because the difference of refractive indexes between the immersion medium of the objective lens and the studied object results in a difference of displacement between the objective lens and the focal plane in the microchannel.

Assuming that  $n_i$  is the refractive index of the immersion medium of the lens,  $n_f$  is the refractive index of the studied object, and the lens of the microscope moves along a distance  $\delta_{obj}$ , the displacement of the focal plane  $\delta$  is illustrated in Fig. 2-5 and can be calculated according to the following equation (Barrot Lattes et al. 2008):

$$\delta = \frac{n_f}{n_i} \delta_{obj} \quad (2-1)$$

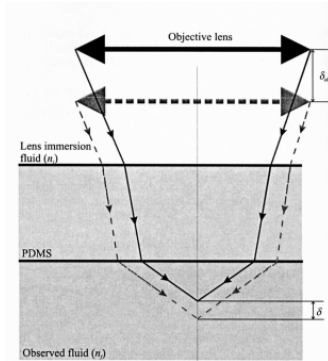


Figure 2 : Light path and relationship between lens and focal plane displacements

Fig. 2-5 Displacement of the objective focal plane. (Barrot Lattes et al. 2008)

In our case, the immersion medium of the objective lens is air with a refractive index  $n_{air} = 1$  and the microchannel is made of glass with a refractive index  $n_{glass} = 1.5$ , giving a theoretical displacement of focal plane in microchannel:

$$\delta = \frac{n_{glass}}{n_{air}} \delta_{obj} = 1.5 \times \delta_{obj} \quad (2-2)$$

This was confirmed by our experiments on a glass microchannel with an outside dimension of 160  $\mu\text{m}$  (Fig. 2-6a) placed on a glass slide. The top and the bottom of the microchannel were respectively marked by a blue line and a red line traced by mark pens, which are clearly visible under microscope but cannot be distinguished here in Fig. 2-6b since the images taken by the

camera are greyscale. We found that the objective lens must move a distance of  $106\text{ }\mu\text{m}$  to make the focal plane move from the top of the microchannel to the bottom. Besides, a red trace was additionally made on the surface of the glass slide just near the microchannel. We had to move the objective lens  $160\text{ }\mu\text{m}$  to displace the focal plane from the top of the microchannel to the glass slide surface in air (Channel outer dimension, OD =  $160\text{ }\mu\text{m}$ ). These results are consistent with Eq. (2-2), that is,  $160 = 1.5 \times 106$ .

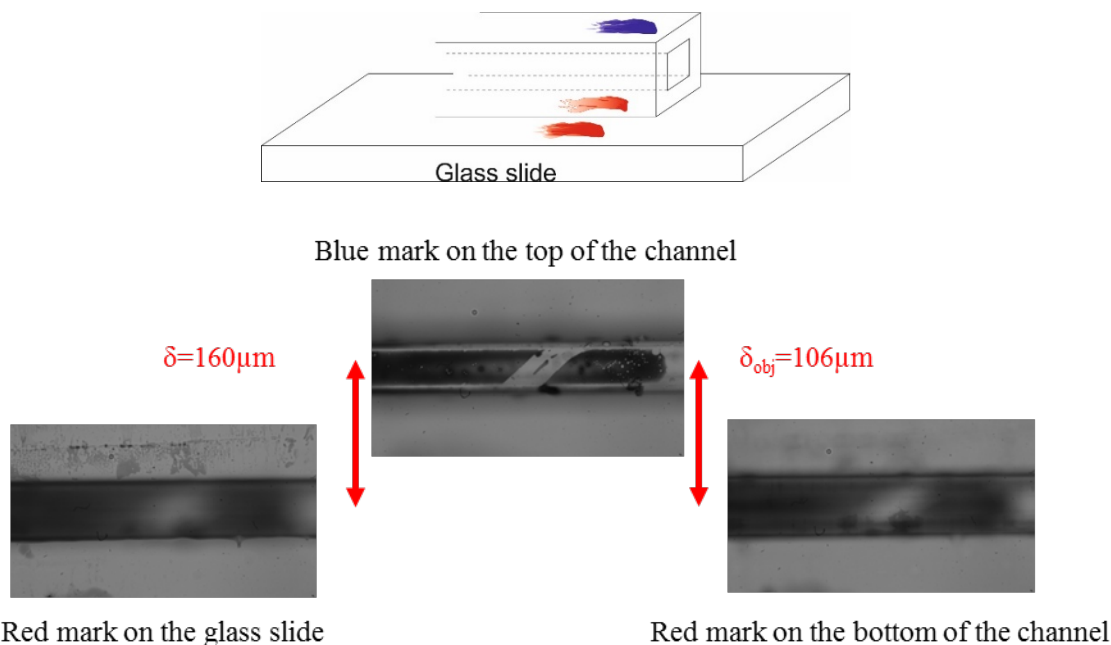


Fig. 2-6 Calibration of the displacement of the focal plane.

Considering that the refractive index of water is 1.33, that of glycerol is 1.45 and both are very close to that of the glass (1.5), when filled with particle suspension, the average refractive index ( $n_{avg}$ ) along the whole microchannel thickness is estimated to be 1.5 in order to simplify the calculation. The outside top and bottom walls of the microchannel can be easily located thanks to the small lines traced with makers. From these locations, the focal plane can be fixed at any vertical position within the microchannel, by displacing the objective lens obeying the relation given in Eq. (2-2). This was used at the beginning of each measurement in order to place the focal plane on the microchannel midplane.

Taking into account the average refractive index of the microchannel system ( $n_{avg}$  estimated to

be 1.5), considering that the best-distinguished particle image with well-defined outline and bright center spot is obtained when the top of the particle is in the focal plane, and according to Eq. (2-2), the downward displacement  $d$  of the objective lens from the top of the microchannel, needed to study the particles located at the channel midplane, is:

$$d = \frac{OD}{2 \times n_{avg}} - \frac{d_p}{2 \times n_{avg}} \quad (2-3)$$

where  $OD$  is the outer dimension of the microchannel and  $d_p$  is the particle diameter. Fig. 2-7 illustrates this displacement of the focal plane. For a  $80 \mu\text{m} \times 80 \mu\text{m}$  square channel with an outside dimension of  $160 \mu\text{m}$  filled with suspension of  $8.7\text{-}\mu\text{m}$  particles,  $d$  is calculated to be  $50 \mu\text{m}$ .

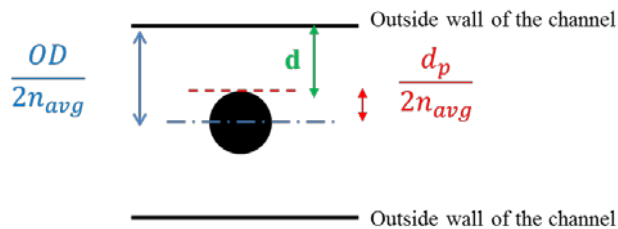


Fig. 2-7 Illustration of the localization process of the midplane of the channel

At this position indeed, not only the particles whose centers are located exactly at the channel midplane, but also the particles in a small range of vertical positions around the midplane, are in focus and can be observed with a bright spot. This is due to the depth of field and the depth of measurement of the microscope.

#### 2.2.3.3 Depth of field and depth of measurement

The depth of field is defined as the distance from the nearest objective plane in focus to the farthest plane also simultaneously in focus. The depth of field of a standard optical microscope objective lens is given by Inoué and Spring (1997) as:

$$\delta_z = \frac{n\lambda_0}{NA^2} + \frac{n}{M \cdot NA} e \quad (2-4)$$

where  $n$  is the refractive index of the fluid between the microfluidic device and the objective lens (in the present study  $n = 1$ ),  $\lambda_0$  is the wavelength of light in a vacuum being imaged by the optical system (in the present study  $\lambda_0 = 550$  nm),  $NA$  is the numerical aperture of the objective lens (in the present study  $NA = 0.4$ ),  $M$  is the total magnification of the system (in the present study  $M = 20$ ) and  $e$  is the smallest distance that can be resolved by a detector located in the image plane of the microscope (Meinhart et al. 2000). In our case, the resolution power of the CCD camera can reach 6.45  $\mu\text{m}$  and the range of  $e$  in the literature is reported between 4 and 24  $\mu\text{m}$ . Eq. (2-4) gives in these conditions an estimated theoretical depth of field of about 4.3  $\mu\text{m}$ . (In fact, the depth of field changes from 3.9 to 6.4  $\mu\text{m}$  for  $e$  ranging from 4 to 24  $\mu\text{m}$ )

The depth of measurement is considered here as the maximal vertical distance between the nearest in-focus particle to the farthest in-focus one simultaneously identified by our post-processing program. Meinhart et al. (2000) observed that the depth of measurement is sometimes slightly different from the depth of field and suggested to take into account the value of the particle diameter when it is high compared to the  $e/M$  ratio. The depth of measurement in this study was experimentally estimated as described below.

A 8.7- $\mu\text{m}$  dry particle was deposited on a glass slide and visualized under the microscope with the objective focal plane at different vertical positions successively separated with a step of 1  $\mu\text{m}$ . The corresponding images are shown in Fig. 2-8. The scale indicates the distance between the focal plane and the bottom of particle.

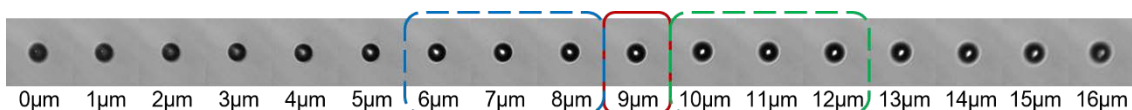


Fig. 2-8 Depth of the focus field calibrated by static particles with a step size of 1  $\mu\text{m}$ .

The image of the particle in the red rectangle, obtained when the focal plane is located at the top of the particle (8.7  $\mu\text{m}$ ), shows the best-defined outline and the brightest center spot. The three images at each side of this one, in the blue and green rectangles, also show well-defined outline and bright central spot. They are also considered to be in-focus by the post-processing

program. The particle images at the left side of the blue rectangle without clearly bright spots and those at the right side of the green rectangle showing blurry outlines are regarded as out-of-focus. The depth of field in this condition is estimated to be between 6 and 7  $\mu\text{m}$ .

To get closer to the real experimental conditions, the same tests have been carried out on a 8.7  $\mu\text{m}$  particle confined in a microchannel, where the particle is kept stable in suspension by blocking the inlet and outlet of the microchannel. Fig. 2-9 shows the particle in suspension observed at different vertical positions successively separated with a step of 1  $\mu\text{m}$ .

Similarly, 11 particle images, encircled by the red, blue and green rectangles, are considered to be in-focus by the post-processing program and the measurement depth here is about 10  $\mu\text{m}$ . This value is coherent with the one obtained for particles in the air. Indeed, due to the difference of refractive indexes between the immersion medium of the objective lens (i.e., air with  $n_i = 1$ ) and that of the particles (i.e., the suspension with  $n_{avg} = 1.5$ ), the depth of field in suspension is 1.5 times greater than that in air, and this depth of field difference certainly influences the depth of measurement value.

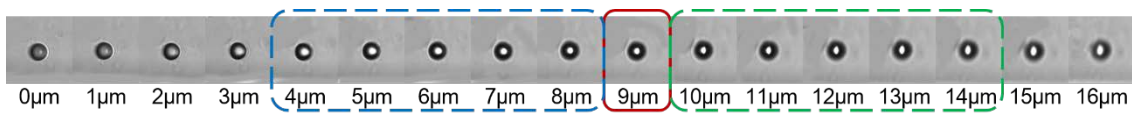


Fig. 2-9 Depth of measurement calibrated by static particles in suspension with a step of 1  $\mu\text{m}$ .

#### 2.2.3.4 Reconstruction of 3D particle distribution

The investigation of particle motion in three dimensions can be realized by directly tracking one particle to study its trajectory and velocity, as reported by Tasadduq et al. (2015). However this strategy is complex to implement in our case since in a straight channel, the lateral migration is a slow phenomenon, which implies very small lateral displacement in the field of view. In our study, we haven chosen to analyse the statistical distribution of a huge number of particles, to indirectly derive the particle migration behaviors. Therefore, all the particles in the flow need to be taken into account.

The particle positions in the two plan-view dimensions being directly read from the microscopic images, the challenge of our method is to identify the particle vertical positions. In order to minimize the number of images stored and the post-processing time, it is better to perform measurements with a relatively large increment in the vertical direction. Thanks to the depth of measurement ( $\sim 10 \mu\text{m}$  in this experimental condition), within which all the particles are observed in-focus, it is possible to perform the observation by dividing the  $80\text{-}\mu\text{m}$  channel height into eight vertical layers whose thickness is close to the depth of measurement, as shown in Fig. 2-10.

The observations have been realized at the seven separation planes between layers, thus at the vertical positions  $y/H = 0.125, 0.25, 0.375, 0.5, 0.625, 0.75$  and  $0.875$ . Indeed, the focal planes were slightly moved in order to make the particles centered on these positions exactly in-focus. (Eq. (2-3) was used to calculate the needed focal plane displacement (cf. Fig. 2-7). 2,000 images are captured and saved at each height to yield converged statistical results. The exposure times from the camera varied from  $2 \mu\text{s}$  to  $5 \mu\text{s}$ , depending on the flow rate.

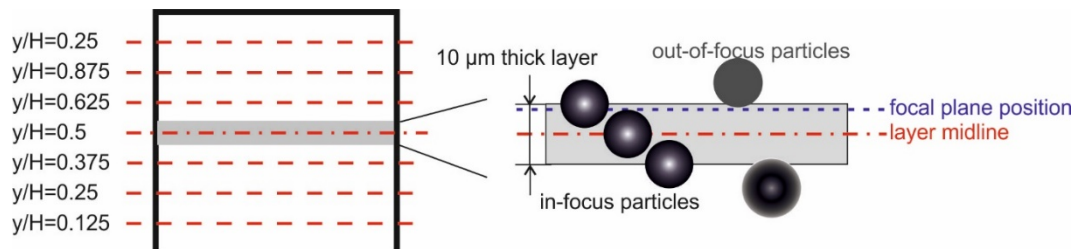


Fig. 2-10 Illustration of measurement layer in a microchannel

The 2D microscopic image obtained at the focal plane contains both in-focus and out-of-focus particles. The in-focus particles are considered to be within the layer around the corresponding vertical position  $y/H$ , and the out-of-focus particles are considered to be in other layers. This strategy is thus capable of reconstructing a 3D distribution of particles without physical slicing of specimens.

#### 2.2.3.5 Data processing for particles

The localization of in-focus and out-focus particles on each microscopic image is identified by

data processing using an in-house MATLAB code.

Fig. 2-11 illustrates the complete post-processing of a given image. From the original image (Fig. 2-3), the channel outside edges (Fig. 2-11a) are detected to localize the inside top and bottom walls and the inclination of the microchannel. The image is then rotated to reach horizontality (Fig. 2-11b) using a bicubic interpolation method, and cropped to keep only the zone between the inside channel walls (Fig. 2-11c). The background image evaluated from the total set of 2,000 images is subtracted from the image (Fig. 2-11d). The image is then converted from grayscale image to binary image (Fig. 2-11e). The identification of real particles is achieved by performing a series of morphological operations on the detected objects (Fig. 2-11f). Particles with a bright spot are considered as in-focus and are selected from all identified particles (Fig. 2-11g). Centers of in-focus particles identified in 2,000 images are replotted in the background image to visually show the distribution in this layer (Fig. 2-11h).

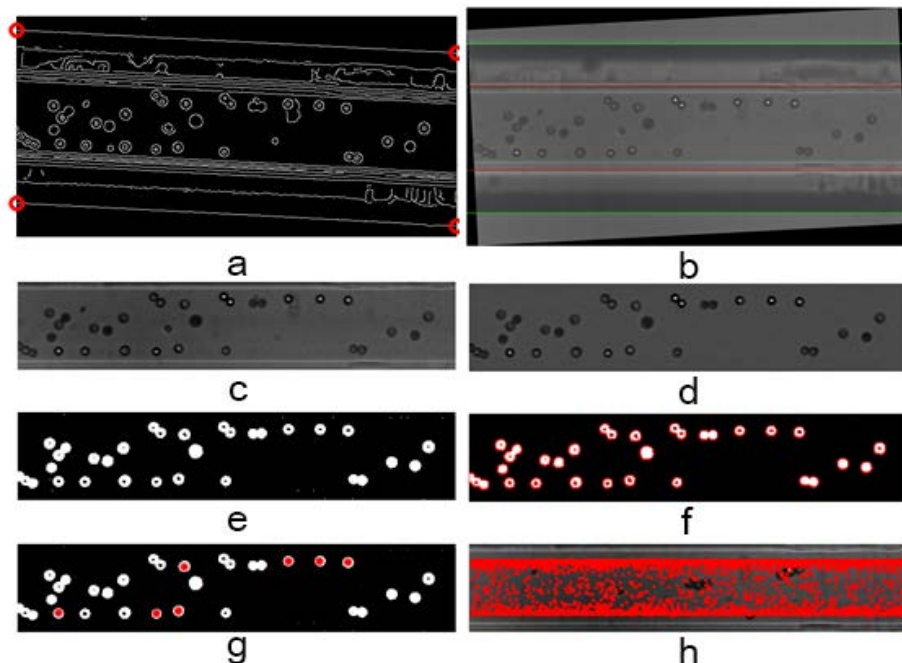


Fig. 2-11 Complete image post-processing. (a) Detection of channel edges and inclination; (b) Rotation of the microchannel; (c) Choice of the region of interest (d) Image after subtraction of background noise; (e) Conversion to a binary image; (f) Identification of real particles; (g) Selection of in-focus particles; (h) Overall in-focus particle positions summed from 2,000 images.

There are several points to be noticed:

- The two outside channel walls are identified by linear interpolation between the extreme points (red circles in Fig. 2-11b). This identification shows an error of  $\pm 1$  pixel.
- The grayscale image is converted to a binary one as follows: The grayscale background signal can be regarded to follow a normal distribution. Its standard deviation  $\sigma$  is evaluated with the full width at half maximum (FWHM). The value of  $3\sigma$  is chosen as the threshold in order to remove 99 % of the background noise. All the pixels with intensity stronger than the threshold are assigned “1” and those less strong are assigned “0”. Thus, “1” and “0” correspond respectively white and black in the binary image.
- The in-focus particles appear as white sphere with a black center spot on the binary image. But only those having a black spot sufficiently large are chosen by the processing program as in-focus particles. The exact positions of these particles are recorded and a second verification is performed on the grayscale image at the same position. This time, only the particles whose central spot reaches certain brightness are kept among the in-focus ones. The rest of the particles are all considered to be out-of-focus.
- Two particles can be attached or lay one on top of the other, as shown in Fig. 2-11g. These couples of particles are neglected in the statistical analysis since their very low percentage hardly affects the particle distribution results in suspensions with a low particle volume fraction.

The overall in-focus particle positions summed from the 2,000 images as shown in Fig. 2-11h are used to extract the spatial distribution of the particles at the corresponding vertical position, using the lateral probability density function (PDF), which is defined as Eq. (2-5):

$$f(x, y) \Delta s(x, y) = \frac{\sum_{k=1}^{k=2000} N_k(x, x + dx)}{T} \quad (2-5)$$

Where  $\Delta s(x, y)$  is the area of the bin,  $N_k(x, x + dx)$  is the number of in-focus particles between the lateral positions  $x$  and  $x + dx$  (Fig. 2-12a) at the  $k^{\text{th}}$  image,

$T = \sum_{x=0}^{x=H} \sum_{k=1}^{k=2000} M_k(x, x + dx)$  is the number of in-focus and out-of-focus particles calculated at  $y/H = 0.5$ , which is verified close to the sum of in-focus particles over all the vertical positions and all the images  $\sum_{y=0}^{y=H} \sum_{x=0}^{x=H} \sum_{k=1}^{k=2000} N_k(x, x + dx)$  (the channel width is normalized by the hydraulic diameter, i.e., the channel width  $H$ ).

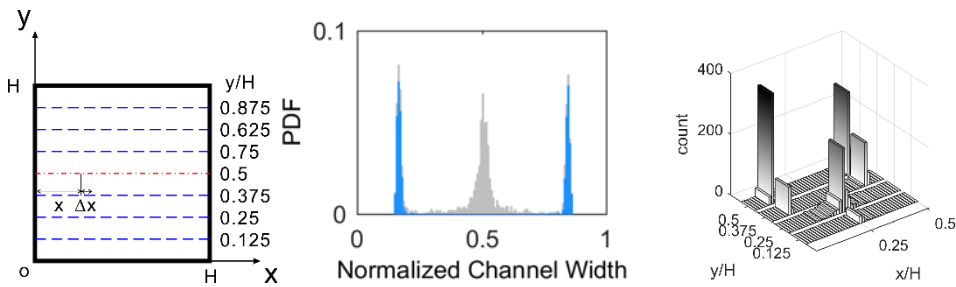


Fig. 2-12 PDF calculation method. (a) Measurement planes. (b) Example of a PDF histogram. (c) Example of a 3D histogram.

Fig. 2-12b shows a typical PDF for 8.7- $\mu\text{m}$  test particles with  $\text{Re} = 112$  obtained at the channel midplane ( $y/H = 0.5$ ) and at  $z/H = 1,000$ . The x-axis represents the normalized channel width and the y-axis represents the PDF as calculated above. The blue peaks correspond to the in-focus particles and indicate the position where the particles are likely to be focused (near the channel walls in this example). The height of the peak reveals the amount of particles accumulated at this position and suggests the degree of inertial migration. The gray peak at the middle of the channel width corresponds to all the particles observed at this vertical position, and serves as complementary information that gives an embryo idea on the distribution of particles over other vertical positions. Here this peak is almost at the same height as the others, suggesting an accumulation of a great number of particles near the center of the channel bottom. A complete 3D distribution of particles can be reconstructed by assembling the PDFs at all the vertical positions. (Fig. 2-12c)

## 2.3 Particle projection method

The particle projection method was developed by our collaborator Lafforgue-Baldas et al. (2013)

at LISPB (Toulouse, France), to study the particle migration at the micro scale. The fluorescent particles, after migration within the channel, are harvested on a plane filtration membrane put perpendicularly at the outlet of the channel. Their distribution on the membrane is then observed by an epi-fluorescent microscope. This device was used in the present study to directly visualize the particle distribution in the microchannel cross section. In this section, we will present in detail the materials, the experimental setup, and the implementation of this method.

### 2.3.1 Materials

#### 2.3.1.1 Particles and suspension

Two types of polystyrene fluorescent microspheres (Thermo Scientific, USA) with a density of 1,060 kg/m<sup>3</sup> were used in this study. The suspension was prepared by diluting the particles in filtrated Milli-Q water. Green particles emitting fluorescence at 508 nm (excitation wavelength at 468 nm) have a diameter of 4.8 μm and a concentration of  $6.4 \times 10^4$  particles/mL in suspension; and red particles emitting fluorescence at 612 nm (excitation wavelength at 542 nm) have a diameter of 8.7 μm and a concentration of  $7.82 \times 10^4$  particles/mL.

#### 2.3.1.2 Filtration membranes

The filtration membranes should be permeable enough to reduce the expansion of the streamlines coming from the micro-channel but also sufficiently rigid not to be modified by the pressure variations. Intermediate permeability acetate cellulose membranes ( $80,000 \text{ L} \cdot \text{h}^{-1} \cdot \text{m}^2 \cdot \text{bar}^{-1}$ ) with a mean pore size of 1.2 μm (Sartorius) were therefore used.

#### 2.3.1.3 Optical devices

The fluorescent particles deposited on the membrane surface were observed using an epi-fluorescence microscope (Leica DM 4000B) equipped with specific filters corresponding to the excitation and emission wavelengths of the dyed particles. The magnification of the selected objective lens was × 10.

### 2.3.2 Experimental setup and implementation

A specific experimental device as illustrated in Fig. 2-13 was used for particle projection method. It consisted in two branches. In the first one, a 8 mL stainless steel syringe ③ filled with diluted suspension was pushed by a syringe pump (HARVARD® 1000) ④ in order to generate flows at a precisely controlled flow rate. The syringe was connected through a plastic tube of inner diameter equaling 0.78 mm (Swagelok®) to the microchannel ① which is typically  $80\text{ }\mu\text{m} \times 80\text{ }\mu\text{m}$  square channels with a length of 30 cm in this study. The microchannel was nested by a 28 cm-long stainless steel tube for protection. In the second branch, water filtrated by Milli-Q (0.22  $\mu\text{m}$ ) was flowing to the filtration system ⑨.

The selected micro filtration membrane was mounted in the membrane holder ②. Before launching the HARVARD pump, the whole system was first filled with water in order to make the microchannel be surrounded with water and to create a jet at its outlet, thus eliminating local perturbations due to gas/liquid interface. The distance between the membrane and the channel outlet was controlled by adjusting the channel vertical position using a micrometric screw ⑩. On the basis of their numerical simulations (COMSOL Multiphysics®), Lafforgue-Baldas et al. (2013) recommended 500  $\mu\text{m}$ . An inspiratory pump (Masterflex, Bioblock scientific, USA) ⑦ was then run on to monitor the filtration conditions (transmembrane pressure), and a manometer (Mano-Thermo) ⑥ was used to check the integrity of the membrane. Finally, the syringe pump was run on at the selected flow rate for the required time to get a sufficient number of particles deposited on the membrane. After that, the membrane was removed and observed under an epi-fluorescent microscopy.

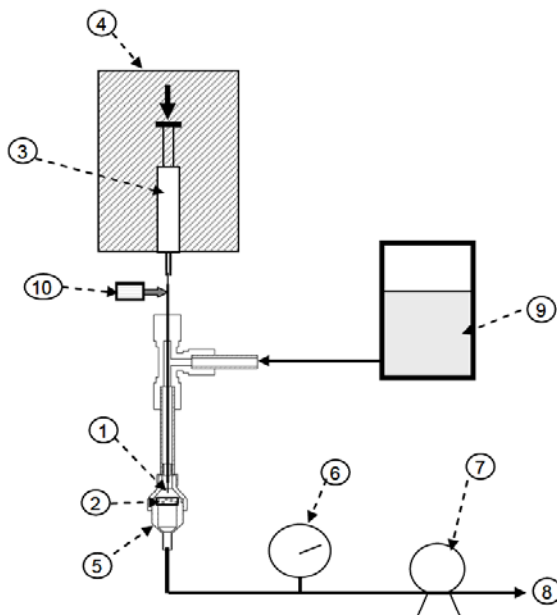


Fig. 2-13 Experimental setup of particle projection method. ①: microchannel; ②: membrane; ③: stainless steel syringe; ④: syringe pump; ⑤: membrane holder; ⑥: manometer; ⑦: pump; ⑧: liquid outlet; ⑨: filtered water; ⑩: micrometric screw. (Lafforgue-Baldas et al. 2013)

### 2.3.3 Data processing

The distribution of particles harvested by the membrane was visualized by an epi-fluorescent microscopy, whereby the fluorescent images captured by a camera are assembled to have an overall view of the channel cross section as shown in Fig. 2-14.

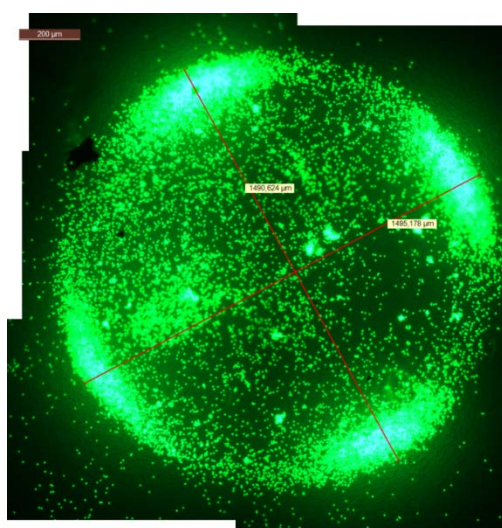


Fig. 2-14 Fluorescent image illustrating the distribution of particles in the cross section.

On the basis of a theoretical model developed to simulate the flow in the filtration chamber, Lafforgue-Baldas et al. (2013) assumed that, in these experimental conditions, particles follow the streamlines from the outlet of the microchannel until they reach the membrane and that the molecular interaction forces allow the particles to adhere as soon as they get in touch with the membrane. The visualized shape of particle deposit correspond thus to the particle spatial distribution in the outlet cross section of the channel.

It should be noticed that no statistical analysis has been carried out since this method is used in our study mainly as an additional means to verify the particle distribution (equilibrium positions) observed using the *in situ* visualization method.

## 2.4 Summary

The *in situ* experimental setup developed in the present work allows the visualization at different heights in channel and different distances from channel inlet in the real flow conditions. It thus gives access to the cross-sectional particles distributions all along the channel and next to the inertial focusing evolution. This is the main advantage of this method compared to other visualization setups found in the literature (e.g., (Bhagat et al. 2008c)) which did not permit to visualize particles in different vertical planes. In addition, the projection method will also be used to confirm and complete the results of this *in situ* visualization method.

# Chapter 3. Lateral Migration in Monodisperse Suspensions

Particle migration in a straight square microchannel, exhibiting quite different equilibrium positions compared to the one observed in pipe flows, was first reported by Di Carlo et al. (2007). He observed that randomly distributed particles focus to four point attractors near the center of each channel face. Nevertheless, in the literature a number of inconsistencies have been reported, for example, not only four (Abbas et al. 2014; Di Carlo et al. 2007) but also eight (Bhagat et al. 2008b; Bhagat et al. 2008c; Chun and Ladd 2006) equilibrium positions in square microchannels have been described. As seen in the Chapter 1, these equilibrium positions result from a balance of a wall repulsion force and a “particle shear” lift that pushes the particle towards the wall (Choi et al. 2011; Lim et al. 2012). Hence, the transverse equilibrium position is where the sum of these two oppositely directed forces becomes zero in the cross section of the channel. (Ciftlik et al. 2013; Di Carlo 2009; Martel and Toner 2014) Although the basic physics of this force balance is still argumentative, several research groups proposed that the rotation-induced lift force also contributes to the equilibration (Zhou and Papautsky 2013), aside from the wall-induced lift and the shear gradient lift which are two well-accepted lift forces (Amini et al. 2014; Di Carlo 2009).

In this chapter, we present a systematic work to analyze the lateral migration of monodisperse neutrally buoyant particles in a square channel. Both the *in situ* visualization method and the projection method are used. A wide range of  $Re$  from 0.07 to 280, suspensions with different particle volume fraction (0.1%, 0.2%, 0.4%), the ratio of particle size to channel hydraulic diameter  $d_p/H$  (0.11, 0.06), and the distance from channel inlet  $z/H$  (from 375 to 7,125) have been separately investigated to expand the understanding of the effects of flow conditions on the particle inertial migration. Finally, a preliminary test has been carried out on the biological particles, to study how micro-organisms migrate in the square channel and whether the developed experimental setup is suitable for studying practical suspensions.

### 3.1 Particle migration at moderate inertia

This part is dedicated to the investigation of particle migration at a moderate  $Re$  conditions ( $Re > 10$ ). First, the migration behavior is investigated with respect to the channel entry length ( $z/H$ ), the Reynolds number ( $Re$ ) and the particle to channel size ratio ( $d_p/H$ ) to reveal the influence of these parameters. Then, two important factors for the design of microfluidic devices devoted to particle separation, are separately discussed, that is, the equilibrium position localization and the outermost edge of particle distribution, i.e., the distance from the channel centerline to the farthest edge of the particle cluster. Finally the focusing degree is also discussed.

#### 3.1.1 Influence of the distance from channel inlet $z/H$

The study of the particle distribution at different longitudinal positions  $z/H$  can help to understand how the particle migration takes place and further develops. Here 8.7- $\mu\text{m}$  particles with a volume fraction  $\Phi = 0.1 \%$  at a constant Reynolds number  $Re = 11.2$  are studied at different vertical positions ( $y/H = 0.5, 0.375, 0.25$  and  $0.125$ ) and at longitudinal positions  $z/H$  ranging from 375 to 3,375. The particle spatial distributions (PDFs) is shown in Fig. 3-1.

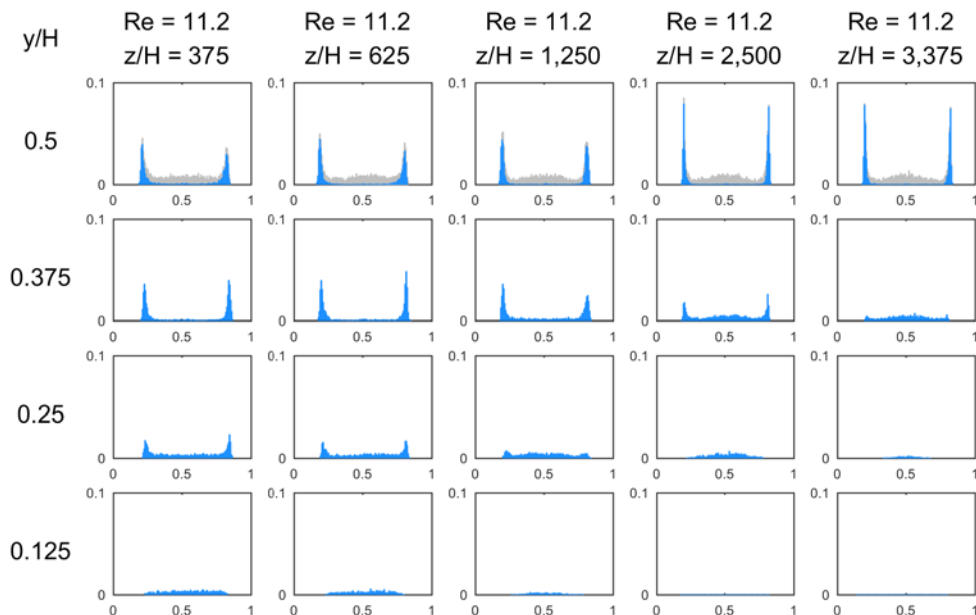


Fig. 3-1 Spatial distributions (PDFs) of 8.7- $\mu\text{m}$  test particles over normalized lateral positions at fixed  $Re = 11.2$  for various measurement positions  $z/H$ .

At  $z/H = 375$  and  $625$ , we can see two peaks near the channel walls at the channel midplane ( $y/H = 0.5$ ) and a relatively uniform distribution of particles near the channel bottom ( $y/H = 0.125$  and  $0.25$ ), indicating that the particles have laterally migrated towards the channel walls and a square annulus is formed close to the channel perimeter. This migration is called the lateral migration. This distribution means that the lateral migration is fully developed at  $z/H = 625$ . As  $z/H$  increases, particles near the channel bottom drift away from the corners and consequently accumulate near the center of the channel wall, which is termed the cross-lateral migration. The increase in peak intensities at  $y/H = 0.5$  and the deterioration of the peaks at  $y/H = 0.375$  also suggests the initiation of the cross-lateral migration. However, the cross-lateral migration is far from fully developed even at  $z/H = 3,375$ , which is due to the fact that  $Re$  is too small (as discussed in detail in the next subsection). The migration process can be more evidently observed at a higher  $Re$ .

Fig. 3-2 shows PDFs of the same suspension studied with  $Re = 28$  at different  $z/H$  positions. It is important to note that the observation is performed only at the channel midplane so the distribution of particles at other vertical positions can only be indirectly represented by the subtraction of the blue histogram from the gray one (all particles in the midplane). At  $z/H = 250$ , the uniform distribution of the gray histogram indicates the formation of an annulus and the fully developed lateral migration. Both intensity and sharpness of the gray peak increase with the increasing channel length, indicating that the particles migrate towards the centers of the four channel faces and the cross-lateral migration is in progress. This example clearly evidences the two-stage migration process involving the lateral migration and the cross-lateral one. However, the particles are not yet focused to a unique streamline located at the center of the channel wall, suggesting that the cross-lateral migration is not yet fully developed.

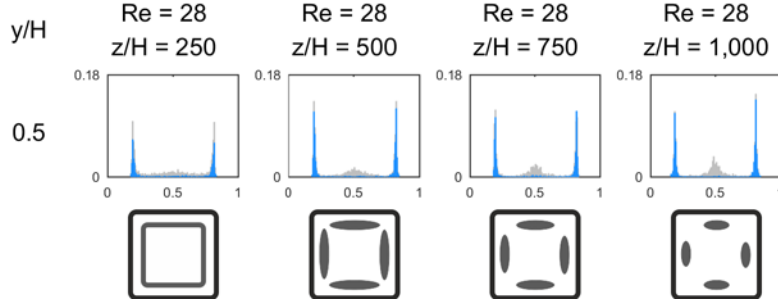


Fig. 3-2 Spatial distributions (PDFs) of 8.7- $\mu\text{m}$  test particles over normalized lateral positions at fixed  $Re = 28$  for various measurement positions  $z/H$ . Schematics of the particle distributions in the cross section are also sketched at the bottom of the figures.

Nevertheless, the channel length is considered enhancing the cross-lateral migration. This is more obvious at a higher  $Re$ , as shown in Fig. 3-3. For the same fluid at  $Re = 56$ , the cross-lateral migration already takes place at  $z/H = 250$ , develops with increasing channel length, and finally is complete at  $z/H = 1,000$ .

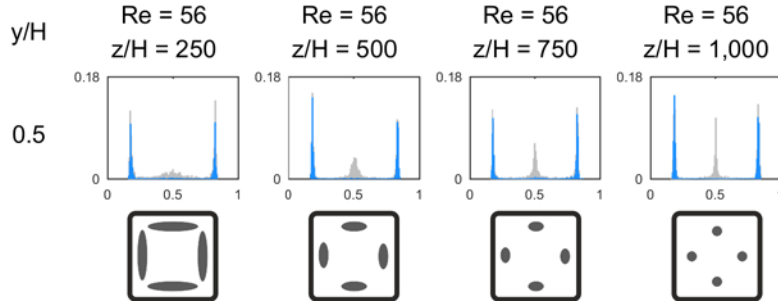


Fig. 3-3 Spatial distributions (PDFs) of 8.7- $\mu\text{m}$  test particles over normalized lateral positions at fixed  $Re = 56$  for various measurement positions  $z/H$ . Schematics of the particle distributions in the cross section are also sketched at the bottom of the figures.

We can therefore conclude that at moderate  $Re$ , the particle migration trajectories in a square channel undergo a two-stage migration regime: the particles migrate first in the lateral direction to form an annulus parallel to the channel walls and then cross-laterally towards the four equilibrium positions near the center of each channel face. This conclusion is consistent with previous findings (Abbas et al. 2014; Choi et al. 2011; Chun and Ladd 2006; Zhou and Papautsky 2013). The second stage, i.e., the cross-lateral migration, takes place only after that the lateral one is fully developed. The channel entry length  $z/H$  enhances the development of

the cross-lateral migration at moderate  $Re$ , but this enhancement depends also on  $Re$ , which is also in agreement with what has been reported by Choi et al. (2011). Moreover, the first stage lateral migration can occur very close to the channel inlet while it seems that a long channel is needed to complete the second stage cross-lateral migration, which indicates that the first stage of the migration process is rather rapid whereas the second one rather slow. This is consistent with the results numerically obtained by Abbas et al. (2014) (Fig. 3-4). The particle trajectories in this two-stage migration are shown in the plane perpendicular to the flow direction. In the first stage, the particles pass through the velocity iso-contours and reach an equilibrium ring; in the second one, they move along the equilibrium ring to the center of the channel face.

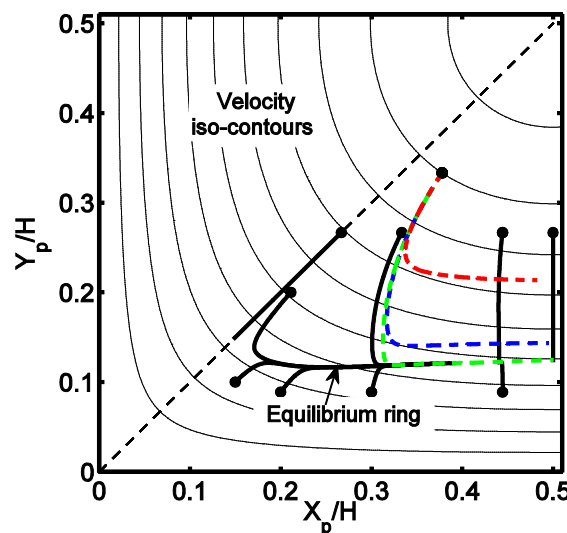


Fig. 3-4 Simulated trajectories of individual particles for a quarter of the channel cross section. The thick black lines are the particle trajectories for  $Re = 120$ ; the red, blue and green dashed lines are the trajectories from the same initial position for  $Re = 12, 60$  and  $120$ , respectively. (Abbas et al. 2014)

### 3.1.2 Influence of Reynolds number $Re$

8.7- $\mu\text{m}$  test particles (particle to channel size ratio  $d_p/H = 0.11$ ) with a volume fraction  $\Phi = 0.1\%$  over a finite range of  $Re$  from 14 to 210 are studied at different vertical positions ( $y/H = 0.5, 0.375, 0.25$  and  $0.125$ ) and at a fixed longitudinal position  $z/H = 1,000$ . Fig. 3-5 shows the spatial distributions of particles (PDFs) of this test.

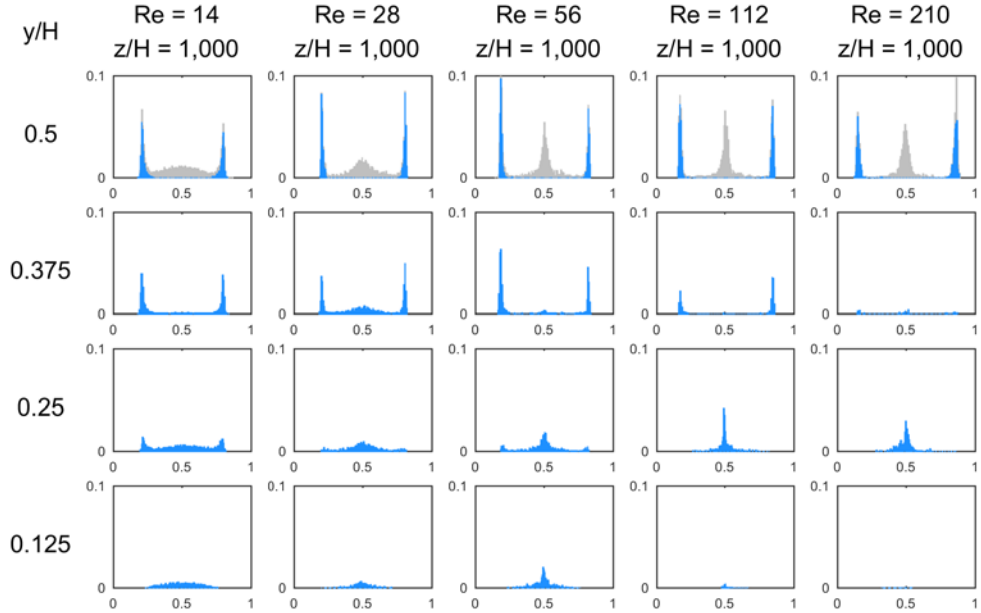


Fig. 3-5 Spatial distributions (PDFs) of 8.7- $\mu\text{m}$  test particles over normalized lateral positions at finite inertia for various  $Re$  at a fixed entry length  $z/H = 1,000$ .

For  $Re = 14$ , the two peaks observed at  $y/H = 0.5$  and the uniform distribution of particles at  $y/H = 0.125$  indicate that the particles have migrated towards the channel walls and form a square annulus. In other words, the lateral migration is fully developed at  $Re = 14$  and  $z/H = 1,000$ . As  $Re$  increases to 28, the particles begin to accumulate near the center of the channel wall and the cross-lateral migration initiates. At higher Reynolds number ( $Re = 112$  and 210), few particles are observed at  $y/H = 0.125$  and a central peak is visible at  $y/H = 0.25$ , which means that the particles are now focused at the four symmetric equilibrium positions near the centers of the channel faces. Besides, the three peaks being of similar intensities at  $y/H = 0.5$  and few particles being found at  $y/H = 0.375$ , the cross-lateral migration is considered to be fully developed. This focusing pattern, differing from the previous observations in cylindrical channels with a radial symmetry, shows a fourfold symmetry reducing the focusing positions to four attractors.

In short, at constant measurement position  $z/H$ , the particles at lower  $Re$  are more likely to laterally migrate to the channel walls and those with higher  $Re$  cross-laterally migrate to the centers of the channel faces. Although the detailed physical principles for the transition of the particle focusing mode from the lateral to the cross-lateral migration are not clear at this moment,

it is considered that high shear rate due to high  $Re$  in microchannel flows possibly induces important rotation-induced lift force driving particles towards the wall centers (Zhou and Papautsky 2013). Future investigations on the inertial migration in a micro-scale channel flow must consider these two different focusing regimes.

### 3.1.3 Influence of particle to channel size ratio

Smaller 5.3- $\mu\text{m}$  test particles, with the same number of particles in a given volume as the previous 8.7- $\mu\text{m}$  particle suspensions, hence, with a volume fraction  $\Phi = 0.02 \%$ , are investigated to reveal the influence of the particle to channel size ratio on inertial migration. Fig. 3-6 shows the PDFs of the 5.3- $\mu\text{m}$  particles at a constant measurement position  $z/H = 1,000$  for  $Re$  ranging from 5.6 to 1,000.

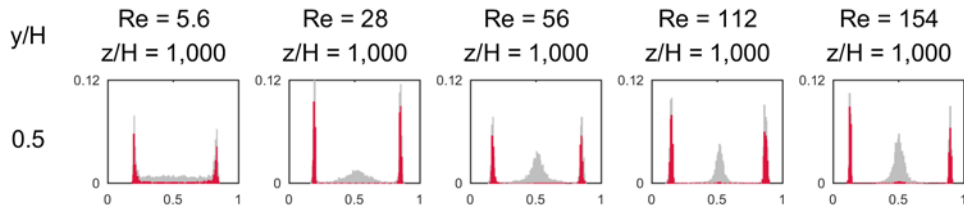


Fig. 3-6 Spatial distributions (PDFs) of 5.3- $\mu\text{m}$  test particles over normalized lateral positions for various  $Re$  at a fixed entry length  $z/H = 1,000$ .

The evolution of focusing as a function of  $Re$  is similar to that observed for the 8.7- $\mu\text{m}$  particles (Fig. 3-5). However, by comparing the gray peak intensity and sharpness, it is observed that the cross-lateral focusing is less developed for the small particles. We can then conclude that a higher particle to channel size ratio accelerates the migration.

The projection method is used to verify the particle spatial distributions deduced from the PDFs. Fig. 3-7 show the particle distributions of 8.7- $\mu\text{m}$  (red) and 4.8- $\mu\text{m}$  (green) fluorescent particles in the cross section at the channel length of 30 cm (corresponding to  $z/H = 3,750$ ), at  $Re = 8.3$  and 16.6, respectively.

The 8.7- $\mu\text{m}$  particles are focused at the center of the four channel faces at  $Re = 8.3$ , with a number of particles uniformly distributed as a loose annulus, indicating that the cross-lateral

migration has not yet been fully developed. At  $Re = 16.6$ , the particles are more focused at these four equilibrium positions, confirming that higher  $Re$  enhances the cross-lateral migration. The focusing positions were confirmed to be in the channel face centers but not the channel corners, by comparing the relative orientation of the membrane with respect to the channel cross section. The blurring of the focusing spots is due to a slight movement of the membrane during this sensitive experiment.

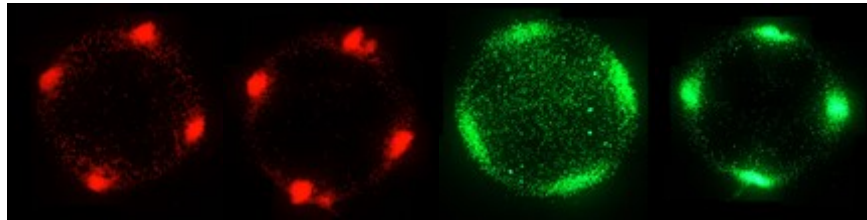


Fig. 3-7 Cross-sectional distributions of 8.7- $\mu\text{m}$  (red) and 4.8- $\mu\text{m}$  (green) test particles on a membrane at  $Re = 8.3$  and  $16.6$ , respectively.

The migration behaviors of the 4.8- $\mu\text{m}$  particles are similar to the 8.7- $\mu\text{m}$  ones, but the focusing degree is weaker under the same experimental conditions ( $\Phi$ ,  $Re$  and  $z/H$ ). At  $Re = 8.3$ , the focusing at the channel walls is prevalent and the cross-lateral migration towards the centers of the channel faces is far from complete at this measurement position  $z/H = 3,750$ . At  $Re = 16.6$ , the cross-lateral migration is considered to be nearly finished at the same channel length.

### 3.1.4 Equilibrium positions localization

It is of great importance, for the design of microdevices regarding particle concentration and separation, to know the exact locations of the equilibrium positions in the square cross section. The aim of this section is to study the evolution of these locations with the Reynolds number.

To this end, we first define a non-dimensional term  $X_{eq}$ , as the distance between the equilibrium position and its closest wall normalized by the channel width  $W$  ( $X_{eq}$  equal to 0 or 0.5 indicates that the particle equilibrium position is located at the channel face or centerline, respectively). It is determined from the distance of the peaks in the PDF histogram at the midplane ( $y/H = 0.5$ ) to the channel face.  $X_{eq}$  at each side of the histogram are separately measured and then averaged

in order to be more accurate. The possible errors in determining  $X_{eq}$  mainly consist of two patterns: (a) the error in determining channel edges  $\delta_w$  corresponding to one pixel size in the image ( $0.63 \mu\text{m}$ ) and (b) the error due to the identification of the particle centers by the program in Matlab  $\delta_p$  which is less than 20 % of the particle size and so estimated to be  $1.10 \mu\text{m}$ . Accordingly, the total error  $\Delta = \delta_w + \delta_p = 1.73 \mu\text{m}$  and the relative error with respect to the channel size  $\Delta/H \times 100\%$  is 2.16 %.

Fig. 3-8 displays the evolution of  $X_{eq}$  with respect to  $Re$ , in comparison with the experimental studies carried out by other authors. Blue squares and red triangles are experimental results from the present work. Green triangles and yellow diamonds are from Choi et al. (2011) for  $d_p/H = 0.075$  and 0.16, respectively. Hollow black triangles are from Kim and Yoo (2008) for  $d_p/H = 0.071$ .

Our results are in agreement with the other curves. In all cases,  $X_{eq}$  decreases with decreasing particle size (here  $d_p/H$  from 0.16 to 0.066), and with increasing  $Re$  (in the range of 10 to 280). The value of  $X_{eq}$  found in our study is between 0.1 and 0.2, consistent with the numerical simulation value of  $X_{eq} \sim 0.2$  for particles with  $d_p/H = 0.1$  for  $Re > 100$  in a square channel reported by Chun (Chun and Ladd 2006), and the experimentally obtained  $X_{eq}$  of 0.18 for blood cells in a  $50 \mu\text{m} \times 50 \mu\text{m}$  channel ( $d_p/H \sim 0.14$  at  $Re = 60$ ) reported by Di Carlo et al. (2007). Besides, these tendencies of  $X_{eq}$  evolution with respect to  $Re$  and particle size is also in agreement with the theoretical predictions in planar channel flows (Asmolov 1999) and the experimental results in rectangular microchannel flows (Mach and Di Carlo 2010).

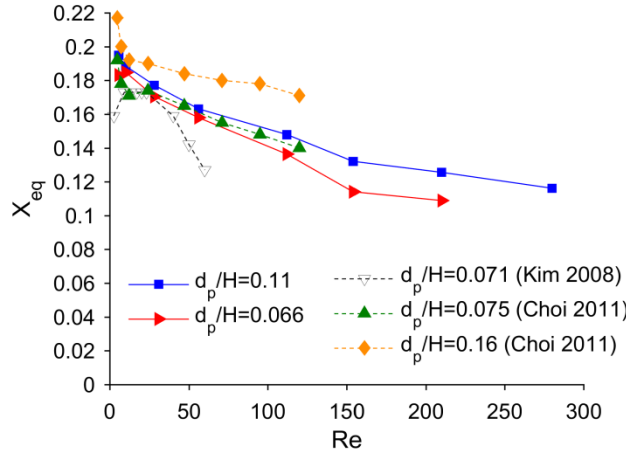


Fig. 3-8 Particle equilibrium position  $X_{eq}$  as a function of  $Re$ .

### 3.1.5 Outermost edge of particle distributions

It has been noticed that a particle-free region is present very close to the channel faces under all the flow conditions, which is evidenced both in the microscopic images and on the PDFs. This can be explained by the significant wall repulsion force exerted between the particles and the wall (Feng et al. 1994b). This is also an important parameter in the design of microfluidic devices for particle separation or sorting. For example, in order to separate plasma from the blood, the main technique is to extract the plasma through the particle-free region (Yang et al. 2006). The best performance is expected to be achieved by enlarging the particle-free layer.

The outermost edge of particle distribution  $X_{out}$ , was first proposed by Segre and Silberberg (1962b) and can be defined as the distance from the channel centerline to the farthest edge of the particle cluster normalized by the channel dimension.  $X_{out}$  is determined on the PDF in the following way; the lateral distances from the centerline to the two outermost edges of the histogram are separately measured and averaged to be more accurate. The experimental errors in determining  $X_{out}$  are the same as for  $X_{eq}$ .

Fig. 3-9 shows the evolution of  $X_{out}$  obtained in the present study as a function of  $Re$ , in comparison with the results of Segre and Silberberg (1962b). We find that  $X_{out}$  increases as  $Re$  increases and decreases as the particle to channel size ratio  $d_p/H$  increases. Our results for  $d_p/H = 0.11$  collapses well with that of Segre and Silberberg (1962b) for  $d_p/H = 0.108$  in a cylindrical

channel. Kim and Yoo (2008) reported a  $X_{out} = 0.35$  for  $Re < 58$  with  $d_p/H = 0.069$ , also very close to our data for  $d_p/H = 0.066$  at the same  $Re$ .

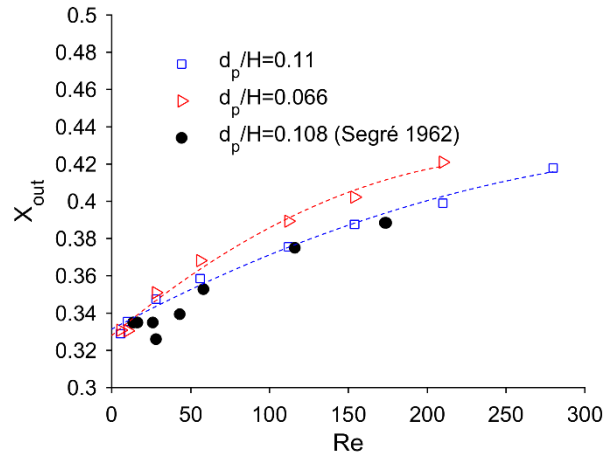


Fig. 3-9 Particle outermost edge  $X_{out}$  as a function of  $Re$  for different  $d_p/H$ .

### 3.1.6 Focusing degree

The inertial focusing is frequently used to separate particles from a mixture as seen in Chapter 1. The efficiency of these separation devices depends on the efficiency of the inertial focusing. It seems thus relevant to introduce a parameter that quantifies the “degree of focusing” of a suspension. This is the goal of this section. The results shown here, however, are only preliminary ones that need to be confirmed by further investigations.

The “focusing degree” that we introduced is defined as the percentage of particles focused at the four equilibrium positions in comparison with the total number of particles in the microchannel. To evaluate this percentage:

- only PDFs at the midplane of the channel are considered;
- the exact positions of the 3 peaks visible on the PDFs (corresponding to the particles located near the vertical walls and near the center of the horizontal ones) is found as defined in Chapter 2;
- a lateral bandwidth of  $0.4 d_p$  is chosen, i.e., only particles centered at a distance less than  $0.2 d_p$  from the equilibrium position on x-axis are considered to be located on the equilibrium

position.

- the number of particles located inside the bands around each peak is evaluated. In fact, we identify with this method the number of particles located in the rectangular zone of  $0.4 d_p$  in width and  $10 \mu\text{m}$  in depth around the four equilibrium positions. The degree of focusing as defined here, is thus dependent on the chosen band width and on the axial resolution.
- these numbers are summed and divided by the total number of particles identified in the PDFs.

Fig. 3-10 shows the degree of focusing of  $8.7\text{-}\mu\text{m}$  particles flowing at  $Re = 11.2, 28$  and  $56$  at  $z/H$  ranging from  $375$  to  $3,375$ , corresponding to the PDFs in Fig. 3-1. The focusing degree increases with increasing measurement position for the three studied Reynolds numbers. Indeed, it increases more acutely at small distances from channel inlet corresponding to the first stage of migration where particles migrate rapidly toward an annulus. And it increases less acutely further, confirming that the second stage of migration, i.e., the cross-lateral migration is a slow phenomenon. No stabilization of the curves has been observed since the migration is fully-developed for none of the presented cases. Besides, the focusing degrees are higher for higher Reynolds numbers due to the fact that at a given distance from channel inlet, the higher the Reynolds number is, the more developed is the inertial focusing.

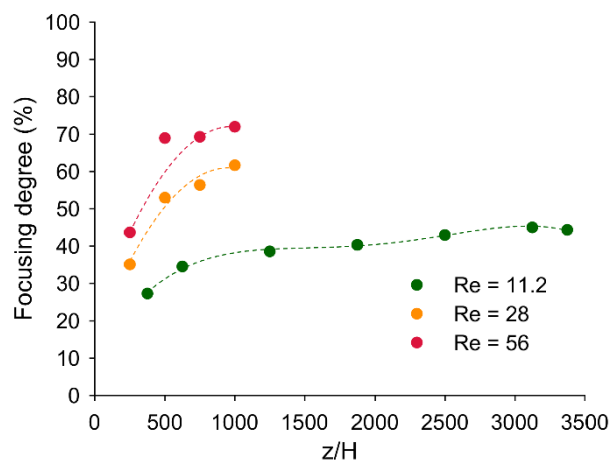


Fig. 3-10 Focusing degree as a function of channel length  $z/H$  for  $8.7\text{-}\mu\text{m}$  particles at  $Re = 11.2$ .

In Fig. 3-11, the focusing degree is plotted for different Reynolds numbers (corresponding to the PDFs presented in Fig. 3-5) at a given distance from channel inlet.

This curve reveals two different kinds of information:

For Reynolds number less than 150, the total migration is not complete at a distance  $z/H = 1,000$  from channel inlet. The focusing degree thus quantifies the degree of development of the inertial migration. As seen in the Figure, the focusing degree increases with increasing  $Re$ , when  $Re < 150$ , confirming that at a given distance from channel inlet, the higher the Reynolds number is, the more developed is the inertial focusing. The maximum is reached at  $Re = 154$  where the migration begins to be fully-developed.

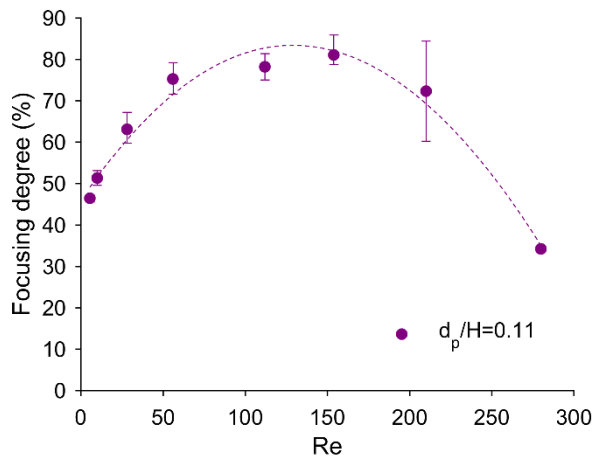


Fig. 3-11 Degree of migration at fixed channel length  $z/H = 1,000$  with respect to  $Re$ .

For Reynolds numbers larger than 154, the total migration is fully-developed at a distance  $z/H = 1,000$  from channel inlet. The focusing degree thus quantifies the maximum inertial focusing i.e. the maximum percentage of particles in the four equilibrium positions that can be reached at a given Reynolds number. As seen in Fig. 3-11, the focusing degree decreases with increasing  $Re$  when  $Re > 150$ . The point at  $Re = 280$  has not been repeated due to clogging problems and was difficult to post-process due to the small contrast in the images (an exposure time of 2  $\mu$ s was used to freeze the particles).

Fig. 3-12 displays the overall and in-focus particle distributions at channel midplane and at  $Re$

= 112, 210 and 280.

It can be seen that in the midplane at  $Re = 280$ , in-focus particles are only observed near the walls, whereas out-of-focus particles are observed in the whole channel width. This suggests that at  $Re = 280$  particles are focused in an annulus close to the perimeter of the channel.

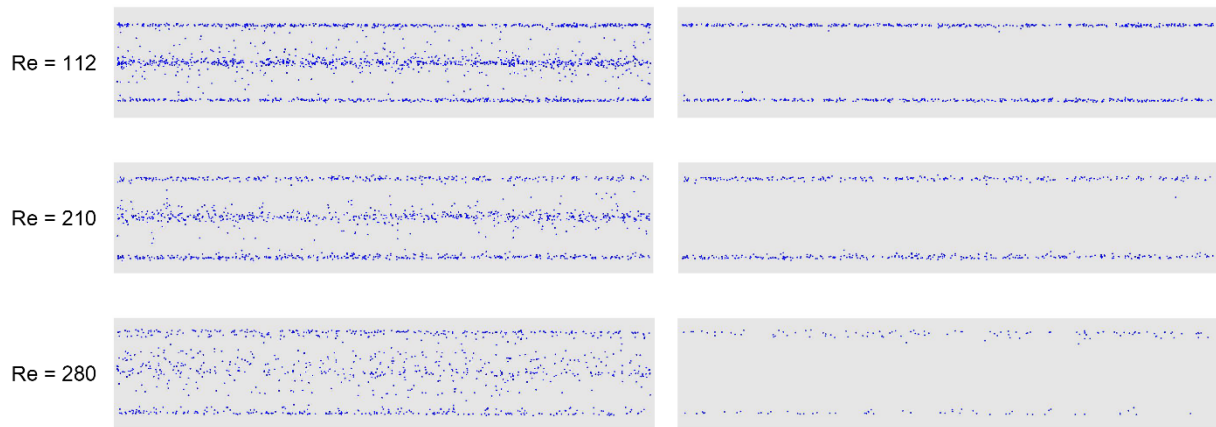


Fig. 3-12 Overall particle distributions (left) and in-focus particle distributions (right) at channel midplane at  $Re = 112, 210$  and  $280$ .

Nakagawa et al. (2015), also observed a shift in the migration behavior of particles flowing in square channels with a particle diameter to channel size ratio  $d_p/H = 0.1$ .

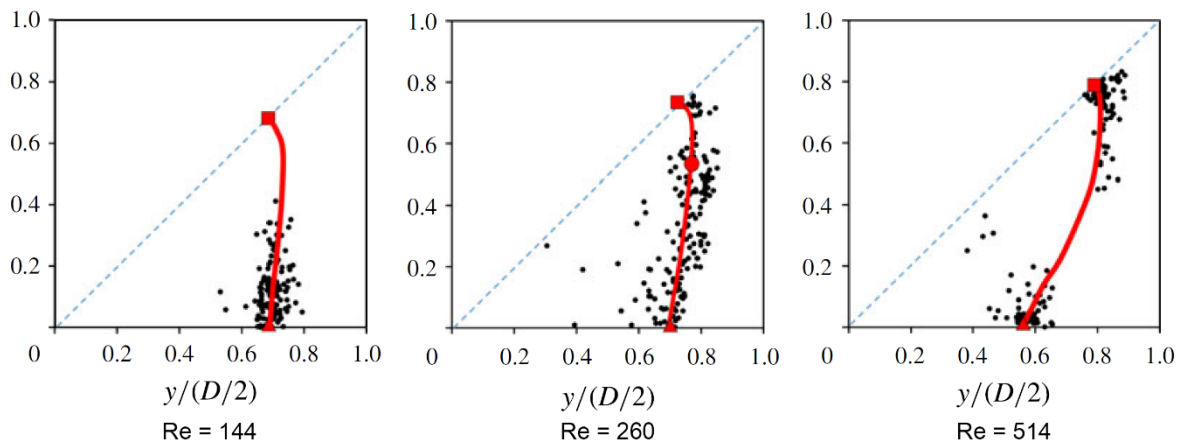


Fig. 3-13 Particle distributions obtained experimentally at  $Re = 144$  (left side),  $Re = 260$  (middle) and  $Re = 514$  (right side). (Reprinted from Nakagawa et al. (2015).)

At  $Re = 144$ , the equilibrium positions are found only at the center of the channel faces, at  $Re = 76$

$= 260$ , other stable equilibrium positions are found near the channel corners (shown as the red circle on the red line) and at  $Re = 514$  both the channel face and the channel corner equilibrium positions are present. The results we obtained at  $Re = 280$  are consistent with Nakagawa's ones. It would have been interesting to go further into this shift in the migration behavior at higher Reynolds numbers, but this was not possible within the allotted time.

### 3.2 Particle migration at low inertia

In spite of the huge number of works dealing with lateral migration of particles in square or rectangular microchannels, the characterization of the particle migration process through a microchannel at extremely low inertia has rarely been reported. Indeed, this is a very slow phenomenon that consequently requires a great channel length, while the channels reported in the literature are always limited up to 10 cm.

In this section, a systematic study of particle migration at low inertia (corresponding to  $Re$  from 0.07 to 7) has been carried out using the  $80 \mu\text{m} \times 80 \mu\text{m}$  square microchannel with a length of 60 cm ( $z/H$  up to 7,125), to reveal the particle distribution as a function of Reynolds number  $Re$ , distance from channel inlet  $z/H$ , particle volume fraction  $\Phi$  and particle to channel size ratio  $d_p/H$ .

#### 3.2.1 Influence of Reynolds number $Re$

Fig. 3-14 illustrates the spatial distributions (PDFs) of 8.7- $\mu\text{m}$  test particles ( $d_p/H = 0.11$ ) at a volume fraction  $\Phi = 0.1 \%$  over the range of  $Re$  from 0.07 to 7 studied at different vertical positions ( $y/H = 0.5, 0.375, 0.25, 0.125$ ) and at a fixed longitudinal position  $z/H = 7,125$ .

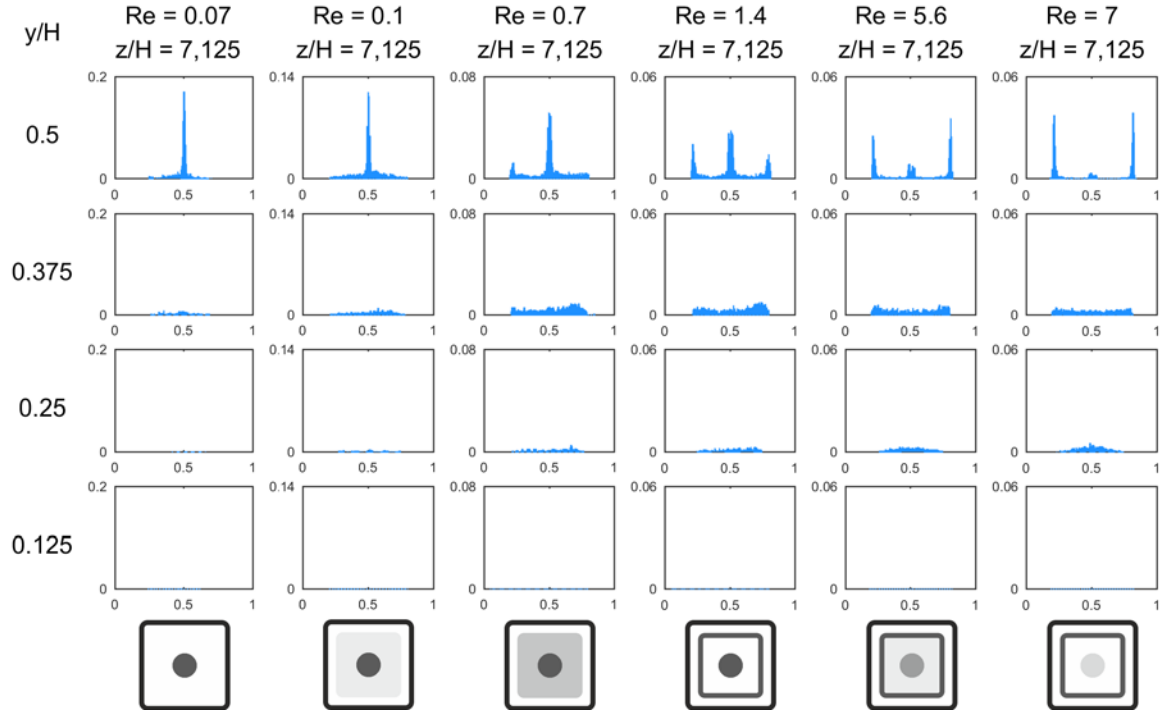


Fig. 3-14 Spatial distributions (PDFs) of 8.7- $\mu\text{m}$  test particles over normalized lateral positions at low and finite inertia at a fixed entry length  $z/H = 7,125$  for various  $Re$ . Schematics of the particle distributions in the cross section are also sketched at the bottom of the figures.

At extremely low flow inertia ( $Re = 0.07, 0.1$  and  $0.7$ ), a strong peak is observed at the channel width center at the midplane ( $y/H = 0.5$ ) and few particles are distributed elsewhere, clearly indicating that the particles are preferentially focused towards the channel centerline. This is another migration regime that hasn't been observed yet and that takes place at low  $Re$ . But at  $Re = 0.1$  and  $0.7$ , the central peak at  $y/H = 0.5$  decreases and a few particles are found to migrate towards the channel faces. For  $Re = 1.4$  and  $5.6$ , high levels of particle concentration are observed simultaneously at the channel centerline and near the channel faces. The migration regime towards the channel centerline and that towards the channel faces coexist in these conditions. But the dominant focusing position is at the channel centerline for  $Re = 1.4$  and at the channel faces for  $Re = 5.6$ . Finally at  $Re = 7$ , the lack of particles at the channel centerline suggests that the migration process towards the center vanishes for the benefit of the migration towards the wall.

As a conclusion, a second regime of migration appears at low Reynolds number where particles concentrate at the centerline of the channel. At a given distance from channel inlet, the equilibrium position gradually shifts from the centerline to the faces as  $Re$  increases. This migration is a slow phenomenon.

The physical explanation of the migration towards the channel centerline is not obvious. At moderate flow inertia, Di Carlo (2009) and Matas et al. (2004c) suggest that the equilibrium position existence is due to the competition of two opposite inertial forces: the “shear-induced lift force” that pushes the particles away from the centerline towards the wall and the “wall-induced lift force” that pushes the spheres away from the wall. At low flow inertia with a blunted velocity profile, the “shear-induced lift force” is very small compared to the “wall-induced lift force”, and remains insignificant in the previously described competition. Nevertheless, the predominant wall induced lift force could probably not be the only reason of the migration towards the centerline. Other physical phenomena like interactions between the finite-size particles certainly become significant in this range of Reynolds numbers. Further experiments are needed to better understand the physical mechanism involved here.

### 3.2.2 Influence of channel length $z/H$

The particle migration at low  $Re$  is a slow process requiring a long distance for the particles to reach the final equilibrium position. So it is of great interest to investigate the establishment of the migration along the channel. In addition, at  $Re = 1.4$  and  $5.6$ , both migration regimes coexist but the dominant one is different. To better understand the shift between the two situations, the study of  $z/H$  has been carried out on these two  $Re$  conditions.

Fig. 3-15 presents the spatial distributions (PDFs) of  $8.7\text{-}\mu\text{m}$  test particles with  $\Phi = 0.1\%$  studied at different measurement positions  $z/H$  ranging from  $625$  to  $7,125$ , for  $Re = 1.4$ . Close to the channel entrance ( $z/H = 625$ ), particles remain uniformly distributed across the channel cross section indicating that nearly no migration is undergone. At a distance  $z/H = 1,250$  from the channel inlet, higher densities of particles are observed near the walls ( $y/H = 0.25$ ),

indicating that the lateral migration towards the channel walls first takes place and a loose square annulus is formed. As the channel entry length increases, at  $z/H = 2,500$ , both migrations towards the channel centerline and towards the faces are present, and the migration towards the channel centerline becomes predominant. The distribution profiles at  $z/H = 5,000$  and  $7,125$  are quite similar to that obtained at  $z/H = 2,500$ , except that the maximum value of the PDF at  $y/H = 0.5$  slightly increases, which indicates a higher degree of particle focusing around the centerline. We can thus conclude that both migration processes coexist and are gradually established along the channel length. The migration towards the centerline becomes dominant after  $z/H = 2,500$ .

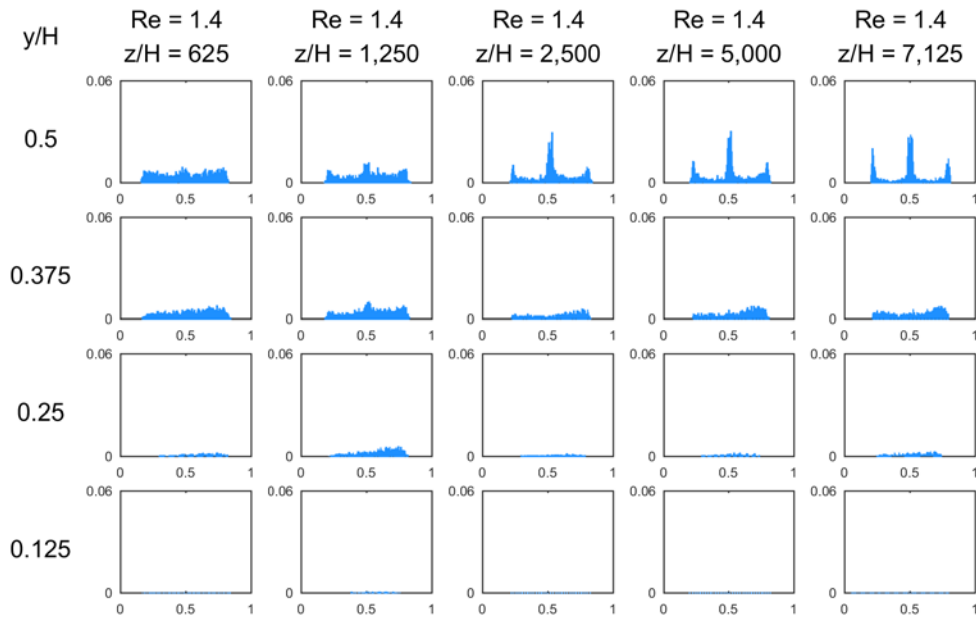


Fig. 3-15 Spatial distributions (PDFs) of 8.7- $\mu\text{m}$  test particles over normalized lateral positions at fixed  $Re = 1.4$  for various measurement position  $z/H$ .

Fig. 3-16 represents the spatial distributions (PDFs) of the same particle suspension studied at different measurement positions  $z/H$  ranging from 625 to 7,125, for  $Re = 5.6$ . Contrary to the case of  $Re = 1.4$ , the particles already begin to migrate towards the channel faces close to the channel entrance ( $z/H = 625$ ) and form a loose annulus, and a small amount of particles are concentrated around the channel centerline. At  $z/H = 1,250$ , the two peaks near the walls at  $y/H = 0.5$  are more intense, indicating an increase of the degree of particle focusing towards the

channel walls. As the channel length further increases, outside peaks become thinner but without evident change of intensity, while the central peak gradually increases, indicating that the migration to the channel walls is full developed while the migration towards the centerline is still in progress. This difference in the time scale associated with each migration regime can be explained by the small inward migration velocity of the particles due to the weak force acting towards the channel centerline near the center region. The dominant equilibrium positions are always the channel walls.

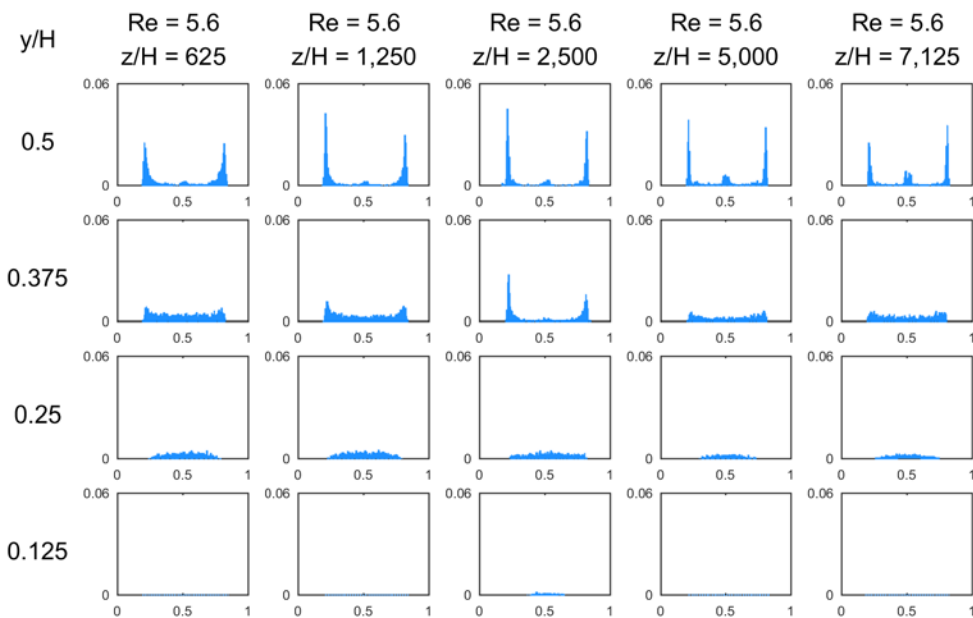


Fig. 3-16 Spatial distributions (PDFs) of 8.7- $\mu\text{m}$  test particles over normalized lateral positions at fixed  $Re = 5.6$  for various measurement position  $z/H$ .

According to the particle migration progress at both  $Re = 1.4$  and  $Re = 5.6$ , we can conclude that the migration towards the channel faces is a fast process and the migration towards the channel centerline needs a longer distance to be established. The final prevalence of one regime to the other depends both on the Reynolds number and on the channel length.

### 3.2.3 Influence of particle volume fraction

All the studies discussed above are based on a low particle concentration  $\Phi = 0.1 \%$ . In this part, we will investigate the influence of particle volume fraction on particle migration behavior

at low inertia. 8.7- $\mu\text{m}$  test particles with higher volume fractions of 0.2 % and 0.4 % over the range of Reynolds numbers  $Re$  from 0.07 to 7 are studied at different vertical positions  $y/H = 0.5, 0.375, 0.25$  and 0.125 and at a fixed longitudinal position  $z/H = 7,125$ .

Fig. 3-17 and Fig. 3-18 respectively show the particle spatial distributions (PDFs) for the suspension with  $\Phi = 0.2 \%$  and 0.4%.

Generally, by comparing these two figures to their counterpart in Fig. 3-14 ( $\Phi = 0.1 \%$ ), we can easily find that, first, the maximum PDF value at  $y/H = 0.5$  decreases with the increasing of volume fraction, indicating that the degree of particle focusing recedes; second, under all three conditions, both migrations towards the channel centerline and that towards the channel walls coexist, and there is a transition of the predominant equilibrium position as  $Re$  increases.

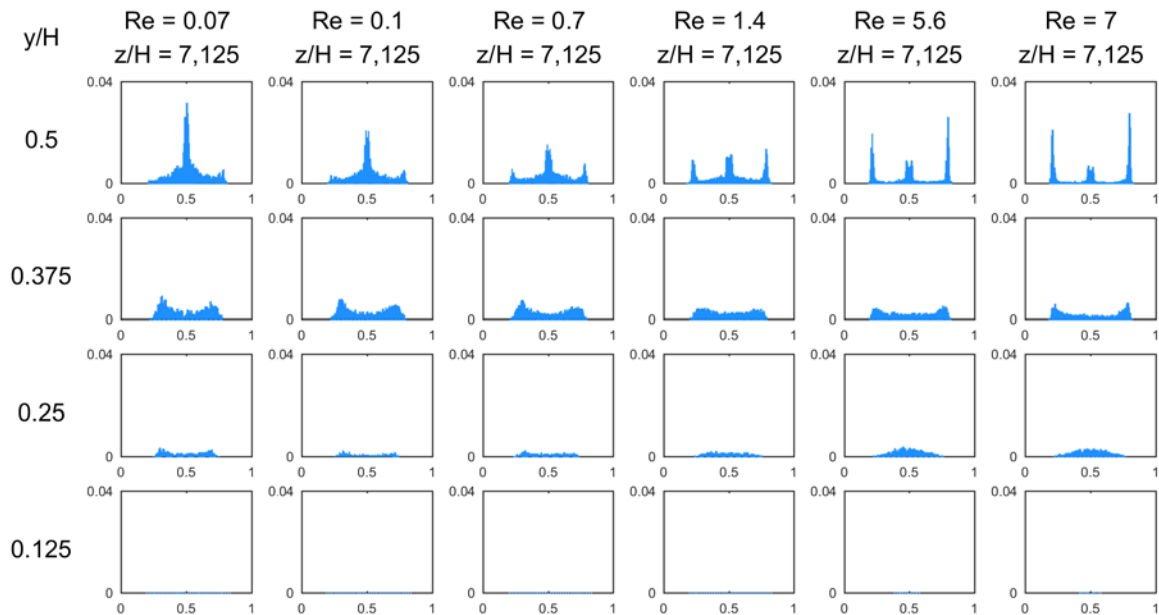


Fig. 3-17 Spatial distributions (PDFs) of 8.7- $\mu\text{m}$  test particles over normalized lateral positions at a fixed entry length  $z/H = 7,125$  for various  $Re$  at a concentration  $\Phi = 0.2 \%$ .

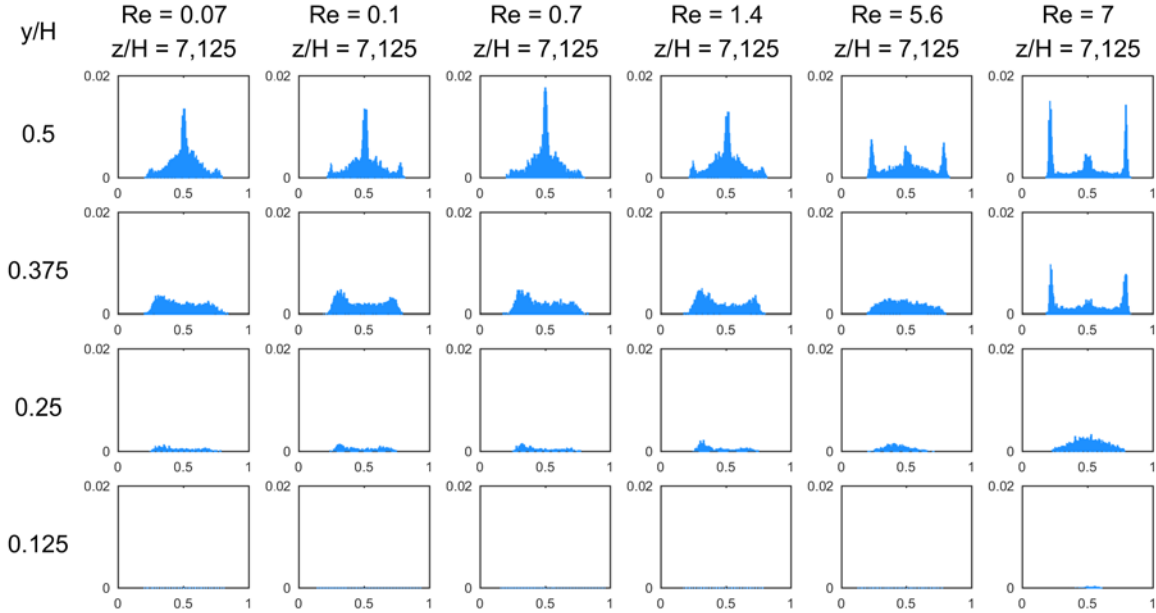


Fig. 3-18 Spatial distributions (PDFs) of 8.7- $\mu\text{m}$  test particles over normalized lateral positions at a fixed entry length  $z/H = 7,125$  for various  $Re$  at a high concentration  $\Phi = 0.4 \%$ .

Specifically, at extremely low  $Re$  from 0.07 to 0.7, the central peaks of the PDFs at the midplane  $y/H = 0.5$  show obviously larger widths at a higher volume fraction, indicating an augmentation of the particle distribution at the non-equilibrium position around the center region (aside from the channel centerline and each channel face center), which suggests a lack of capability to maintain all the particles at the channel centerline. At a relatively higher  $Re$  from 1.4 to 7, high volume fraction seems to be a factor enhancing the particle migration towards the channel centerline which is an unstable equilibrium position at low concentration: at  $Re = 1.4$ , the predominant focusing towards the channel centerline is most obvious for  $\Phi = 0.4 \%$ ; at  $Re = 5.6$ , the predominant focusing position becomes the channel walls but this prevalence is less obvious for  $\Phi = 0.4 \%$ . The transition thus occurs between  $Re = 1.4$  and  $Re = 5.6$  for low concentrations but tends to shift to a higher Reynolds number when the volume fraction increases. Finally, at  $Re = 7$ , there are still a number of particles focused at the channel centerline at  $\Phi = 0.4 \%$ , while nearly no particles are gathered there at  $\Phi = 0.1 \%$ .

This phenomenon is consistent with the observations of some previous works. For example, Han et al. (1999) reported that qualitatively different from the tubular pinch effect at a low

concentration, the particle distribution profile along the radial position has a double-humped shape (focusing at the center and at the Segré-Silberberg annulus) in a cylindrical channel at higher concentration. Lim et al. (2012) reported that the larger prostate cancer cells (PC-3) focusing in a rectangular channel shifted radically in whole blood and predominantly occupied an unstable equilibrium position (the short face centers of the channel) in diluted blood.

Furthermore, the particle aggregated clusters are observed at low  $Re$  and high concentration, in agreement with the report of Chun and Ladd (2006). Fig. 3-19 shows the microscopic images of the  $8.7\text{-}\mu\text{m}$  particles with  $\Phi = 0.4\%$  and  $Re = 0.07$ , taken at  $z/H = 7,125$  with the focal plane located at the channel midplane ( $y/H = 0.5$ ). Particle aggregation or particle clusters can be observed in the right picture, which may explain the wider peaks on the corresponding histogram. Complementary, we have checked that there are nearly not pre-aggregated particles near the channel entrance and have found that at volume fractions less than  $0.1\%$ , nearly none of these particle aggregations or clusters are formed. Aggregation occurs certainly as particles concentrate in the channel center.

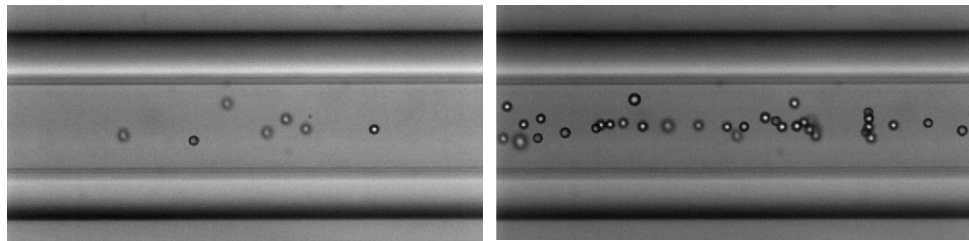


Fig. 3-19 Particle cluster formation at high concentration.

We also notice that the number of particles on each image is fluctuant as shown by the left and right images in Fig. 3-19. This heterogeneity is probably due to the interaction between the numerous particles at a high concentration conditions. Further experiments are needed to uncover the physical explanation of this phenomenon.

The volume fraction shows influence not only on the final equilibrium positions, but also on the migration progress along the channel length. Fig. 3-20 shows the spatial distributions (PDFs) of the  $8.7\text{-}\mu\text{m}$  test particles with  $\Phi = 0.4\%$  at constant Reynolds numbers  $Re = 1.4$  and  $5.6$

studied along the channel length from  $z/H = 1,250$  to 7,125.

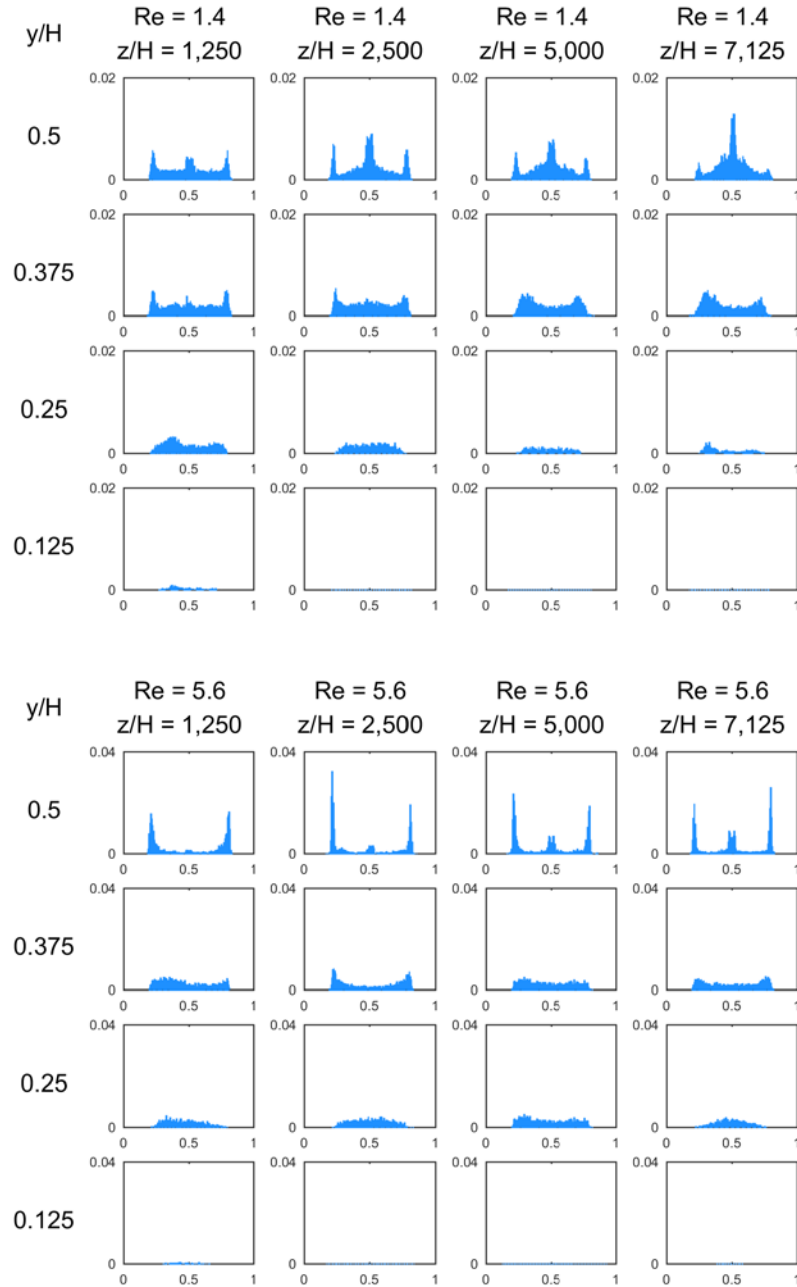


Fig. 3-20 Spatial distributions (PDFs) of 8.7- $\mu\text{m}$  test particles over normalized lateral positions at fixed  $Re = 1.4$  and 5.6 for various entry length  $z/H$  at a high concentration  $\Phi = 0.4 \%$ .

The global migration process along the channel length at  $\Phi = 0.4\%$  is similar to that in the low concentration condition shown in Fig. 3-15 and Fig. 3-16 and confirms that:

- first, the migration towards the channel centerline is a slow phenomenon and is gradually

developed as the channel length increases;

- second, the migration towards the channel walls is a rapid phenomenon (for example, a loose square annulus is already formed at  $z/H = 1,250$  at  $Re = 5.6$ );
- and third, the transition between both migration regimes seems thus to occur at higher  $Re$  when concentration increases. By comparing the histograms at  $z/H = 7,125$  for  $\Phi = 0.4\%$  and  $\Phi = 0.1\%$ , we can find indeed, at higher volume fraction, the predominance of the migration towards the channel centerline at  $Re = 1.4$  is more obvious, and that towards the channel walls at  $Re = 5.6$  is weakly marked.

In short, the particle migration as a function of  $Re$  and  $z/H$  at higher volume fraction follows the same rules as at low volume fraction, except that the migration towards the channel centerline is enhanced and that the transition between the two regimes is moved towards higher Reynolds numbers.

### 3.2.4 Influence of particle to channel size ratio

In order to investigate the effect of the particle size on the inertial focusing behavior, various particle diameters,  $d_p = 1.9, 5.3, 8.7$  and  $15.6 \mu\text{m}$ , have been studied in this work, corresponding to the ratios of particle diameter to the channel hydraulic diameter  $d_p/H = 0.025, 0.066, 0.11$  and  $0.19$ .

Here we show the measurements for  $d_p/H = 0.11$  and  $0.066$  ( $d_p = 8.7 \mu\text{m}$  and  $5.3 \mu\text{m}$ ) with a volume fraction  $\Phi = 0.2\%$  carried out at a fixed measurement position  $z/H = 7,125$  with  $Re$  ranging from  $0.07$  to  $7$ . The particle spatial distributions (PDFs) are presented in Fig. 3-17 and Fig. 3-22, respectively.

Comparing the PDFs of these 2 types of particles under the same experimental conditions ( $Re$  and  $z/H$ ), it can be seen that the maximum values of the PDFs decrease with the decreasing particle diameters, indicating a decline of focusing degree. Moreover, the particle migration towards the channel centerline is more significant for large particles. Two migration regimes

are observed for 8.7- $\mu\text{m}$  particles in the studied range of Reynolds numbers: the migration towards the channel centerline at  $Re = 0.07$  and the coexistence of the migration towards the channel centerline and that towards the channel walls at higher  $Re$ . The predominant equilibrium position is shifted from the centerline to the walls between  $Re = 1.4$  and  $Re = 5.6$ . For the 5.3- $\mu\text{m}$  particles, the migration towards the centerline is extremely weak at  $Re = 0.07$  and  $z/H = 7,125$ , indicating that the migration towards the channel centerline is slower for small particles and the channel length ( $z/H = 7,125$ ) is not sufficient for them to reach the equilibrium positions at the channel centerline. Besides, the predominant equilibrium position is always at the walls, probably suggesting that the transition between the two regimes occurs at a smaller  $Re$  when the particle to channel size ratio decreases.

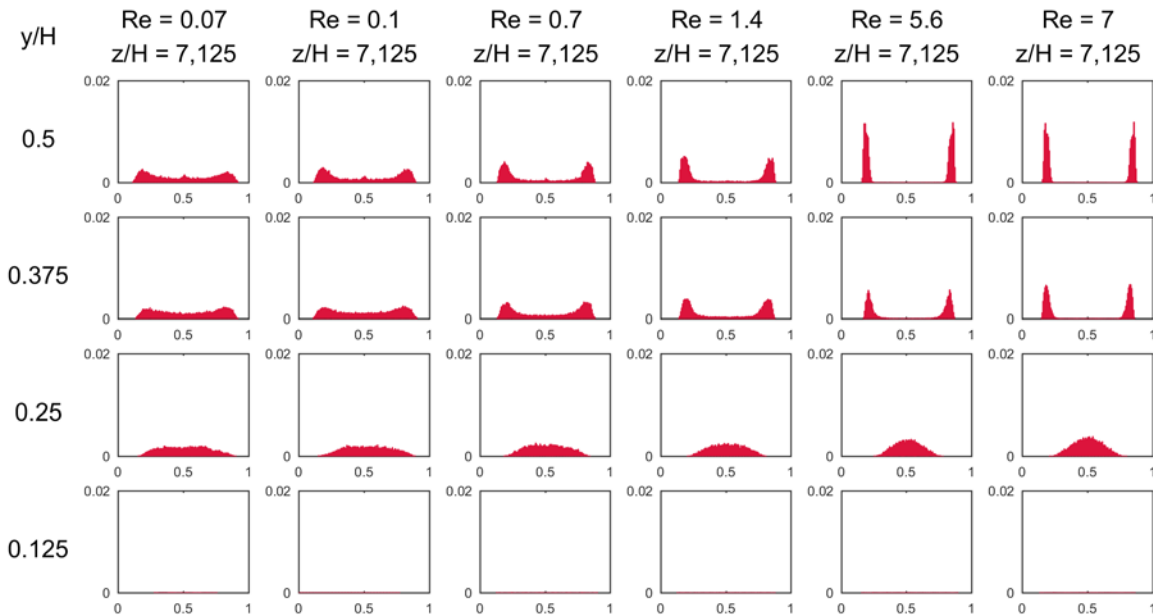


Fig. 3-21 Spatial distributions (PDFs) of 5.3- $\mu\text{m}$  test particles over normalized lateral positions at a fixed entry length  $z/H = 7,125$  for various  $Re$ .

It has to be noted that for the 5.3- $\mu\text{m}$  particles, the volume fraction = 0.2 % indeed leads to a huge number of particles in a given volume, as compared to the the 8.3- $\mu\text{m}$  particles. At lower  $Re$ , these particles tend to be aggregated. If we take into account the aggregation of small particles and treated them as a large particle with the same centroid in the postprocessing program, we may find a central peak appearing on the PDFs at  $y/H = 0.5$ , as shown in Fig. 3-22,

indicating that the aggregations migrate towards the centerline of the channel, just as the large particles.

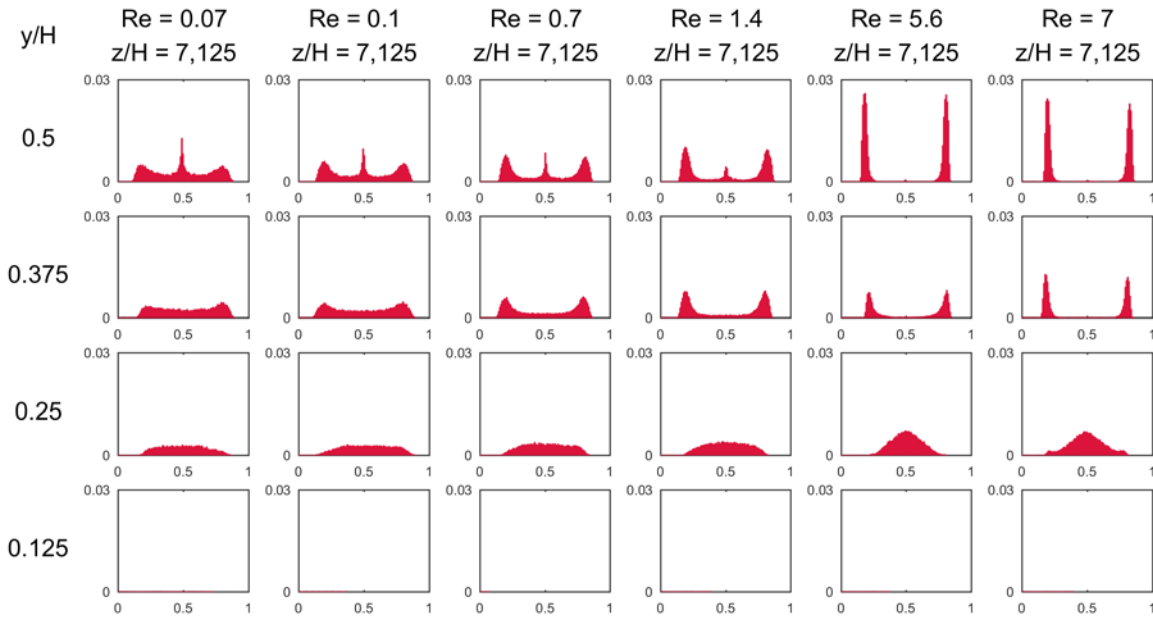


Fig. 3-22 Spatial distributions (PDFs) of  $5.3\text{-}\mu\text{m}$  test particles over normalized lateral positions at a fixed entry length  $z/H = 7,125$  for various  $Re$ . (Aggregations are taken into account)

Generally speaking, the focusing effect becomes significant as the ratio of particle to channel size increases, indicating its dependence on this parameter. The critical  $Re$ , where the lateral migration attains a fully developed state (4 equilibrium positions at each channel face), appears to be smaller in the case of large particles. This can be explained by the fact that the inertial lift force is proportional to the particle diameter at the power 4, while the Stokes drag force is proportional to the first power of the diameter. Hence, the force balance between these two forces brings about higher lateral migrating velocity for large particles, which induces faster lateral motion, even though the maximum flow velocity is small (Di Carlo 2009). Similarly, the particle migration towards the channel centerline is more significant for large particles. However, this migration needs a longer channel and a smaller  $Re$  value. This implies that the migration towards the channel face centers occurs more easily as the shear-gradient increases and the particle size decreases and that the migration towards the channel centerline occurs more favorably as the shear-gradient decreases and the particle size increases.

Fig. 3-23 shows the distributions of 8.7- $\mu\text{m}$  (red) and 4.8- $\mu\text{m}$  (green) fluorescent particles in the cross section at the channel length of 30 cm (corresponding to  $z/H = 3,750$ ) by the projection method, at  $Re$  of 1.0 and 2.1, respectively.

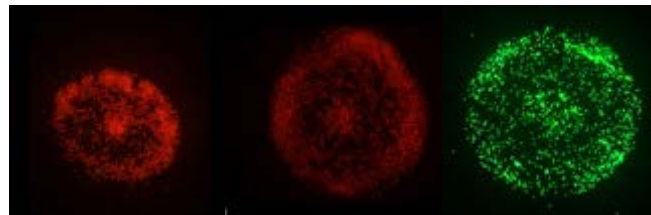


Fig. 3-23 Cross-sectional distributions of 8.7- $\mu\text{m}$  test particles on a membrane at  $Re = 1.0, 2.1$  and of 4.8- $\mu\text{m}$  test particles at  $Re = 2.1$ , from left to right respectively.

The projection method here confirms the previous conclusions on the particle to channel size ratio effect: at a given channel length, the focusing degree scales with the particle to channel size ratio, thus a longer distance is needed for small particles to complete the migration.

### 3.3 Preliminary study on biological particles

In the present work, we have studied the migration behavior of neutrally buoyant solid particles. But slightly non-neutrally buoyant particles or deformable cells are involved in the real suspensions, for example, biological particles or blood cells suspended in physiological saline, plasma of blood, etc. Besides, microorganisms significantly differ from the solid spherical particles in cell sizes, shapes, and stiffness and in some cases they can even be motile and exhibit complex aggregative forms (Kim and Yoo 2008; Lafforgue-Baldas et al. 2013).

To know how microorganisms migrate in square channel and if the developed experimental setups would be able to study their migration behavior, preliminary tests have been carried out with the yeast *Saccharomyces cerevisiae* and the bacteria *Lactococcus lactis*.

The brightfield microscopic images for the yeasts and the bacteria are shown in Fig. 3-24, to reveal the sizes and the shapes of these microorganisms. The yeasts show an ovoid shape and a mean diameter of about 6  $\mu\text{m}$  and the bacteria with a mean diameter of about 2  $\mu\text{m}$  may appear in chains. These microorganisms are chosen because their sizes are close to the polystyrene

spherical particles used in our study.

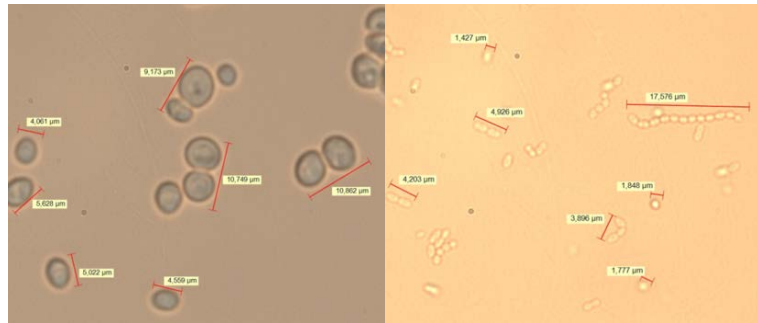


Fig. 3-24 Microscopic observation of the yeasts and the bacteria. ( $\times 1,000$  magnification)

The microorganisms are colored by fluorescent dye and the suspensions are diluted to a very low volume fraction  $\Phi \sim 0.001\%$ . The projection method has been used to observe the particle distributions at a distance of 30 cm from the channel entrance ( $z/H = 3,750$ ) at various  $Re$ .

Fig. 3-25 and Fig. 3-26 display the yeast and bacterium distributions on the plane membrane, representing their cross-sectional distributions at the channel outlet.

In Fig. 3-25, with the increasing flow rate ( $Re$ ), the yeast focusing is evidently enhanced, since the region where the yeasts concentrated become thinner. At  $Re = 16.6$ , the yeast cells begin to concentrate to some specific positions corresponding to the center of each channel face, which is very similarly to the solid spherical particles in the same range of size as shown in Fig. 3-5. Different from the yeast cells, the lactococcus bacteria seem to initiate their lateral migration at a relatively high Reynolds number  $Re = 16.6$ , as shown in Fig. 3-26. This behavior is similar to that of the 2-μm particles in our study.

Obviously, the yeasts were concentrated to the equilibrium positions at lower  $Re$  than the lactococcus bacteria, suggesting that a yeast/bacterium separation could be possible.

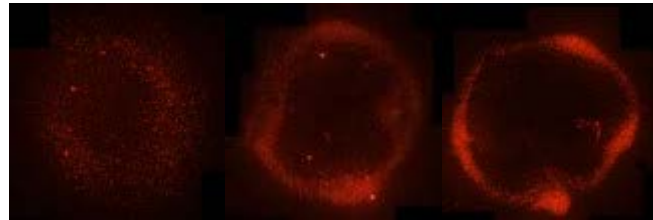


Fig. 3-25 Cross-sectional distributions of yeasts on a membrane at  $Re = 8.3, 12.5$  and  $16.6$ , respectively.



Fig. 3-26 Cross-sectional distributions of bacteria on a membrane at  $Re = 12.5$  and  $16.6$ , respectively.

Fig. 3-27 shows the brightfield microscopic image of the yeasts, taken using the *in situ* visualization method at the channel midplane at  $Re = 56$  and  $z/H = 1,000$ . The yeasts are focused near the centers of the lateral channel faces, confirming the observations by the projection method shown in Fig. 3-25.

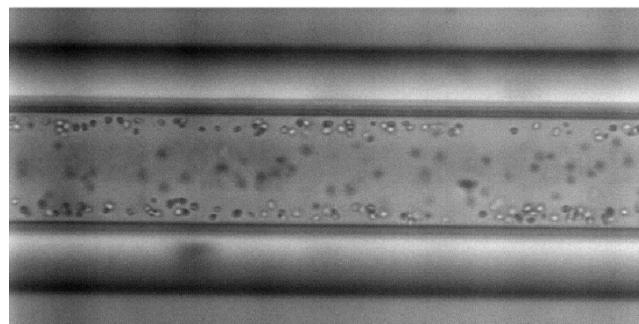


Fig. 3-27 Microscopic image of the yeast cells in a micro channel at  $Re = 56$  and  $z/H = 1,000$ .

As a conclusion, despite their non-spherical shape, their slightly non-neutrally buoyancy characteristic and their deformability, the yeast (*Saccharomyces cerevisiae*) and the bacteria (*Lactococcus lactis*) laterally migrate similarly to the solid spherical particles and could be studied with our devices. This is in agreement with the observations made by other authors (Cox and Mason 1971; Hur et al. 2011b; Mach and Di Carlo 2010; Uijtewaal et al. 1994) who reported that deformable biological particles exhibit similar migration behaviors as solid

spherical particles.

### 3.4 Summary

An empirical study based on the *in situ* visualization method has been carried out to identify and characterize the inertial focusing behavior of neutrally buoyant particles in square microchannel flows, for Reynolds numbers  $Re$  ranging from 0.07 to 280.

The determination of particle spatial distributions (PDFs) provides an experimental frame of reference allowing a better understanding of the physical basis of inertial migration. The empirical results show that two regimes of migration are observed depending on the different parameters (Reynolds number  $Re$ , channel entry length  $z/H$ , particle volume fraction  $\Phi$ , and particle to channel size ratio  $d_p/H$ ):

- At moderate flow inertia (approximately  $Re > 10$  in the flow conditions studied in this work), particles migrate towards the channel faces and undergo a two-stage migration: a lateral migration to form an annulus around the channel perimeter and a cross-lateral migration towards the centerlines of the channel faces. The first stage is a relatively fast process; the second stage is slower, takes place only when the first one is fully developed, and is favored by larger  $Re$ , longer channel, and larger particles.
- At extremely low but not negligible flow inertia (approximately  $Re < 1$  in our case), particles migrate towards and focus near the channel centerline, which had never been reported, up to now, in the literature. This migration is very slow and long channels are needed to attain the equilibrium position. The length required to complete the migration decreases with increasing particle to channel size ratio;
- For Reynolds numbers ranging from 1 to 10, both regimes of migration coexist, of which the dominant one depends on the Reynolds number, the particle size and the channel entry length. Smaller  $Re$ , longer entry length and larger particle to channel size ratio favor the migration towards channel centerline.

Besides, a quantification of the equilibrium position localization at the channel cross section and the outermost edge of particle distribution have been carried out based on the PDFs of the particle distribution. This can be helpful to optimize the design parameters for developing a microfluidic device devoted to particle separation.

In addition, we have highlighted in this chapter the phenomenon of migration towards the channel centerline at low Reynolds number. This provides a great advantage in separating large particles that are shown to migrate towards the centerline more rapidly. In particular, some fragile biological particles (such as HPET cells with a diameter of 18 - 22  $\mu\text{m}$ ) might be lysed due to the high shear forces in high flow rate conditions (Zhou et al. 2013a), and thus could not be separated by conventional microfluidic devices based on the migration towards the channel faces at moderate Reynolds numbers. The low flow inertia reduces the shear forces and makes the separation possible, avoiding hemolysis (Mach and Di Carlo 2010). The need of relatively great channel length could be overcome using serpentine or spiral channels, which could reduce the practical device dimension.



# Chapter 4. Particle Alignment

During the course of investigating the “tubular pinch effect” phenomenon, Segré and Silberberg firstly noticed the phenomenon of particle alignment (Segré and Silberberg 1962b). However, they just briefly mentioned these particle chains as a phenomenon occurring at high concentration without a systematic investigation. This inertial ordering of particles into trains has been later observed in circular pipes (Matas et al. 2004a), square microchannels (Di Carlo et al. 2007) and rectangular microchannels (Edd et al. 2008; Humphrey et al. 2010; Hur et al. 2010; Lee et al. 2010).

Although studied in a phenomenological manner by some authors, there is not yet a full consensus on the role of the hydrodynamic flow parameters and the geometric channel characteristics on the interparticle spacing. Furthermore, the fraction of particles in trains as a key parameter to characterize a given configuration has been rarely studied. In short there is a real lack of statistical studies on the formation and evolution of trains.

In the chapter, we statistically investigate the particle trains in a square and a rectangular channel, for various flow configurations, using *in situ* flow visualization. First, we probe into the physical principles by a bibliographic study helping in the understanding of the longitudinal ordering mechanisms. Then we present experimental results obtained by image analysis techniques and in particular extract two main parameters which are the fraction of particles in trains  $\psi$  and the interparticle distance  $l$  thanks to image analysis techniques. A systematic study of different factors such as distance from channel inlet, volume fraction, particle to channel size ratio and Reynolds number is performed. The dynamics of particle self-ordering is also investigated along the channel length.

## 4.1 Bibliographic study

The origin of this phenomenon could be attributed to the interactions between the fluid and the particles, involving the effect of the fluid on particles, the interactions between particles and the

effect of particles on the fluid flow (Amini et al. 2014). Streamlines around an isolated sphere in a simple shear flow were firstly numerically predicted Mikulencak and Morris (2004). As seen in Fig. 4-1, streamlines in the proximity of the particle first approach and then move away from the particle in its reference frame.

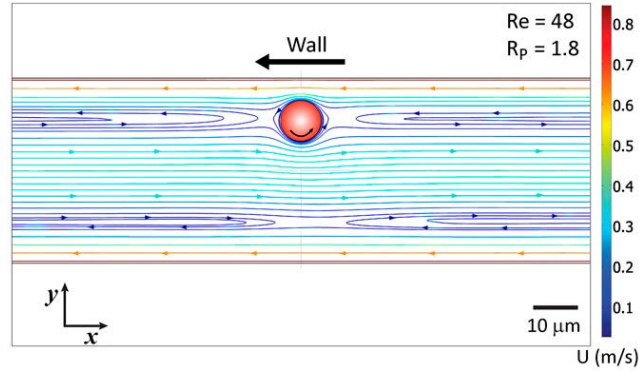


Fig. 4-1 Simulated streamlines around an isolated sphere for  $Re = 48$ . (Reprinted from (Lee et al. 2010).)

(Matas et al. 2004a) suggested that these so-called “reversing streamlines” are essential for the formation of particle trains. Pair trajectories in finite inertia suspensions of neutrally buoyant particles were determined by Morris and co-workers (Haddadi and Morris 2015; Kulkarni and Morris 2008b) using lattice-Boltzmann simulations, confirming the role of the reversing streamline zones on the relative movement between particles. Humphry et al. (2010) simulated the motion of a pair of spheres that are initially separated by given distances in the flow direction but located at their inertial focusing equilibrium positions. The pair moves closer on a damped oscillatory trajectory and eventually reaches a steady axial spacing. This oscillatory motion through which stable self-assembled pairs are formed was experimentally observed by Lee et al. (2010) using high-speed imaging. Based on these observations, Lee suggested a mechanism for the dynamic self-assembly process. When a quick particle (lagging one) is catching up a slow one (leading one), once they approach each other, the lagging particle is influenced by the drag force of the reversing streamlines due to the leading one, and the drag force will act to slow down the quick one until it reaches the average intersected fluid speed. So the quick particle will be pushed by the streamlines in the opposite direction and move slightly toward

the channel walls to slow down, following the opposite direction streamline. The leading particle with a slower speed will also be affected by the drag force of the reversing streamlines due to the quick one, which accelerates and directs it slightly towards the channel center, following the streamline in the main flow direction. At the same time, the inertial lift force directs them back to their sharp focusing positions when they are far from their equilibrium positions as shown in Fig. 4-2. This motion resembles harmonic oscillations with damping until they reach simultaneously the center (or vortex) of the reversing streamlines and the inertial focusing positions, where neither the drag force of the fluid, nor the inertial lift force acts.

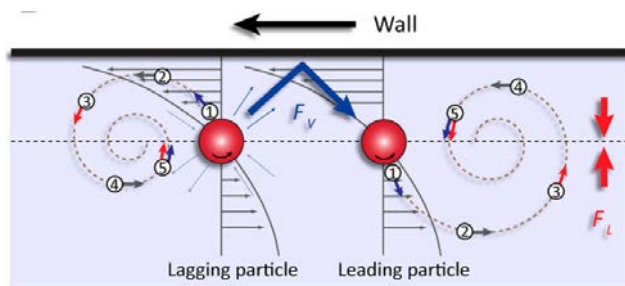


Fig. 4-2 Schematic drawing of the interaction between two aligned particles. (Reprinted from (Lee et al. 2010).)

Lee et al. (2010) also observed that the dynamics for more than two particles mainly follows the same mechanism: the train elongates through additional particles joining already organized particle pairs or trains of particles, and particle-particle interactions within a train, evidenced by oscillations and acceleration patterns during interaction, are essentially the same as in two particle interactions. Kakheshani et al. (2016) however mentioned that, considering that the disturbance streamlines around a single particle are affected by the presence of other particles, the fundamental description of the flow leading to train formation remains an open question. They showed, in particular, that the concentration of suspension impacted the most probable spacing between particles in trains.

## 4.2 Characterization of particle trains

### 4.2.1 Identification of trains

The experimental setup for particle train identification is depicted schematically in Fig. 4-3a. The appearance of the trains of particles becomes visually evident at  $Re_p \sim 0.2$  and dramatically robust ordering phenomenon was observed above  $Re_p \sim 0.5$  in our case. To illustrate this phenomenon, Fig. 4-3b and Fig. 4-3c show two brightfield microscopic images of relatively long trains of particles at moderate particle Reynolds numbers (defined as  $Re_p = Re(d_p/H)^2$  where  $d_p$  is the particle diameter), where the trains are defined as an array with three or more particles aligned. The particles in Fig. 4-3b are bright, indicating their localization in the focal plane (the focus located at the midplane of the channel). The particles are aligned near the wall, i.e., focused at the center of the front and back walls of the micro channel and form regular trains. In Fig. 4-3c, particles without bright points, i.e., out of the focal plane, apparently align at the center of the bottom wall. These considerations are consistent with the inertial focusing equilibrium positions previously observed in square channels (Abbas et al. 2014).

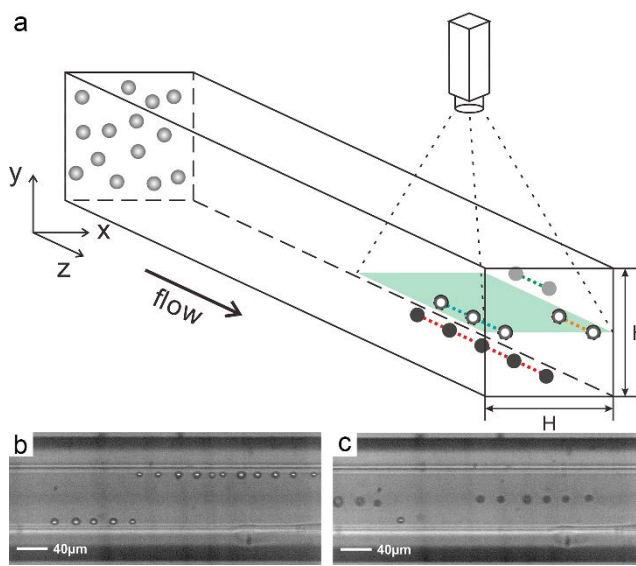


Fig. 4-3 (a) Schematic drawing of the experimental setup. Examples of image recorded of particle trains at mid height ( $y/H = 0.5$ ),  $z/H = 1,000$ ,  $\Phi = 0.1\%$  and (b)  $Re = 210$  ( $Re_p = 2.48$ ), (c)  $Re = 112$  ( $Re_p = 1.32$ ).

Trains are identified when three or more particles are aligned with a regular interparticle spacing. In Fig. 4-3b, particles considered in trains are highlighted by the yellow rectangles, particles considered out of trains and in the focal plane are indicated by the red circles and particles out of trains and out of the focal plane are indicated by the green triangles. The total number of particles in and out of trains is calculated over the set of 2,000 images and the fraction of particles in trains (i.e., the total number of particles in trains normalized by the total number of particles) is thus evaluated. This fraction is underestimated since some trains are sliced in some images and might thus be non-identified by the data processing method. Finally, the Probability Density Function (PDF) of axial spacing between centers of consecutive particles  $l$  normalized by the particle diameter  $d_p$  is computed for particles self-assembled into trains, and the highest peak is identified and chosen as a metric of the most probable spacing between consecutive particles in trains. The PDFs of the axial spacing between particles at  $\Phi = 0.1\%$ ,  $Re_p = 0.33$  and 3.31 (corresponding to  $Re = 28$  and 280) and  $z/H=1,000$  are presented in Fig. 4-3c. In these two examples, the most probable spacing between consecutive particles in trains is thus determined as  $l/d_p = 4$  at for  $Re_p = 0.33$  and  $l/d_p = 2.5$  at for  $Re_p = 3.31$ .

The observations of trains of particles presented in this section are all realized at the same distance from the channel inlet ( $z/H = 1,000$ ) and the same height in the channel ( $y/H = 0.5$ ), taking into account all particles. Indeed, since our goal in this section is to identify and characterize the trains whatever they are located, both in-focus and out-of focus particles are taken into account. Moreover, we have verified that the results obtained at the seven different heights that were used in Chapter 2 were similar and we thus decided to limit the measurement at the midplane to save time.

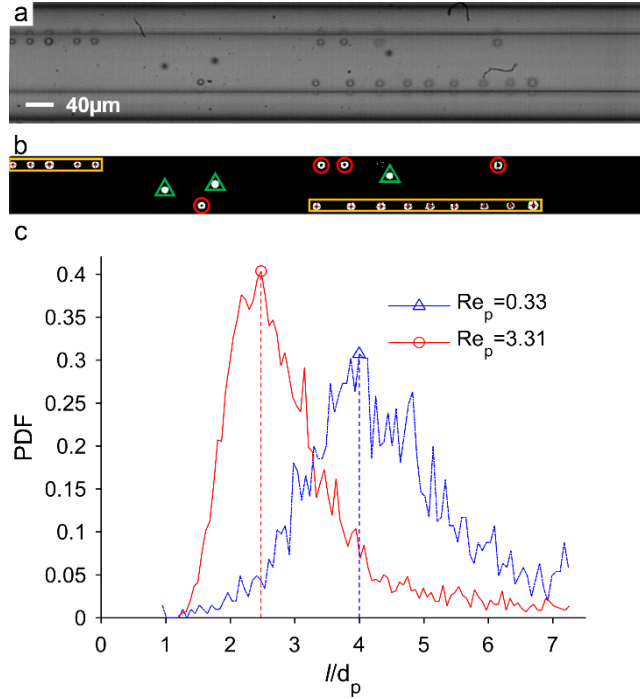


Fig. 4-4 (a) Original gray-scaled image horizontally rotated. (b) Post-processed image where particles in trains are highlighted by rectangles. (c) PDFs of the normalized interparticle spacing for  $Re_p = 0.33$  and 3.31,  $\phi = 0.1\%$  and  $z/H = 1,000$ .

#### 4.2.2 Effect of $Re_p$ and $d_p$

The fraction of particles in trains  $\psi$  is displayed with respect to the particle Reynolds number and the channel Reynolds number in Fig. 4-5a and its inset, respectively, for two confinements:  $d_p/H = 0.11$  (at  $\Phi = 0.1\%$ ) and  $d_p/H = 0.06$  (at  $\Phi = 0.02\%$ ). These two different volume fractions are set to ensure the same number of particles in a given volume. The error bars represent the amplitude of the variations observed in the six experiments done for each operating condition and indeed, the square and triangle symbols correspond to the mean value of  $\psi$ . The last result obtained at  $Re_p = 3.33$  could not be reproduced unfortunately, due to clogging problems. The fraction of particles in trains  $\psi$  first increases with  $Re_p$ . As we will see in section 4.3 trains are formed only when particles have reached the four equilibrium positions. Since the images used to study the fraction of trains are recorded at a constant distance from the channel inlet, the increased number of particles in trains is related to the shorter downstream

length required for the establishment of particle equilibrium positions when the Reynolds number is increased. This could also be explained by the fact that, when the particle Reynolds number increases, the region of reversed flow streamlines around a reference particle in a shear flow becomes wider (Haddadi and Morris 2015; Kulkarni and Morris 2008a). This phenomenon favors relative particle trapping and increases the number of particles in trains at a given concentration.

The fraction of particles in trains reaches a maximum around  $Re_p = 1.82$  (i.e.,  $Re = 154$ ) and decreases for higher particle Reynolds numbers as illustrated in Fig. 4-5a. This Reynolds number correspond to the minimum  $Re$  necessary to reach a fully-developed inertial migration process at a distance  $z/H = 1,000$  from channel inlet. Matas et al. (2004a) obtained a similar tendency in a circular pipe flow. The reason for the decrease of  $\psi$  is still elusive. This could be due to the increase of particle agitation or dispersion with the Reynolds number and therefore, the decrease of particle trapping in the reversed flow zone. In addition, Kahkeshani et al. (2016) observed, thanks to lattice Boltzmann numerical simulations, that for larger concentration of particles, the interparticle distance keeps fluctuating in time and never reaches a steady value. The disruption of trains, due to the onset of temporal fluctuations in the spacing between the particles, might thus also have a role on the decrease of the fraction of particles in trains at higher Reynolds number.

The fraction of particles in trains is higher for  $d_p/H = 0.11$  than for  $d_p/H = 0.06$  at the same channel Reynolds numbers, indicating that the particle confinement enhances the formation of trains (cf. inset of Fig. 4-5a). This could be explained by the fact that large particles create larger reversing streamline regions, catching more easily lagging particles. (Haddadi and Morris 2015; Kulkarni and Morris 2008a)

Moreover, the data for  $d_p/H = 0.11$  and  $d_p/H = 0.06$  collapse quite well to a single curve (cf. main plot of Fig. 4-5a), suggesting that the  $Re_p$ , characterizing the shear flow seen by a particle, controls the train formation (Fig. 4-5a). These results are consistent with the data of Matas et al. (2004a) obtained in circular pipe flow for  $Re$  between 0 and 3,000. It is to be noticed that at

the same confinement ( $d_p/H \sim 0.05$ ), the maximal proportion of particles in trains reaches 40 % in the square channel whereas it reaches only 15 % in a tube (Matas et al. 2004a). The difference is certainly due to the fact that the equilibrium positions are restricted to four points in the cross section of a square channel flow, whereas they are distributed on a ring in a tube flow. Therefore, the probability of pair assembly is enhanced in the square channel flows.

The interparticle distance (centre-to-centre distance) normalized by the particle diameter  $l/d_p$  is presented in Fig. 4-5b as a function of the particle Reynolds number  $Re_p$ . The deviation on the most probable interparticle distance between the six experiments (not represented in this figure) is always less than 1  $\mu\text{m}$ , that is, smaller than 5 % of  $l/d_p$ .

The normalized interparticle distance  $l/d_p$  is found to depend not only on the particle Reynolds number, but also on the confinement effect. In the studied range of particle Reynolds numbers, the normalized interparticle distance decreases with  $Re_p$ . This is in agreement with the reports of Morris and co-authors (Haddadi and Morris 2015; Kulkarni and Morris 2008a; Mikulencak and Morris 2004), who claim that the distance between consecutive particles is set by the reversing streamline region around a particle in shear flow which gets closer to the reference particle surface when the particle Reynolds number increases.

When the distance between the surfaces of two consecutive particles normalized by channel dimension,  $(l-d_p)/H$ , is plotted as a function of the particle Reynolds number (Fig. 4-6), the data obtained for the two different confinements (blue squares and red triangles) collapse quite well to a single curve which is not the case for the distance between the centers of two consecutive particles. More configurations, varying  $d_p/H$ , should be investigated to confirm this tendency but we can already conclude that the key parameter is the distance between the surfaces of two consecutive particles and not the distance between their centers. This is also confirmed by the data of Matas et al. (2004a) reported in this figure and obtained for similar weak degrees of confinement (between  $d_p/H = 0.03$  and  $d_p/H = 0.06$ ), even if in this case the surface to surface distance surprisingly decreases for low  $Re_p$ . Our data are also similar to those reported by Humphry et al. (2010) in a rectangular channel.

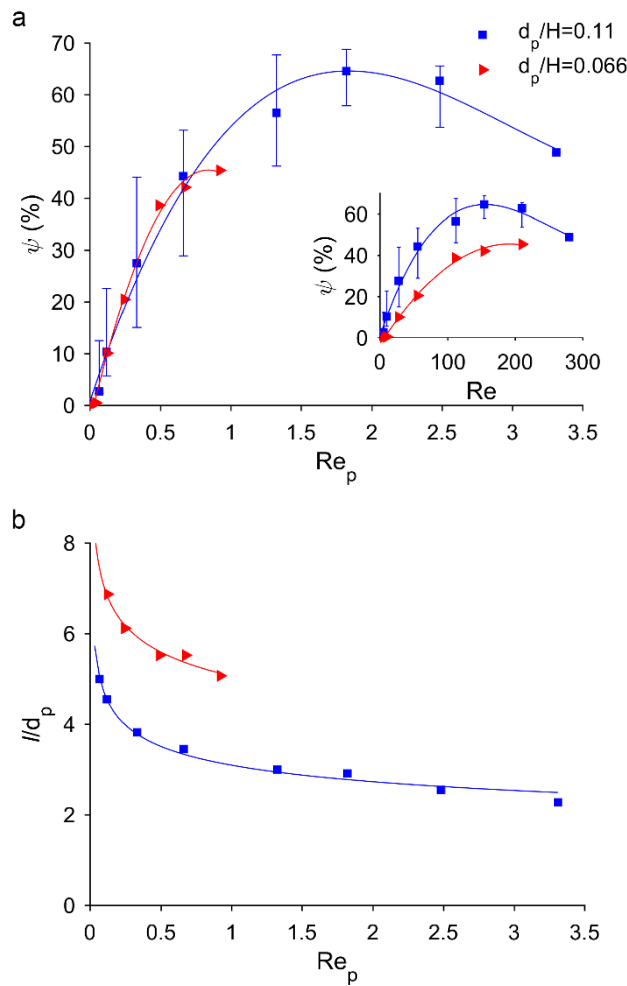


Fig. 4-5 (a) Fraction of particles in trains  $\psi$  as a function of particle Reynolds numbers  $Re_p$  and channel Reynolds numbers  $Re$  (inset) for  $d_p/H = 0.11$  and  $d_p/H = 0.066$ . (b) Normalized interparticle distance  $l/d_p$  as a function of particle Reynolds numbers  $Re_p$  for  $d_p/H = 0.11$  and  $d_p/H = 0.066$ .

Other reported punctual values of surface separation normalized by the hydraulic diameter,  $(l-d_p)/H$ , have also been reprinted in Fig. 4-6 for different experimental conditions.

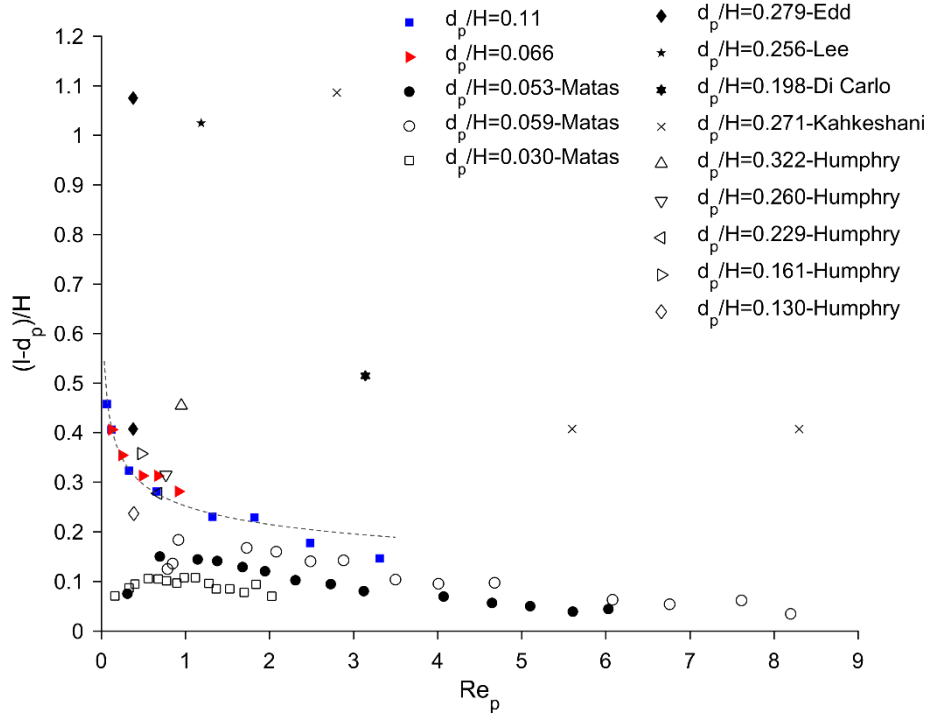


Fig. 4-6 Normalized separation distance  $(l-d_p)/H$  as a function of particle Reynolds numbers  $Re_p$  for  $d_p/H = 0.11$  and  $d_p/H = 0.066$ .

It can be seen that high confinement ( $d_p/H > 0.2$ ) can lead to high surface separation as shown by the reported data of Di Carlo et al. (2007), Edd et al. (2008), Humphry et al. (2010), Lee et al. (2010) and Kahkeshani et al. (2016). However these reported data have all been obtained in specific configurations. Lee et al. (2010) and Kahkeshani et al. (2016) used a two-inlet co-flow within a rectangular channel which reduced the degrees of freedom of the particles and increased their confinement leading to their focusing in a single line. For highly confined particles in rectangular channels, Edd et al. (2008) and Humphry et al. (2010) observed two classes of trains: either particles aligned themselves with the same equilibrium position along one side of the channel or particles alternated from one side of the channel to the other one. . Edd et al. (2008) thus gave two interparticle distances, one for “same streamline” trains and one for alternated trains at the same  $Re_p$  (cf. Fig. 4-6). We also observed alternated trains in preliminary results obtained in high confinement configurations in rectangular channels. Due to the small dimensions of the channel, the reversing streamlines in the other half of the channel are sufficiently close to the particle to create either an alternated pair or a “same streamline”

pair whether the second particle arrive on the same channel side or not.

### 4.2.3 Low inertia

As highlighted in Fig. 3-14, at low flow inertia (typically  $Re_p < 10^{-2}$ ), a second regime of migration in which particles concentrate in the channel center is highlighted by Abbas et al. (2014). Fig. 4-7 shows two typical brightfield images of the suspension at  $Re_p = 8 \times 10^{-4}$  and  $Re_p = 8 \times 10^{-3}$ , respectively. Particles are preferentially encountered at the center of the channel indicating that most of them have reached their equilibrium position. Nevertheless, they are roughly aligned, and the irregular interparticle distances suggest that no train is established.

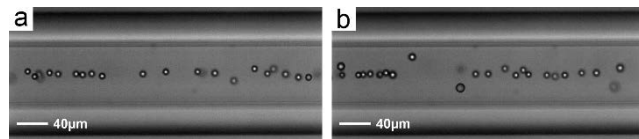


Fig. 4-7 Images of the suspension at  $y/H = 0.5$ ,  $z/H = 1,000$ ,  $\Phi = 0.4\%$  and (a)  $Re_p = 8 \times 10^{-4}$  ( $Re = 0.07$ ) (b)  $Re_p = 8 \times 10^{-3}$  ( $Re = 0.7$ ).

As mentioned before, the pair's formation is linked to the presence of reversing streamlines which also exist at low inertia and even for Stokes flow in confined configurations (Zurita-Gotor et al. 2007). In the pair interaction mechanism, these reversing streamlines initiate drag forces (viscous disturbance flow in (Lee et al. 2010), stresslet disturbance flow in (Zurita-Gotor et al. 2007)) which push the two particles away from their focusing position, in transverse and opposite directions. Inertial lift forces direct then the particles back to the focusing line (Lee et al. 2010). This interplay between viscous disturbance flow and lift forces explain the oscillatory relative trajectories of the particles observed by these authors during the self-assembly process. However, the closed streamline regions around the particles expand when  $Re$  decreases, moving thus away the reversing zones from the particle (Haddadi and Morris 2015). In addition, the repulsive interaction initiated by the viscous disturbance flow decays with  $1/l^2$  (Lee et al. 2010; Zurita-Gotor et al. 2007) and will thus decrease when the reversing zones move away from the particle with the decrease of  $Re$ . This could explain the vanishing of the self-assembly process

observed at low inertia.

#### 4.2.4 Effect of solid volume fraction

The influence of the particle volume fraction on the formation of particle trains is analyzed from the observations realized at the end of the channel ( $z/H = 1,000$ ), with particle to channel size ratio  $d_p/H = 0.11$  and particle volume fractions  $\Phi$  ranging from 0.02 % to 1 %. The evolution of the fraction of particles in trains and interparticle distance as a function of  $Re_p$  are illustrated in Fig. 4-8.

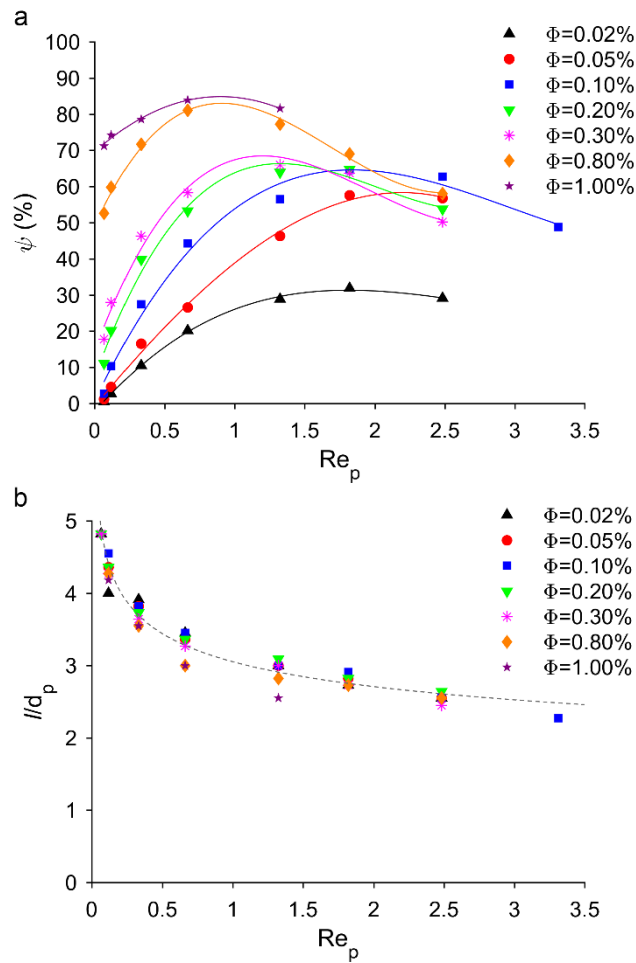


Fig. 4-8 (a) Fraction of particles in trains  $\psi$  and (b) normalized interparticle distance  $l/d_p$  as a function of particle Reynolds number  $Re_p$  for  $d_p/H = 0.11$ ,  $z/H = 1,000$  and  $\Phi = 0.02\%, 0.05\%, 0.1\%, 0.2\%, 0.3\%, 0.8\%$  and  $1\%$ .

For all the studied concentrations, the evolution of the fraction of particles in trains with  $Re_p$  is

similar: this fraction increases with  $Re_p$ , reaches a maximum and then decreases (Fig. 4-8a). With increasing concentrations, the maximal value of the fraction of particles in trains increases too and is reached for lower  $Re_p$ . It could be thus assumed that higher concentrations enhance particle self-assembly at small  $Re_p$ , which is no more the case at higher  $Re_p$  (around 2). Kakheshani et al. (2016) also mentioned that at high concentrations, stable trains were no longer observed due to temporal fluctuations in interparticle spacing.

The interparticle distance exponentially decreases while increasing  $Re_p$  and turns out to be independent of the concentration, as illustrated in Fig. 4-8b. Nearly all the data obtained for different concentrations are well fitted by an exponential function (dashed line in Fig. 4-8b). However, a few points obtained for the highest concentrations, i.e.,  $\Phi = 0.8\%$  and  $\Phi = 1\%$ , are located below the fitting line. The number of particles per unit length, or length fraction,  $\lambda = \Phi (H^2/\pi d_p^3)$  was calculated to quantify the proximity between particles in the suspensions. If  $\lambda > 4/l$ , where 4 is the number of equilibrium positions in square channels, steric crowding effects, as defined by Di Carlo (2009), appear. Under the present experimental conditions,  $\lambda > 4/l$  is verified for  $Re_p < 1$  when  $\Phi = 0.8\%$  and for  $Re_p < 3$  when  $\Phi = 1\%$ . In that case, the interparticle distance decreases so that all particles can take place on one of the four equilibrium positions. This is confirmed by the experimental data presented in Fig. 4-8b. The diamond symbols representing  $\Phi = 0.8\%$  are located below the fitting line at  $Re_p = 0.33$  and  $0.66$ ; the same phenomenon for  $\Phi = 1\%$  represented by five-pointed star symbols at  $Re_p = 0.33, 0.66$  and  $1.32$ . As long as the crowding limit is not reached, the interparticle distance is found to be independent of the concentration. Humphry et al. (2010) also found that the interparticle distance does not depend strongly on the volume fraction in rectangular microchannels. However, whenever the crowding limit was reached, he observed the formation of a parallel additional train neighboring the first one that was located on the equilibrium position. It would have been interesting to increase even more the particle concentration in the present experiments to check if such multiple parallel trains also appear in square channel. But this was not possible due to clogging problems.

#### 4.2.5 Particle trains in rectangular channels: preliminary results

Different from the particle trains in circular and square channel flows (Di Carlo et al. 2007; Matas et al. 2004a), the particle trains in rectangular microchannel flows show an alternating pattern, i.e., the particles are ordered into the same streamline along one side of the channel or arranged into arrays alternated from one side of the channel to the other (Edd et al. 2008). Note that the selection of particle focusing position is intrinsically a random event which leads to diverse patterns in the organized structure (Lee et al. 2010).

A preliminary study was carried out in this work using rectangular channels with a high aspect ratio ( $\sim 10$ , i.e.,  $50 \mu\text{m} \times 500 \mu\text{m}$ ) to observe this phenomenon. The flow in such a channel can be considered as a 2D planar Poiseuille flow, where the inertial focusing positions are the two plane layers parallel to the two large faces of the channel (Asmolov 1999). Fig. 4-9 shows the particle trains observed in our rectangular channel. Both in-focus particles (i.e., ones with well-defined contours) and out-of-focus particles (i.e., ones with blurred contours) are visible in a same train, suggesting that they are aligned alternatively at the two side of the channel.

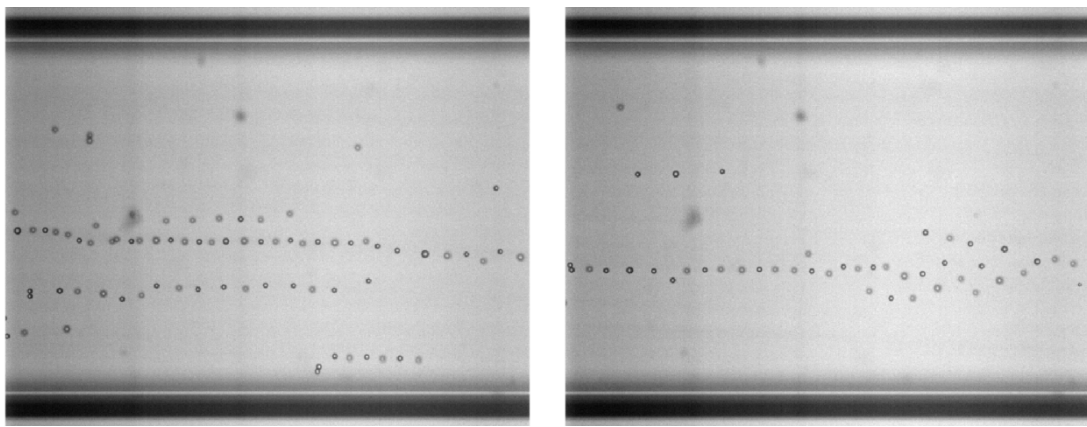


Fig. 4-9 Staggered particle trains in rectangular channels.

This alternating pattern occurs when the confinement is high enough to create, in the surrounding of the particle, two zones of reversing streamlines located in the upper side and in the lower side of the channel as suggested by Humphry et al. (2010) (cf. Fig. 4-10). In this configuration, particles can be trapped in either of these reversing streamlines zones.

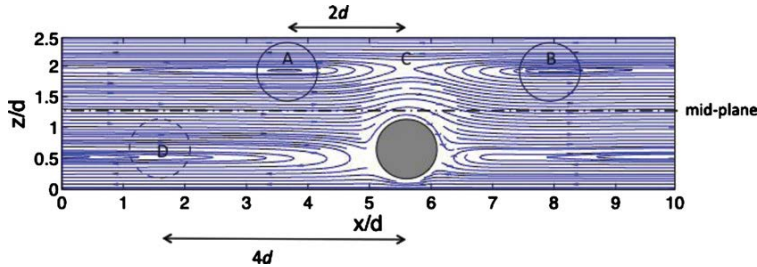


Fig. 4-10 Streamlines around an isolated particle computed using lattice Boltzmann simulations. The solid and dotted circles suggest positions of adjacent particles (reprinted from (Humphry et al. 2010)).

In rectangular channels with high aspect ratio, the inertial equilibrium positions are planes rather than lines as indicated before. This might explain several other observations in Fig. 4-9:

- Some parallel particle trains coexist, which is consistent with observation of parallel rows in rectangular channels by Humphry et al. (2010). He suggested that the number of rows depends on the particle volume fraction.
- Long trains can be inclined of a small angle relative to the main flow direction, which is consistent with the results of Matas et al. (2004a) in a cylindrical channel.
- The so called “tree-shape trains” (Fig. 4-9b) with several branches linked together were observed, suggesting that a single particle can lead several lagging ones.

The fraction of particles in trains has been evaluated as a function of  $Re$  and is shown in Fig. 4-11. This fraction increases with increasing  $Re$ , similar to the evolution in the square channel. Even at a low concentration  $\Phi = 0.01\%$ , the percentage of the particles in trains can reach up to more than 80 %, which is higher than the value obtained at the same volume fraction and the same distance from channel inlet in a square channel. This augmentation is considered to be related to the higher confinement of the rectangular cross section. The high aspect ratio rectangular shape and its wide equilibrium position could also play a role. More investigations are needed to clarify this observation. Besides, the presence of long particle trains (more than 30 particles in a single train) in rectangular channel can also be a reason for the high particle volume fraction in trains.

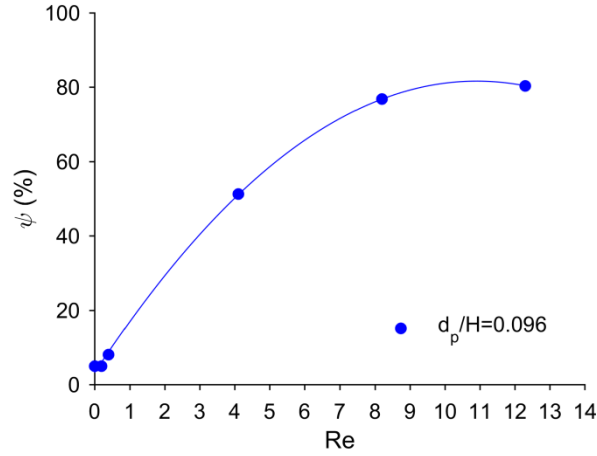


Fig. 4-11 Fraction of particles in trains  $\psi$  as a function of Reynolds number for  $z/H = 1,000$  and  $\Phi = 0.01 \%$ .

The normalized interparticle distance,  $l/d_p$ , is found to be around 3.38 for  $Re$  equal to 4, 8 and 12. No interparticle distance could be evaluated in the present experiments for lower Reynolds due to the small number of trains.

These preliminary results show similarities and differences between square and rectangular channels. A complete statistical study is necessary for a better understanding of these observations.

### 4.3 Dynamics of particle self-ordering

To better understand the dynamics of particle self-ordering in square channels, trains are observed at different distances from the channel inlet. The fraction of particles in trains  $\psi$  and the normalized interparticle distance  $l/d_p$  are presented as a function of the normalized downstream distance from channel inlet  $z/H$  in Fig. 4-12 for  $d_p/H = 0.11$ ,  $\Phi = 0.1 \%$  and different particle Reynolds numbers  $Re_p$ . Long channels (60 cm long) are used at low Reynolds number ( $Re_p = 0.07$ ) in order to allow particles to get closer to their focusing position (channel centerline), medium channels (30 cm) and short channels (10 cm) are used for  $Re_p = 0.13$  and  $Re_p = 0.33$  and 1.32, respectively, to limit pressure losses.

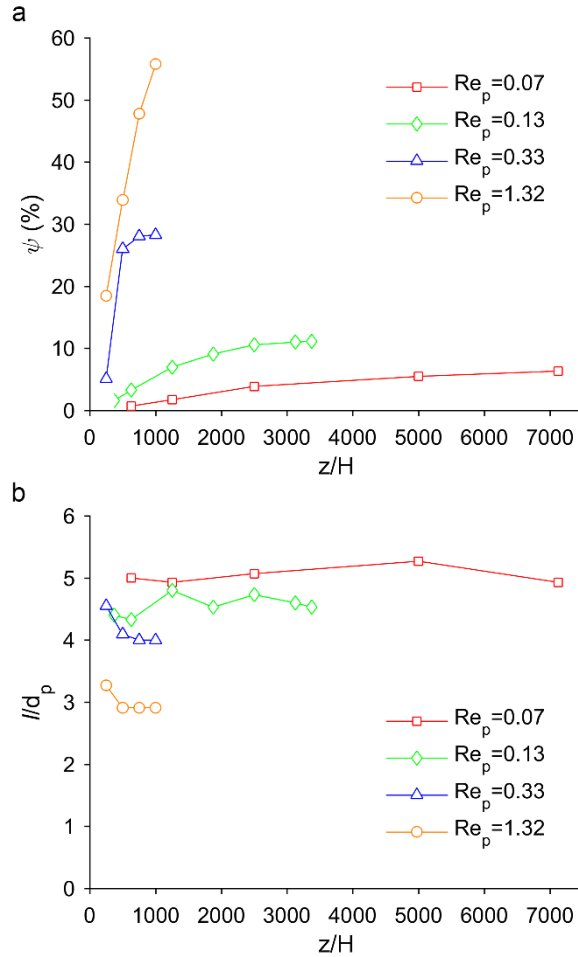


Fig. 4-12 (a) Fraction of particles in trains  $\psi$  and (b) normalized interparticle distance  $l/d_p$  as a function of normalized distance from channel inlet for  $d_p/H = 0.11$ ,  $\Phi = 0.1\%$  and different particle Reynolds numbers  $Re_p$ .

The fraction of particles in trains increases when moving downstream in the channel, indicating that trains form progressively. None of the obtained curves seems to have reached a stable level, indicating that particles certainly still join the existing trains or form new ones even far from the channel inlet ( $z/H = 7,125$  for low  $Re_p$  and  $z/H = 1,000$  for high  $Re_p$ ). This suggests that train formation is a slow phenomenon and that sufficiently long channels are needed to reach a constant fraction of particles in trains. Interparticle distance nevertheless becomes rapidly nearly constant along the channel, but its value depends on the value of  $Re_p$ . On the contrary, Lee et al. (2010) observed that the interparticle spacing continuously increased further downstream.

Since particles are “simultaneously” laterally focused and longitudinally ordered in trains while travelling downstream in the channel, it seems important to investigate the relationship between these two phenomena. Probability Density Functions (PDFs) of particles detected in the focal plane (bold red lines) and in the whole channel (dotted blue lines) are presented in Fig. 4-13 versus the normalized transverse direction  $x/H$  at  $y/H = 0.5$ , for the same experimental conditions than the ones described in Fig. 4-12. Schematics of particle distributions in the cross section are also proposed (deduced from other PDFs obtained at different heights  $y/H$  and not presented in this work).

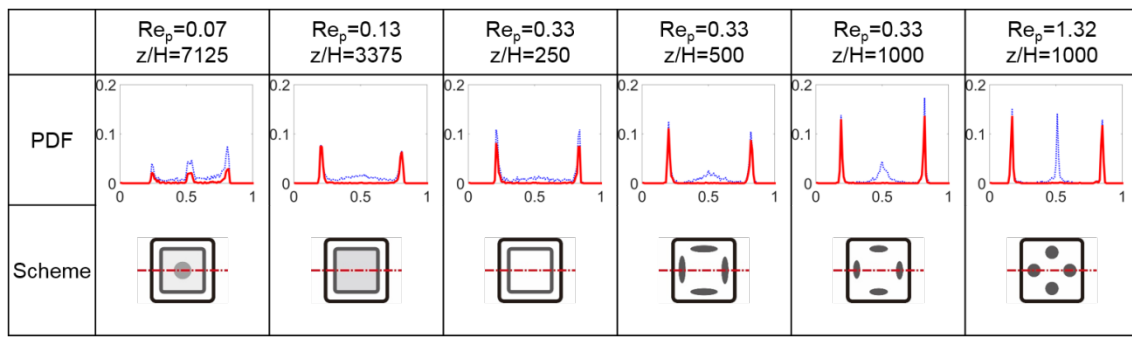


Fig. 4-13 PDFs of particles at  $y/H = 0.5$  (midplane),  $\Phi = 0.1 \%$ , for different  $Re_p$  and  $z/H$ . Bold red lines correspond to particles in the focal plane and dotted blue ones to particles present in the whole section. Schematics of the particle distributions are proposed at the bottom of the figures.

At  $Re_p = 0.07$ ,  $z/H = 7,125$ , particles are found in the channel center and in an annulus close to the wall indicating the co-existence of the two regimes of migration, at low (towards the channel centerline) and moderate  $Re$  (towards 4 equilibrium positions near the centers of the channel faces). At  $Re_p = 0.13$ ,  $z/H = 3,375$  and  $Re_p = 0.33$ ,  $z/H = 250$ , particles are concentrated in an annulus close to the channel wall indicating that they are in the first stage (lateral migration) of the moderate  $Re$  migration regime. At  $Re_p = 0.33$ ,  $z/H = 500$  and  $z/H = 1,000$ , it is apparent that all the particles have focused along the channel perimeter, according to the first stage of the migration process, but not all of them have reached the final four attractors centered at the each channel face. On the contrary, at  $Re_p = 1.32$  and  $z/H = 1,000$ , the two stages of the migration are fully completed. However, the trendline of train formation for this case in Fig. 4-12 still

increases, which seems to show that the longitudinal ordering process is slower, or starts later, than the lateral migration process.

Another important question concerns the starting point of the self-assembly process: does this process start during the lateral migration of the particles or only when these particles are focused on their final equilibrium positions?

Particles centers superposed over a set of 2,000 images are shown in Fig. 4-14, for focal plane located at different vertical heights ( $y/H$ ).  $y/H = 0.5$  corresponds to the channel midplane and  $y/H = 0.15$  to the one close to the bottom wall at  $Re_p = 0.13$  and  $z/H = 3,375$ . For each height, the particles in trains are also identified and shown separately. The numbers of particles in the focal plane and in trains are also presented by histograms.

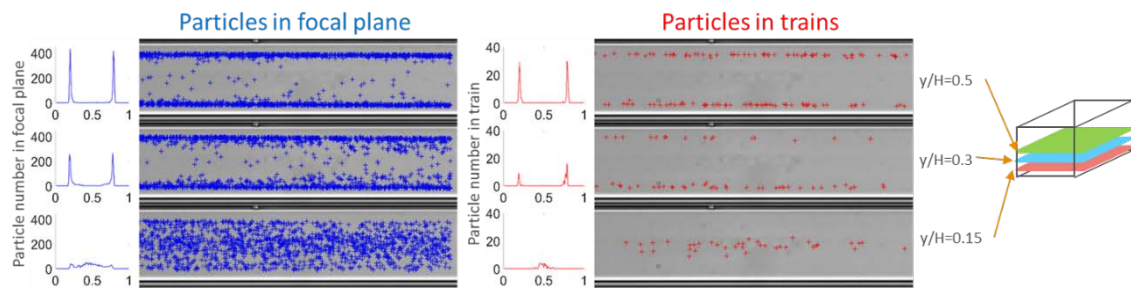


Fig. 4-14 Numbers of particles in trains at different vertical heights ( $y/H = 0.15, 0.3$  and  $0.5$ ) at  $Re_p = 0.13$  and  $Re_p = 1.32$  for  $d_p/H = 0.11$ ,  $\Phi = 0.1 \%$ .

At  $y/H = 0.5$ , particles in the focal plane are mostly located near the front and the back channel walls while at  $y/H = 0.15$ , they occupy all the layer confirming that in this configuration ( $Re_p = 0.13$  and  $z/H = 3,375$ ), particles are concentrated in an annulus close to the channel perimeter. In the same time, particles in trains are found to be located near the front and the back walls in the channel midplane ( $y/H = 0.5$ ) but only near the center of the channel in the plane close to the bottom wall ( $y/H = 0.15$ ). Even if all the particles are focused on a ring, particles in trains are only located on the four final equilibrium positions near the center of the channel faces. Similar results have been obtained for other  $Re_p$  and  $z/H$ , even near the channel inlet. Trains are thus found to be located only on the particle final equilibrium positions, indicating that the self-

assembly process concerns only particles which have completed their lateral migration.

## 4.4 Summary

In this chapter, the formation of particle trains in square microchannels has been experimentally studied. A statistical analysis of a large number of train's images, recorded and post-processed for various flow conditions and at various positions in the channel, has permitted to identify important relations between the trains' structure (fraction of particles in trains and interparticle distance) and some flow conditions such as the particle Reynolds number and the particle concentration. We have shown in particular that:

- High fractions of particles in trains can be reached in some flow configurations (up to 80% in the presently studied conditions);
- Increasing the particle Reynolds number  $Re_p$ , firstly favors the trains' formation, but leads to a diminution of the percentage of particles organized in trains over an optimal value of  $Re_p$ . With increasing concentrations, the maximal value of the fraction of particles in trains increases too and is reached for lower  $Re_p$ ;
- The distance between consecutive particle surfaces decreases when  $Re_p$  increases, independently of the particle concentration. However, if the concentration exceeds a threshold value linked to the flow confinement (and defined as the crowding limit), the interparticle distance tends to decrease in relation with the concentration augmentation;
- The train formation process only starts when the particles have reached their equilibrium position, located near the center of each channel face.

# **Chapter 5. Migration in Bidisperse Suspension: Preliminary Results**

As seen in Chapter 2, particles flowing in microchannels at moderate Reynolds numbers laterally migrate due to inertia. Moreover, particles of different sizes show different migration behaviors: small particles laterally migrate more slowly than large ones, thus taking a longer distance to focus to the equilibrium positions close to the channel walls. Taking advantage of these differences in behaviors can allow particle separation and sorting, as demonstrated by (Bhagat et al. 2008b), (Mach and Di Carlo 2010), (Zhou et al. 2013a), (Gossett et al. 2012), (Masaeli et al. 2012), (Hur et al. 2011b) or (Seo et al. 2007), who have all developed prototypes to separate polydisperse particles based on inertial microfluidic.

As seen in Fig. 4-3, particles flowing in microchannels also self-assemble to form trains during inertial migration. Although the train formation has also been reported by some authors in monodisperse suspensions, few investigations have been carried out on the trains in polydisperse suspensions. This seems nevertheless crucial to check if mixed trains are formed and how such trains could affect the sorting process.

In this chapter, we seek to investigate the effect of bidispersity on inertial focusing. More specifically, the suspension is presented firstly: a mixture of 8.7- $\mu\text{m}$  and 5.3- $\mu\text{m}$  particles is adopted to address this study. Then in the second part, the effect of bidispersity on the lateral migration is discussed. Finally, the longitudinal ordering of particles in bidisperse suspensions is presented. The lateral migration and the longitudinal ordering are studied thanks to the experimental setups presented in the preceding chapters. The results are compared with those obtained for monodisperse suspensions to reveal the effect of bidispersity. These are however only preliminary experiments aiming at discovering the trends and preparing a broader measurement campaign.

## 5.1 Suspension

In order to investigate the migration behavior of bidisperse particles, we used a mixture of two particles that have been well studied in monodisperse suspensions: the ones of diameter  $d_p = 5.3 \mu\text{m}$  and  $8.7 \mu\text{m}$ . The volume fraction of  $8.7\text{-}\mu\text{m}$  particles in the bidisperse suspension is  $\Phi = 0.05\%$  and that of  $5.3 \mu\text{m}$  diameter particles is  $\Phi = 0.01\%$ . These concentrations were chosen to ensure the same particle number of each particle in a given volume, and also the same particle number (small and large particles) in the monodisperse suspensions discussed in this chapter. Besides, a hemocytometer was used to count the different particles in a sample of the suspension and verify their concentrations.

Fig. 5-1 shows a typical brightfield image of such a bidisperse suspension at rest. The particles of two different sizes can be easily visually distinguished.

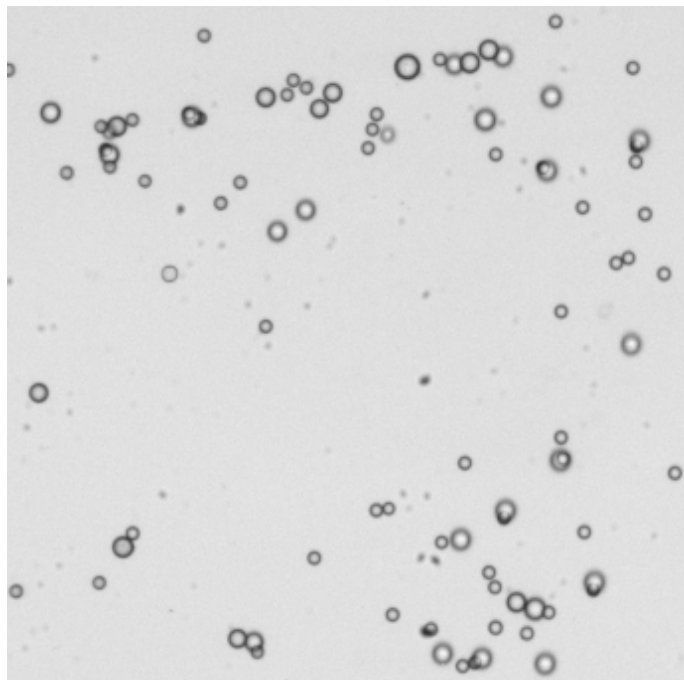


Fig. 5-1 Microscopic observation ( $50 \times$ ) of a mixture of  $5.3\text{-}\mu\text{m}$  and  $8.7\text{-}\mu\text{m}$  particles.

## 5.2 Lateral migration

The particle mixture was studied in an  $80 \mu\text{m} \times 80 \mu\text{m}$  microchannel using the *in situ*

vizualisation method described in Section 2.2, in the range of  $Re$  from 5.6 to 210, at the constant longitudinal position  $z/H = 1,000$  and at seven vertical positions, i.e.,  $y/H = 0.125, 0.25, 0.375, 0.5, 0.625$ , and  $0.875$ . The post-processing procedure for identifying the two type particles and the in-focus particles is described in section 2.2. A typical post-processed image is shown in Fig. 5-2. The  $8.7\text{-}\mu\text{m}$  particles and the  $5.3\text{-}\mu\text{m}$  particles are respectively surrounded by blue and red circles. The in-focus and out-of-focus particles are marked respectively by bold and thin circles. This image was captured at channel entry length  $z/H = 1,000$  and at the channel midplane  $y/H = 0.5$ , for  $Re = 5.6$ .



Fig. 5-2 Particle identification in the bidisperse suspension ( $Re = 5.6$ ).  $8.7\text{-}\mu\text{m}$  and  $5.3\text{-}\mu\text{m}$  particles are surrounded by blue and red circles, respectively, and the in-focus and out-of-focus particles by bold and thin circles, respectively.

Again, 2,000 images have been taken at each position and the statistical spatial distributions of both particles summarized from the 2,000 images are presented by PDFs.

The lateral migration is presented in the first section and the longitudinal ordering will be presented in the next section.

### 5.2.1 Particle distribution

Fig. 5-3 displays the post-processed image of the overall identified in-focus particles (i.e., the stack of the 2,000 images) at different vertical positions for  $Re = 5.6$  and 112, in order to have a global overview of the particle distribution. The centers of  $5.3\text{-}\mu\text{m}$  particles and the  $8.7\text{-}\mu\text{m}$  particles are marked respectively by red and blue crosses.

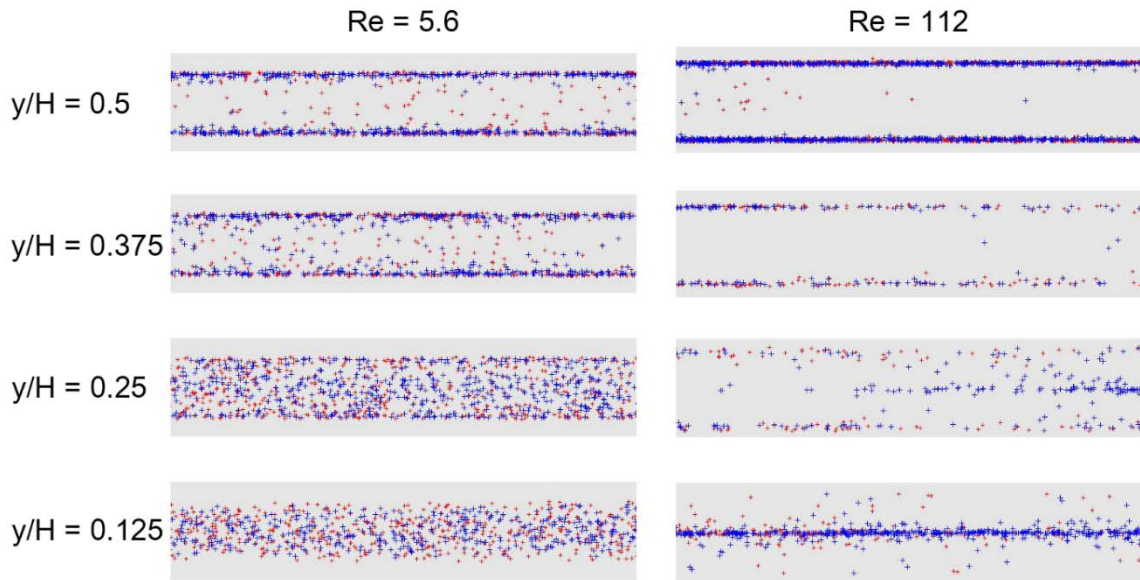


Fig. 5-3 Overall particle distributions at different vertical positions at  $Re = 5.6$  and  $112$

Firstly, the red and blue crosses are distributed in a similar way (close to the channel walls, either near the channel wall centerline, or uniformly distributed), indicating that the migration behaviors of the  $5.3\text{-}\mu\text{m}$  and  $8.7\text{-}\mu\text{m}$  particles are similar.

Secondly, at  $Re = 5.6$  which is a relatively small Reynolds number, the  $8.7\text{-}\mu\text{m}$  particles are focused near the channel walls and form a square annulus, indicating that the first stage of the inertial focusing (the lateral migration) is fully developed. In the image corresponding to  $Re = 5.6$  and  $y/H = 0.5$ , however, red crosses are still observed in the central part of the channel, indicating that the  $5.3\text{-}\mu\text{m}$  particles are less focused than the  $8.7\text{-}\mu\text{m}$  ones in this condition. At  $Re = 112$ , both small and large particles are found near the four centerlines of the channel walls. This indicates that the cross-lateral migration is in progress. These observations are consistent with the conclusion obtained at moderate Reynolds number for monodisperse particles:

- Particles undergo a two-stage inertial focusing including a lateral migration and a cross-lateral migration.
- The Reynolds number enhances the migration process: at a given distance from channel inlet, the higher the Reynolds number is, the more developed is the migration.

To better see if there is a difference in the focusing behaviors of the same particles when they are mixed in a bidisperse suspension or in a monodisperse suspension, the PDFs are separately calculated for the two types of particles at  $Re = 5.6, 10, 28$  and  $112$ , and are shown in Fig. 5-4.

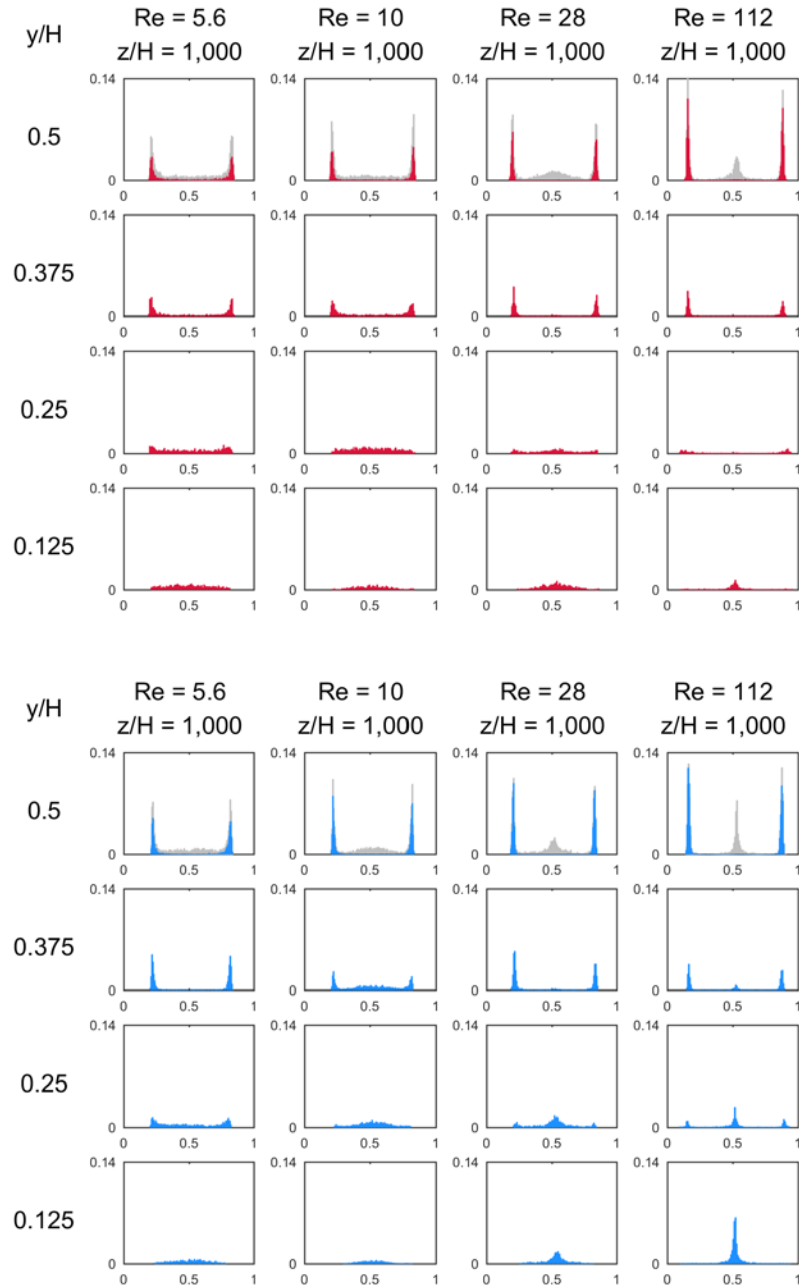


Fig. 5-4 Particle distributions (PDFs) of bidisperse  $8.7\text{-}\mu\text{m}$  (blue) and  $5.3\text{-}\mu\text{m}$  (red) particles as a function of  $Re$ , at different  $y/H$  positions and at  $z/H = 1,000$ .

These PDFs confirm the observations outlined in Fig. 5-3 concerning the focusing degree for

the two types of particles, the two-stage process and the influence of Reynolds number.

Moreover, these PDFs are very similar to those obtained with the 8.7- $\mu\text{m}$  and 5.3- $\mu\text{m}$  particles in monodisperse suspensions shown in Fig. 3-5 and Fig. 3-6. The shapes of the PDFs are identical and the peak heights are very close. These very small differences in the heights of the PDFs could be linked to the reduction of the individual volume fractions from 0.1% to 0.05% for the 8.7- $\mu\text{m}$  particles and from 0.02% to 0.01% for the 5.3- $\mu\text{m}$  ones.

From these PDFs we can conclude that no influence of the bidispersity on the migration behaviors of the two types of particles is evidenced in the investigated experimental conditions.

### 5.2.2 Equilibrium position localization

The lateral localization of the equilibrium positions ( $X_{eq}$ ) in the channel cross section have been measured for both 5.3- $\mu\text{m}$  and 8.7- $\mu\text{m}$  particles using the method described in section 3.1.4. Fig. 5-5 displays the evolutions of  $X_{eq}$  as a function of  $Re$ , for the 8.7- $\mu\text{m}$  particles ( $d_p/H = 0.11$ , represented by blue squares) and the 5.3- $\mu\text{m}$  particles ( $d_p/H = 0.066$ , represented by red triangles) in a bidisperse suspension. The results for the two same-sized particles in monodisperse suspensions are reprinted from Fig. 3-8 by the hollow symbols.

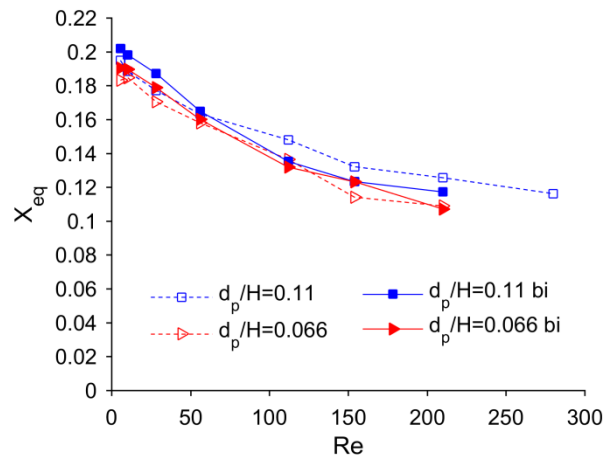


Fig. 5-5  $X_{eq}$  (normalized distance between the equilibrium position and the channel wall) as a function of  $Re$ , for bidisperse and monodisperse 8.7- $\mu\text{m}$  and 5.3- $\mu\text{m}$  particles.

The observations are again consistent with the conclusions made in the cases of monodisperse

suspensions:

- $X_{eq}$  decreases with  $Re$  for both particle sizes, indicating that the equilibrium positions get closer to the walls with increasing Reynolds numbers.
- $X_{eq}$  for the 8.7- $\mu\text{m}$  particles ( $d_p/H = 0.11$ ) are slightly greater than that for the 5.3- $\mu\text{m}$  ones, indicating that the small particles migrate closer to the channel walls than the large ones.

It can be concluded from these evolutions, that the bidispersity does not seem to influence the equilibrium positions of the two types of particles in the used experimental conditions.

The difference between the localizations of the equilibrium positions of the large and the small particles is extremely small ( $\sim 0.5 \mu\text{m}$ ) in the case studied here. It seems thus difficult to use a difference in the particle equilibrium positions to separate these two types of particles. An added system that amplifies this difference could be a solution. Since particles of different sizes do not have the same migration velocity, i.e., their inertial focusing are differently developed at a given distance from channel inlet, the kinetic separation could be possible.

### **5.2.3 Outermost edge of particle distribution**

The normalized distance between the outermost edge of the particle clusters and the channel center, i.e.,  $X_{out}$ , is plotted in Fig. 5-6 as a function of  $Re$  for the 8.7- $\mu\text{m}$  particles and 5.3- $\mu\text{m}$  particles in bidisperse suspension, and compared to the results obtained in monodisperse suspensions. The evolutions of  $X_{out}$  in bidisperse and monodisperse suspensions are also similar:  $X_{out}$  increases with increasing  $Re$  and decreasing particle to channel size ratio. It also seems that, in the used experimental conditions, the bidispersity has a weak influence on the outermost edges of distributions of the two types of particles.

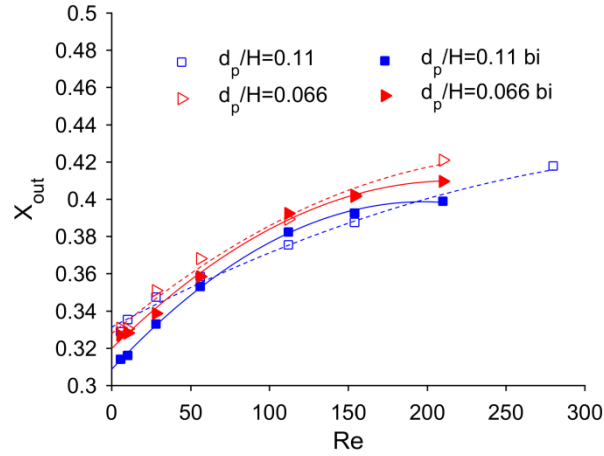


Fig. 5-6  $X_{out}$  (normalized distance between the outmost edge and the channel centerline) as a function of  $Re$ , for bidisperse and monodisperse 8.7- $\mu\text{m}$  and 5.3- $\mu\text{m}$  particles.

#### 5.2.4 Focusing degree

The quantification of the focusing degree as defined in section 3.1.6 has been performed here for both sizes of particles in bidisperse suspension and compared to the monodisperse one. The results are shown in Fig. 5-7, as a function of  $Re$ .

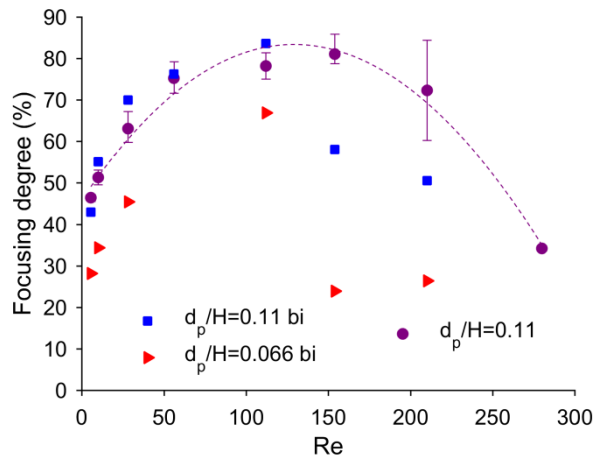


Fig. 5-7 Focusing degree as a function of  $Re$ , for bidisperse 8.7- $\mu\text{m}$  and 5.3- $\mu\text{m}$  particles and monodisperse 8.7- $\mu\text{m}$  particles.

Similar evolutions are observed for Reynolds numbers smaller than 150. For Reynolds numbers larger than 150, the bidisperse results seem incoherent for both types of particles, which could be due to image quality problems. The images corresponding to the bidisperse particles were

not enough contrasted indeed and we suppose that the strong decay of the focusing degree might be due to a bad exposure time. These experiences will be repeated to confirm this assumption.

No clear influence of the bidispersity on the migration process can be extracted from these results, even if it seems that, for Reynolds number less than 150, the blue squares corresponding to the large particles in bidisperse mixture is a bit higher than the purple circles corresponding to the same particle in a monodisperse suspension. Additional measurements have thus to be conducted to draw clearer conclusions on this point.

### 5.3 Longitudinal ordering of bidisperse particles

Fig. 5-8 illustrates the formation of trains of bidisperse particles, where the 8.7- $\mu\text{m}$  ( $d_p/H = 0.11$ ) and 5.3- $\mu\text{m}$  particles ( $d_p/H = 0.066$ ) are respectively encircled by blue and red squares. These two images are captured at the distance from the channel inlet  $z/H = 1,000$  with the focus at the channel midplane ( $y/H = 0.5$ ) at  $Re = 112$ . The upper image shows an in-focus bidisperse particle train located at the centerline of the channel front wall and the bottom one shows an out-of-focus bidisperse particle train formed at the centerline of the bottom wall. These two images confirm that linear chains of more or less uniformly spaced particles are formed like in monodisperse suspensions. In addition, they highlight that the trains can be mixed, i.e., particles of both sizes can be self-assembled in a same train. The objective of this section is to investigate how the bidispersity affects the fraction of particles in trains, the sequential ordering of trains and the interparticle distance.

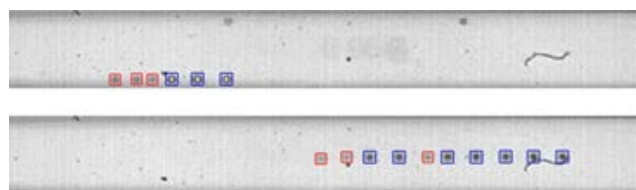


Fig. 5-8 Particle trains are identified at the centers of the channel front wall and of the channel bottom wall ( $Re = 112$ ,  $z/H = 1,000$ ,  $y/H = 0.5$ ). The 8.7- $\mu\text{m}$  and 5.3- $\mu\text{m}$  particles are encircled by blue and red squares, respectively.

### 5.3.1 Fraction of particles in trains

Three fractions of particles in trains are considered and their evolutions are studied as a function of  $Re$ , as shown in Fig. 5-9. The blue solid squares represent the fraction of 8.7- $\mu\text{m}$  particles in trains over all the 8.7- $\mu\text{m}$  particles, the red solid triangles represent the fraction of 5.3- $\mu\text{m}$  particles in trains over all the 5.3- $\mu\text{m}$  particles, and the black solid circles represent the fraction of all particles in trains over all the particles in the suspensions. The results are compared to those of two monodisperse suspensions: the monodisperse suspension of 8.7- $\mu\text{m}$  particle with  $\Phi = 0.1 \%$  and the monodisperse suspension of 5.3- $\mu\text{m}$  particle with  $\Phi = 0.02 \%$ . Considering that the bidisperse particle volume fraction  $\Phi$  is 0.05 % and 0.01 % for 8.7- $\mu\text{m}$  and 5.3- $\mu\text{m}$  particles, respectively, the same number of each type of particles is ensured in a given volume of suspension. Results for the two monodisperse suspensions are reprinted from the inset of Fig. 4-5a and are represented by the hollow markers and the non-solid lines as the corresponding fitting curves.

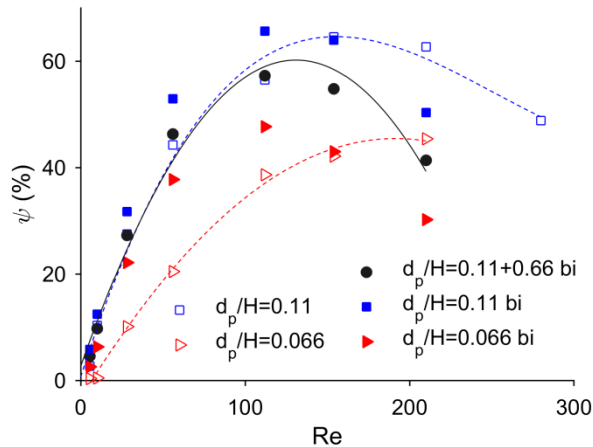


Fig. 5-9 Fraction of particles in trains as a function of  $Re$ , for bidisperse and monodisperse 8.7- $\mu\text{m}$  and 5.3- $\mu\text{m}$  particles.

The blue solid squares are always higher than the red solid triangles as expected, showing that in bidisperse particle suspensions, the large particles are more capable of forming trains than the small ones. This is similar to the results obtained for monodisperse suspensions as discussed in section 4.2.2.

When  $Re$  is smaller than 150, the fraction of 8.7- $\mu\text{m}$  particles in trains is higher than that in monodisperse suspension. The same phenomenon is seen for the 5.3- $\mu\text{m}$  particles even with a greater enhancement on the bidisperse curve with respect to the monodisperse one. We can thus conclude that the bidispersity enhances the formation of trains for both particle sizes but more strongly for the small ones. The enhancement of train formation of both sizes of particles could be linked to the enhancement of the migration process since the formation of trains is constrained by the presence of the particles on their equilibrium positions. The more developed is the migration, the more particles are on their equilibrium positions, the more trains can form. However, this assumption has to be confirmed by additional experimental investigation on the focusing degree of particles in bidisperse suspensions, as no clear conclusion could be drawn on the preliminary and partial results presented in section 5.2.4.

The fact that the formation of trains is more enhanced for the small particles than for the large ones suggests that the presence of large particles promotes the self-assembling of small ones. This could be explained by the larger reversing streamline zones generated by the large particles that might more easily slow down and capture particles.

The curves for both sizes of particles in bidisperse suspensions reach their maxima around  $Re = 112$  whereas those for the 8.7- $\mu\text{m}$  and 5.3- $\mu\text{m}$  particles in monodisperse suspensions reach their maximum at  $Re$  around 154 and 210, respectively. Furthermore, for Reynolds numbers higher than 112, the fractions of particles in trains for both sizes of particles in bidisperse suspension decrease in the same manner and more acutely than in monodisperse suspension. We can thus conclude that the bidispersity affects the longitudinal self-ordering process in enhancing and accelerating the train formation during the lateral migration process and in enhancing the reduction of trains for higher Reynolds numbers.

The fraction of particles in trains as a function of  $Re_p$  is presented in Fig. 5-10. For monodisperse particles, the train formation is controlled by  $Re_p$ , since the two dashed curves collapse quite well to a single curve (see section 4.2.1 for detailed discussion). The data overlap disappears showing that in bidisperse suspension,  $Re_p$  is no more a scaling factor.

Moreover, at  $Re_p < 0.5$ , the fraction of particles in trains for 5.3- $\mu\text{m}$  particles is always higher than that for the 8.7- $\mu\text{m}$  particles, confirming that the effect of dispersity on train formation (enhancement) is stronger on the small particles than on the large ones.

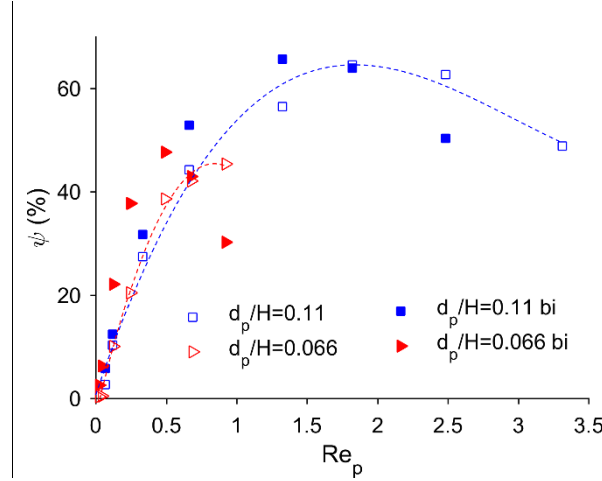


Fig. 5-10 Fraction of particles in trains as a function of  $Re_p$ , for bidisperse and monodisperse particles and monodisperse 8.7- $\mu\text{m}$  and 5.3- $\mu\text{m}$  particles.

### 5.3.2 Sequential ordering

We have observed in Fig. 5-8 that the trains are composed of both particles. In fact, there are three types of particle trains in the suspension: some composed solely of 8.7- $\mu\text{m}$  particles, some composed solely of 5.3- $\mu\text{m}$  particles and the others composed of mixed particles. Moreover, mixed trains show a sequential ordering: most of them begin with large particles and end with small ones, as illustrated in Fig. 5-11. Note that the large particles in the image are not exactly of the same size, because our 8.7- $\mu\text{m}$  particles have a high standard deviation ( $\sim 0.89 \mu\text{m}$ ).

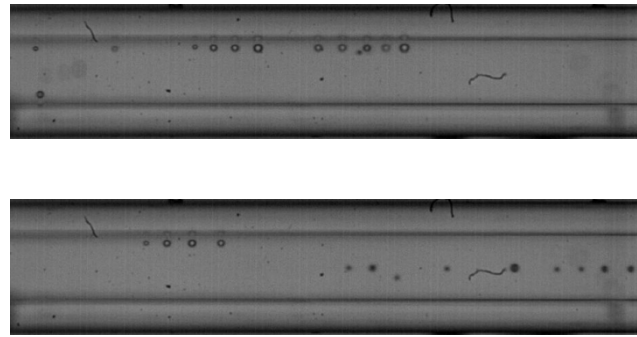


Fig. 5-11 Examples of bidisperse particle trains, often beginning with a large particle and ending with a small one. ( $Re = 112$ )

A statistical analysis has been carried out to extract the fraction of trains beginning with large particles and the fraction of trains ending with small particles. The results for different  $Re$  are shown in Fig. 5-12.

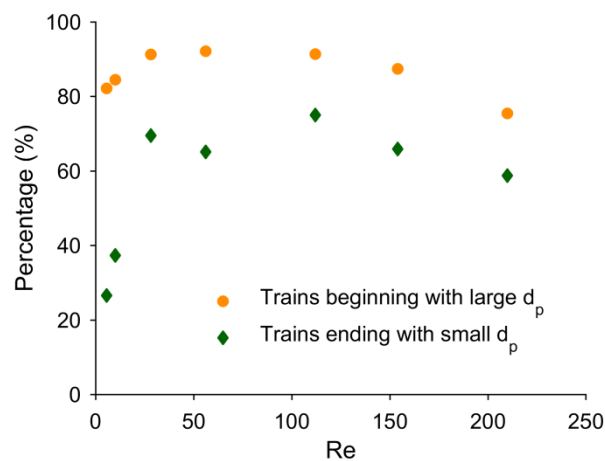


Fig. 5-12 Fraction of trains beginning with large particles and the fraction of trains ending with small particles as a function of  $Re$ .

Over 80 % of the particle trains begin with the large particles in the studied range of  $Re$ , and this fraction is even up to 94.48 % at  $Re = 56$ . This might be due to the big reversing streamline region created by the large particles, which makes it easier to slow down a following particle, and to capture it to form a particle pair. The fraction of trains ending with small particles is over 60 % at a relative high flow rate ( $Re > 30$ ). This could be explained by the fact that small particles with small inertia are much easily slowed down and then captured by the leading

particle.

The percentage of trains ending with a small particle is low at small  $Re$ : it is less than 40 % for Reynolds numbers smaller than 28. As small particles need a higher distance from channel inlet to reach their equilibrium position, it is evident that fewer small particles than large particle are present on the four equilibrium positions for small Reynolds numbers and thus fewer small particles can be caught in trains.

Finally, both the percentages of trains with large particle at the head and small particle at the end drop from  $Re \sim 112$ , indicating that the train ordering is less regular. This might be linked to the decrease of the fraction of particles in trains at the same  $Re \sim 112$  (Fig. 5-9). It seems that above a critical Reynolds number, particle flows become less ordered with fewer particles on their equilibrium positions, fewer particles in trains and more irregular trains.

### 5.3.3 Interparticle spacing

The interparticle spacing taken into account in this section is the distance between two adjacent particles whatever their sizes. Fig. 5-13 shows the interparticle spacing in the bidisperse particle suspension (black solid circles) as a function of  $Re$ . Blue open squares and red open triangles are reprinted from Fig. 4-5b, corresponding respectively to the 8.7- $\mu\text{m}$  and 5.3- $\mu\text{m}$  monodisperse particles.

The evolution of the interparticle spacing in the case of bidisperse particles is similar to those of the interparticle spacing in the case of monodisperse particles. It is however slightly smaller for all the studied Reynolds numbers.

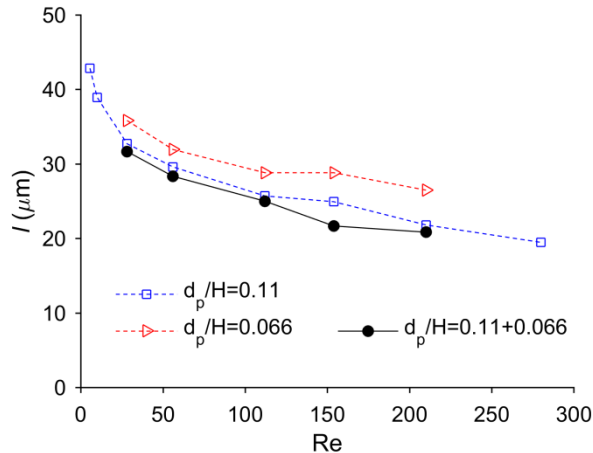


Fig. 5-13 Mean interparticle spacing for bidisperse particles as a function of  $Re$ , compared to the interparticle spacings for 8.7- $\mu\text{m}$  and 5.3- $\mu\text{m}$  monodisperse particles.

To better understand this intriguing phenomenon, we examined the distance between the different particles forming a train in several given mixed trains. Fig 6-14 illustrates the measurement of the distance between two 8.7- $\mu\text{m}$  particles (blue square), that between two 5.3- $\mu\text{m}$  particles (red triangle), and that between two particles of different sizes (black solid circle) in a mixed train taken for example. These distances are compared to the mean interparticle distances for 8.7- $\mu\text{m}$  monodisperse particle trains and 5.3- $\mu\text{m}$  monodisperse particle trains, under the same flow conditions ( $Re = 210$ ).

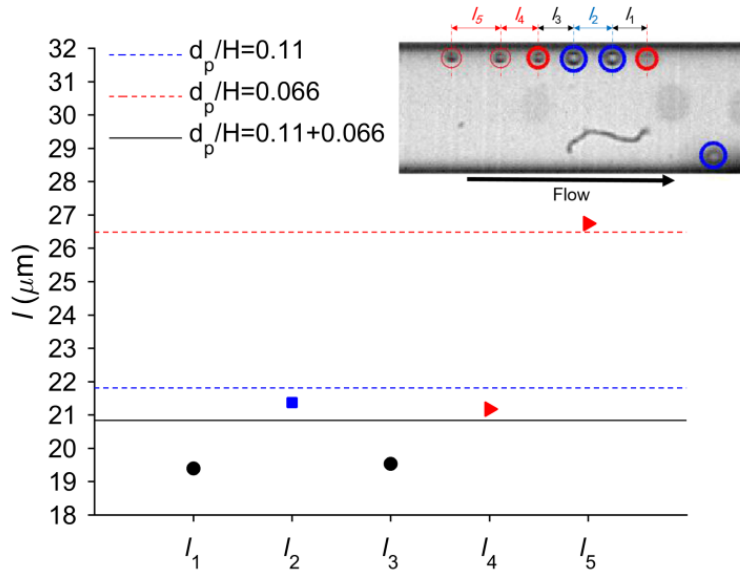


Fig 6-14 Distance between two 8.7- $\mu\text{m}$  particles (blue square), that between two 5.3- $\mu\text{m}$  particles (red triangle), and that between the two particles of different sizes (black spot) in a mixed bidisperse particle train. ( $Re = 210$ ) Dotted lines correspond to the interparticle distances observed in a monodisperse suspension of 5.3- $\mu\text{m}$  particles (red line) and 8.7- $\mu\text{m}$  particles (blue line). The black solid line gives the average interparticle distance in the bidisperse suspension.

We find that the interparticle distances for 8.7- $\mu\text{m}$  particles either in monodisperse or in bidisperse suspensions are very close. The two distances for 5.3- $\mu\text{m}$  particles in bidisperse suspension seen on this example are very different:  $l_5$  located between the last two particles is very close to that in monodisperse suspension but  $l_4$  located between two particles in the center of the train is smaller than it. This suggests that the location of particles inside a train impact their interparticle distance. Finally, the distance between two particles of different sizes are much smaller than the two monodisperse interparticle distances. The reason for this small distance between particles of different sizes is still elusive.

## 5.4 Summary

A preliminary empirical study has been carried out to characterize the effect of bidispersity on the inertial focusing behavior. 8.7- $\mu\text{m}$  ( $\Phi = 0.05 \%$ ) and 5.3- $\mu\text{m}$  particles ( $\Phi = 0.01 \%$ ) were mixed in a diluted suspension to ensure the same number of each particles in a given volume.

We found that the dispersity seems to have little effect on the particle migration at such a low concentration and in the studied range of Reynolds numbers:

- The equilibrium positions are identical in both bidisperse and monodisperse suspensions;
- Even if the focusing degree seemed to be slightly modified by the bidispersity in the few experiments that were performed, no clear conclusion can be drawn yet on the influence of this parameter on the migration process.

In contrast, we also found that the bidispersity seems to have a consequent impact on the longitudinal self-ordering of particles in the studied range of Reynolds numbers:

- Trains are composed either only of large particles, either only of small particles, or of both types of particles. The mixed trains frequently begin with a large particle and end with a small one;
- The formation of trains for particles of both sizes is enhanced and accelerated in bidisperse suspensions;
- The mean interparticle spacing is smaller in bidisperse suspensions. Further studies have to be conducted to confirm these preliminary observations and extend them to other sizes of particles and other experimental conditions.

Taking into account these conclusions, equilibrium separation of a mixture of 8.7- $\mu\text{m}$  and 5.3- $\mu\text{m}$  particles seems difficult to implement in a straight channel. Since particles migrate at moderate Reynolds numbers to very close equilibrium positions and form mixed trains, the separation is compromised once the particles are on their equilibrium position. However, kinetic separation could still be possible as large particles reach the four equilibrium position faster than the small ones and could thus be extracted firstly.



# Conclusions & Perspectives

## Conclusions

The main goal of the present thesis was to experimentally investigate the inertial focusing of spherical particles flowing in square straight microchannels.

Following a bibliographical study, mainly delving into the fundamental dynamics of the inertial migration and the different parameters that may influence the inertial migration, and a presentation of the experimental setups and data processing procedures used in this study, the essential of this thesis work has been presented in three main parts, concerning the inertial migration in monodisperse suspensions, the particle alignment, and the migration in bidisperse suspensions. The major conclusions are as follows:

- An *in situ* experimental setup based on classical microscopy has been developed to visualize the suspensions at different heights inside the microchannels and different distances from channel inlet. An in-house image analysis Matlab code has been developed to give access to the cross-sectional particle distributions all along the channel and next, to the inertial focusing evolution. The particle distributions in the channel cross section have also been confirmed using the particle projection method. Influences of Reynolds number, channel length, particle concentration and particle to channel size ratio on particle focusing have been studied in a wide range of  $Re$  (from 0.07 to 280).
- Three regimes of migration were observed in the flow conditions studied in this work, depending on the flow inertia.
  - At low flow inertia ( $Re < 1$  in our experimental conditions), particles migrate towards the channel centerline. This migration, which had never been reported in the literature, is very slow and long channels are needed for particles to reach the equilibrium positions.

- At moderate flow inertia ( $10 < Re < 280$  in our experimental conditions), particles migrate toward the centerlines of the channel faces within a two-stage process. Particles first migrate in the lateral direction to form an annulus parallel to the channel perimeter and then move cross-laterally parallel to the walls toward the four equilibrium positions near the center of each channel face. The second stage takes place only when the first one is fully developed, and is favored by larger  $Re$ , longer channels, and larger particle to channel size ratios.
- For Reynolds numbers ranging from 1 to 10, both regimes of migration coexist. Increasing the particle to channel size or the particle volume fraction shifts the transition between the two migration regimes towards higher Reynolds numbers.
- The longitudinal self-ordering of particles in flows of monodisperse suspensions has been studied through a statistical analysis of a large number of train images. The train formation process only starts when the particles have reached their equilibrium positions located near the centerline of each face. Fractions of particles in trains of up to 80% can be reached in some flow configurations. Increasing the particle Reynolds number  $Re_p$ , firstly favours the train formation, but leads to a diminution of the percentage of particles organized in trains over an optimal value of  $Re_p$ . Higher concentrations lead to a higher maximal value of this fraction and a smaller optimal value of  $Re_p$ . The distance between consecutive particle surfaces decreases when  $Re_p$  increases, independently of the particle concentration. However, if the concentration exceeds a threshold value linked to the flow confinement, the interparticle distance tends to decrease in relation with the concentration augmentation.
- Preliminary results of the effect of bidispersity on the inertial focusing have been obtained. Both lateral migration and longitudinal ordering have been studied using the in situ visualization method, in a range of  $Re$  from 5.6 to 210. The bidispersity is found to have little effect on the particle migration in the studied flow conditions, but it is found to favour acutely the train formation process. Moreover the observed trains were,

for a large majority, mixed trains, frequently beginning with a large particle and ending with a small one. The formation of trains for particles of both sizes is enhanced and accelerated in the bidisperse suspensions.

## Perspectives

The long time goal of this project is to predict the trajectories of microorganisms flowing in microchannels. Several tasks with increasing complexity have been identified to reach this objective. In the present thesis, inertial focusing of rigid spheres in monodisperse dilute suspension has been studied. The trajectories of non-spherical particles, deformable ones and even selected microorganisms, in dilute and moderately concentrated suspensions will be addressed in the forthcoming works.

In a shorter term, the promising perspectives that could be developed in future works are the following:

- It has been reported in the literature that particles tend also to migrate to the four corners of square channels, in addition to the four existing equilibrium lines near the face centers, when the Reynolds number  $Re$  is greater than 260. This could be a possible explanation of the unexpected behavior that we observed in our experiments at  $Re = 280$  (cf. section 3.1.6). Additional experiments in a higher range of Reynolds numbers would be necessary to confirm the existence of this migration regime and to identify the transition limits between the different regimes.
- The number of particles in trains and the robustness of the trains formed during monodisperse inertial focusing are still unstudied. These parameters however can affect separation processes and should thus be investigated.
- The train formation in rectangular channels has only been preliminarily studied in this thesis. Future works could be carried out with different aspect ratios to reveal the influence of this parameter.

- The experiments conducted with bidisperse suspensions should be repeated to confirm the obtained results and extend them to a higher range of Reynolds numbers, various particle concentrations and different confinements.

# Bibliography

- Abbas M, Magaud P, Gao Y, Geoffroy S (2014) Migration of finite sized particles in a laminar square channel flow from low to high Reynolds numbers. *Physics of Fluids* 26:123301
- Adamczyk A, Rimai L (1988) 2-Dimensional particle tracking velocimetry (PTV): technique and image processing algorithms. *Experiments in fluids* 6:373-380
- Altobelli SA, Fukushima E, Mondy LA (1997) Nuclear magnetic resonance imaging of particle migration in suspensions undergoing extrusion. *Journal of Rheology* 41:1105-1115
- Altobelli SA, Givler RC, Fukushima E (1991) Velocity and concentration measurements of suspensions by nuclear magnetic resonance imaging. *Journal of Rheology* 35:721-734
- Amini H, Lee W, Di Carlo D (2014) Inertial microfluidic physics. *Lab Chip* 14:2739-2761
- Andersson SR, Rasmussen A (2000) Flow measurements on a turbulent fiber suspension by laser Doppler anemometry. *AIChE Journal* 46:1106-1119
- Asmolov ES (1999) The inertial lift on a spherical particle in a plane Poiseuille flow at large channel Reynolds number. *Journal of Fluid Mechanics* 381:63-87
- Ayliffe HE, Frazier AB, Rabbitt RD (1999) Electric impedance spectroscopy using microchannels with integrated metal electrodes. *Journal of Microelectromechanical systems* 8:50-57
- Ayrancı I, Pinguet G, Escudié D, Selçuk N, Vaillon R, André F (2007) Effect of particle polydispersity on particle concentration measurement by using laser Doppler anemometry. *Experimental Thermal and Fluid Science* 31:839-847
- Bachalo W (1994) Experimental methods in multiphase flows. *International Journal of Multiphase Flow* 20:261-295
- Barrot Lattes C, Newport D, Chiavaroli S, Luca Morini G, Baldas L, Colin S (2008) 3-D reconstruction of velocity profiles in rectangular microchannels. *International Journal of Heat and Technology* 26:153-159
- Berland KM, So P, Gratton E (1995) Two-photon fluorescence correlation spectroscopy: method and application to the intracellular environment. *Biophysical Journal* 68:694-701
- Besseling R, Isa L, Weeks ER, Poon WC (2009) Quantitative imaging of colloidal flows. *Adv Colloid Interface Sci* 146:1-17
- Bhagat AA, Kuntaegowdanahalli SS, Papautsky I (2008a) Continuous particle separation in spiral microchannels using Dean flows and differential migration. *Lab Chip* 8:1906-1914

- Bhagat AAS, Kuntaegowdanahalli SS, Papautsky I (2008b) Enhanced particle filtration in straight microchannels using shear-modulated inertial migration. *Physics of Fluids* 20:101702
- Bhagat AAS, Kuntaegowdanahalli SS, Papautsky I (2008c) Inertial microfluidics for continuous particle filtration and extraction. *Microfluidics and Nanofluidics* 7:217-226
- Bonn D, Rodts S, Groenink M, Rafaï S, Shahidzadeh-Bonn N, Coussot P (2008) Some Applications of Magnetic Resonance Imaging in Fluid Mechanics: Complex Flows and Complex Fluids. *Annual Review of Fluid Mechanics* 40:209-233
- Brister PC, Kuricheti KK, Buschmann V, Weston KD (2005) Fluorescence correlation spectroscopy for flow rate imaging and monitoring--optimization, limitations and artifacts. *Lab Chip* 5:785-791
- Brown JR, Fridjonsson EO, Seymour JD, Codd SL (2009) Nuclear magnetic resonance measurement of shear-induced particle migration in Brownian suspensions. *Physics of Fluids* 21:093301
- Butler JE, Bonnecaze RT (1999) Imaging of particle shear migration with electrical impedance tomography. *Physics of Fluids* 11:1982-1994
- Caprihan A, Fukushima E (1990) Flow measurements by NMR. *Physics reports* 198:195-235
- Chen Z, Milner TE, Dave D, Nelson JS (1997) Optical Doppler tomographic imaging of fluid flow velocity in highly scattering media. *Optics letters* 22:64-66
- Choi S, Karp JM, Karnik R (2012) Cell sorting by deterministic cell rolling. *Lab Chip* 12:1427-1430
- Choi S, Park J-K (2008) Sheathless hydrophoretic particle focusing in a microchannel with exponentially increasing obstacle arrays. *Analytical chemistry* 80:3035-3039
- Choi S, Song S, Choi C, Park JK (2007) Continuous blood cell separation by hydrophoretic filtration. *Lab Chip* 7:1532-1538
- Choi YS, Seo KW, Lee SJ (2011) Lateral and cross-lateral focusing of spherical particles in a square microchannel. *Lab Chip* 11:460-465
- Christopher DA, Burns PN, Starkoski BG, Foster FS (1997) A high-frequency pulsed-wave Doppler ultrasound system for the detection and imaging of blood flow in the microcirculation. *Ultrasound in medicine & biology* 23:997-1015
- Chun B, Ladd A (2006) Inertial migration of neutrally buoyant particles in a square duct: An investigation of multiple equilibrium positions. *Physics of Fluids* 18:031704
- Ciftlik AT, Ettori M, Gijs MA (2013) High throughput-per-footprint inertial focusing. *Small* 9:2764-2773, 2828

- Cox R, Mason S (1971) Suspended particles in fluid flow through tubes. *Annual Review of Fluid Mechanics* 3:291-316
- David C, Pignon F, Narayanan T, Sztucki M, Gésan-Guiziou G, Magnin A (2008) Spatial and temporal in situ evolution of the concentration profile during casein micelle ultrafiltration probed by small-angle X-ray scattering. *Langmuir* 24:4523-4529
- Derk D, Wisman H, Blaaderen Av, Imhof A (2004) Confocal microscopy of colloidal dispersions in shear flow using a counter-rotating cone–plate shear cell. *Journal of Physics: Condensed Matter* 16:S3917-S3927
- Devendra R, Drazer G (2012) Gravity driven deterministic lateral displacement for particle separation in microfluidic devices. *Anal Chem* 84:10621-10627
- Di Carlo D (2009) Inertial microfluidics. *Lab Chip* 9:3038-3046
- Di Carlo D, Edd JF, Humphry KJ, Stone HA, Toner M (2009) Particle segregation and dynamics in confined flows. *Phys Rev Lett* 102:094503
- Di Carlo D, Irimia D, Tompkins RG, Toner M (2007) Continuous inertial focusing, ordering, and separation of particles in microchannels. *Proceedings of the National Academy of Sciences* 104:18892-18897
- Di Leonardo R, Leach J, Mushfique H, Cooper JM, Ruocco G, Padgett MJ (2006) Multipoint holographic optical velocimetry in microfluidic systems. *Phys Rev Lett* 96:134502
- Dinsmore AD, Weeks ER, Prasad V, Levitt AC, Weitz DA (2001) Three-dimensional confocal microscopy of colloids. *Applied optics* 40:4152-4159
- Edd JF, Di Carlo D, Humphry KJ, Koster S, Irimia D, Weitz DA, Toner M (2008) Controlled encapsulation of single-cells into monodisperse picolitre drops. *Lab Chip* 8:1262-1264
- Elsinga GE, Scarano F, Wieneke B, van Oudheusden BW (2006) Tomographic particle image velocimetry. *Experiments in Fluids* 41:933-947
- Faivre M, Abkarian M, Bickraj K, Stone HA (2006) Geometrical focusing of cells in a microfluidic device: an approach to separate blood plasma. *Biorheology* 43:147-159
- Feng J, Hu HH, Joseph DD (1994a) Direct simulation of initial value problems for the motion of solid bodies in a Newtonian fluid Part 1. Sedimentation. *Journal of Fluid Mechanics* 261:95-134
- Feng J, Hu HH, Joseph DD (1994b) Direct simulation of initial value problems for the motion of solid bodies in a Newtonian fluid. Part 2. Couette and Poiseuille flows. *Journal of fluid mechanics* 277:271-301
- Frank M, Anderson D, Weeks ER, Morris JF (2003) Particle migration in pressure-driven flow of a Brownian suspension. *Journal of Fluid Mechanics* 493:363-378

- Fukushima E (1999) Nuclear magnetic resonance as a tool to study flow. Annual review of fluid mechanics 31:95-123
- Gascoyne PR, Vykoukal J (2002) Particle separation by dielectrophoresis. Electrophoresis 23:1973
- Gossett DR, Tse HT, Dudani JS, Goda K, Woods TA, Graves SW, Di Carlo D (2012) Inertial manipulation and transfer of microparticles across laminar fluid streams. Small 8:2757-2764
- Haddadi H, Morris JF (2015) Topology of pair-sphere trajectories in finite inertia suspension shear flow and its effects on microstructure and rheology. Physics of Fluids 27:043302
- Han M, Kim C, Kim M, Lee S (1999) Particle migration in tube flow of suspensions. Journal of Rheology 43:1157-1174
- Hashmi SM, Loewenberg M, Dufresne ER (2007) Spatially extended FCS for visualizing and quantifying high-speed multiphase flows in microchannels. Optics express 15:6528-6533
- Heindel TJ (2011) A review of X-ray flow visualization with applications to multiphase flows. Journal of Fluids Engineering 133:074001
- Heindel TJ, Gray JN, Jensen TC (2008) An X-ray system for visualizing fluid flows. Flow Measurement and Instrumentation 19:67-78
- Hibiki T, Mishima K, Yoneda K, Fujine S, Tsuruno A, Matsabayashi M (1994) Visualization of fluid phenomena using a high frame-rate neutron radiography with a steady thermal neutron beam. Nuclear Instruments and Methods in Physics Research Section A: Accelerators, Spectrometers, Detectors and Associated Equipment 351:423-436
- Hinds KA et al. (2003) Highly efficient endosomal labeling of progenitor and stem cells with large magnetic particles allows magnetic resonance imaging of single cells. Blood 102:867-872
- Ho B, Leal L (1974) Inertial migration of rigid spheres in two-dimensional unidirectional flows. Journal of fluid mechanics 65:365-400
- Howell PB, Jr., Golden JP, Hilliard LR, Erickson JS, Mott DR, Ligler FS (2008) Two simple and rugged designs for creating microfluidic sheath flow. Lab Chip 8:1097-1103
- Huang LR, Cox EC, Austin RH, Sturm JC (2004) Continuous particle separation through deterministic lateral displacement. Science 304:987-990
- Huh D et al. (2007) Gravity-driven microfluidic particle sorting device with hydrodynamic separation amplification. Analytical chemistry 79:1369-1376
- Humphry KJ, Kulkarni PM, Weitz DA, Morris JF, Stone HA (2010) Axial and lateral particle ordering in finite Reynolds number channel flows. Physics of Fluids 22:081703

- Hur SC, Choi S-E, Kwon S, Carlo DD (2011a) Inertial focusing of non-spherical microparticles. *Applied Physics Letters* 99:044101
- Hur SC, Henderson-MacLennan NK, McCabe ER, Di Carlo D (2011b) Deformability-based cell classification and enrichment using inertial microfluidics. *Lab Chip* 11:912-920
- Hur SC, Mach AJ, Di Carlo D (2011c) High-throughput size-based rare cell enrichment using microscale vortices. *Biomicrofluidics* 5:22206
- Hur SC, Tse HT, Di Carlo D (2010) Sheathless inertial cell ordering for extreme throughput flow cytometry. *Lab Chip* 10:274-280
- Inoué S, Spring KR (1997) Video microscopy: The fundamentals (The language of science). Plenum, New York,
- Isa L, Besseling R, Weeks ER, Poon WCK (2006) Experimental studies of the flow of concentrated hard sphere suspensions into a constriction. *Journal of Physics: Conference Series* 40:124-132
- Kahkeshani S, Haddadi H, Di Carlo D (2016) Preferred interparticle spacings in trains of particles in inertial microchannel flows. *J Fluid Mech* 786:R3
- Keane R, Adrian R, Zhang Y (1995) Super-resolution particle imaging velocimetry. *Measurement Science and Technology* 6:754
- Kikura H, Matsushita J, Matsuzaki M, Kobayashi Y, Aritomi M (2004) Thermal behaviour and particle size evaluation of primary clusters in a water-based magnetic fluid. *Science and Technology of Advanced Materials* 5:703-707
- Kim J, Lee J, Wu C, Nam S, Di Carlo D, Lee W (2016) Inertial focusing in non-rectangular cross-section microchannels and manipulation of accessible focusing positions. *Lab Chip* 16:992-1001
- Kim YW, Yoo JY (2008) The lateral migration of neutrally-buoyant spheres transported through square microchannels. *Journal of Micromechanics and Microengineering* 18:065015
- Kloosterman A, Poelma C, Westerweel J (2010) Flow rate estimation in large depth-of-field micro-PIV. *Experiments in Fluids* 50:1587-1599
- Koh CJ, Hookham P, Leal L (1994) An experimental investigation of concentrated suspension flows in a rectangular channel. *Journal of Fluid Mechanics* 266:1-32
- Kulkarni PM, Morris JF (2008a) Pair-sphere trajectories in finite-Reynolds-number shear flow. *Journal of Fluid Mechanics* 596
- Kulkarni PM, Morris JF (2008b) Suspension properties at finite Reynolds number from simulated shear flow. *Physics of Fluids* 20:040602
- Lafforgue-Baldas C, Magaud P, Schmitz P, Zhihao Z, Geoffroy S, Abbas M (2013) Study of

- Microfocusing Potentialities to Improve Bioparticle Separation Processes: Towards an Experimental Approach. *Journal of Flow Chemistry* 3:92-98
- Lee G-B, Chang C-C, Huang S-B, Yang R-J (2006) The hydrodynamic focusing effect inside rectangular microchannels. *Journal of Micromechanics and Microengineering* 16:1024-1032
- Lee H, Yoon T-J, Figueiredo J-L, Swirski FK, Weissleder R (2009) Rapid detection and profiling of cancer cells in fine-needle aspirates. *Proceedings of the National Academy of Sciences* 106:12459-12464
- Lee W, Amini H, Stone HA, Di Carlo D (2010) Dynamic self-assembly and control of microfluidic particle crystals. *Proc Natl Acad Sci U S A* 107:22413-22418
- Lim EJ, Ober TJ, Edd JF, McKinley GH, Toner M (2012) Visualization of microscale particle focusing in diluted and whole blood using particle trajectory analysis. *Lab Chip* 12:2199-2210
- Lima R, Ishikawa T, Imai Y, Takeda M, Wada S, Yamaguchi T (2009) Measurement of individual red blood cell motions under high hematocrit conditions using a confocal micro-PTV system. *Annals of biomedical engineering* 37:1546-1559
- Lindken R, Westerweel J, Wieneke B (2006) Stereoscopic micro particle image velocimetry. *Experiments in Fluids* 41:161-171
- Liu C, Stakenborg T, Peeters S, Lagae L (2009) Cell manipulation with magnetic particles toward microfluidic cytometry. *Journal of Applied Physics* 105:102014
- Loth E, Dorgan AJ (2009) An equation of motion for particles of finite Reynolds number and size. *Environmental Fluid Mechanics* 9:187-206
- Loutherback K, Chou KS, Newman J, Puchalla J, Austin RH, Sturm JC (2010) Improved performance of deterministic lateral displacement arrays with triangular posts. *Microfluidics and Nanofluidics* 9:1143-1149
- Lumma D, Best A, Gansen A, Feuillebois F, Radler JO, Vinogradova OI (2003) Flow profile near a wall measured by double-focus fluorescence cross-correlation. *Phys Rev E Stat Nonlin Soft Matter Phys* 67:056313
- Lyon M, Leal L (1998a) An experimental study of the motion of concentrated suspensions in two-dimensional channel flow. Part 1. Monodisperse systems. *Journal of Fluid Mechanics* 363:25-56
- Lyon M, Leal L (1998b) An experimental study of the motion of concentrated suspensions in two-dimensional channel flow. Part 2. Bidisperse systems. *Journal of Fluid Mechanics* 363:57-77
- Maas H, Gruen A, Papantoniou D (1993) Particle tracking velocimetry in three-dimensional

- flows. *Experiments in Fluids* 15:133-146
- Mach AJ, Di Carlo D (2010) Continuous scalable blood filtration device using inertial microfluidics. *Biotechnol Bioeng* 107:302-311
- Mach AJ, Kim JH, Arshi A, Hur SC, Di Carlo D (2011) Automated cellular sample preparation using a Centrifuge-on-a-Chip. *Lab Chip* 11:2827-2834
- Magde D, Elson E, Webb WW (1972) Thermodynamic Fluctuations in a Reacting System—Measurement by Fluorescence Correlation Spectroscopy. *Physical Review Letters* 29:705-708
- Majors PD, Givler R, Fukushima E (1989) Velocity and concentration measurements in multiphase flows by NMR. *Journal of Magnetic Resonance* (1969) 85:235-243
- Manneville S (2008) Recent experimental probes of shear banding. *Rheologica Acta* 47:301-318
- Manneville S, Bécu L, Colin A (2004) High-frequency ultrasonic speckle velocimetry in sheared complex fluids. *The European Physical Journal Applied Physics* 28:361-373
- Martel JM, Toner M (2013) Particle Focusing in Curved Microfluidic Channels. *Scientific Reports* 3
- Martel JM, Toner M (2014) Inertial focusing in microfluidics. *Annu Rev Biomed Eng* 16:371-396
- Maru K, Fujii Y (2010) Differential Laser Doppler Velocimeter With Enhanced Range for Small Wavelength Sensitivity by Using Cascaded Mach-Zehnder Interferometers. *Journal of Lightwave Technology* 28:1631-1637
- Masaeli M et al. (2012) Continuous Inertial Focusing and Separation of Particles by Shape. *Physical Review X* 2
- Matas J-P, Glezer V, Guazzelli É, Morris JF (2004a) Trains of particles in finite-Reynolds-number pipe flow. *Physics of Fluids* 16:4192-4195
- Matas J-P, Morris JF, Guazzelli É (2004b) Inertial migration of rigid spherical particles in Poiseuille flow. *Journal of Fluid Mechanics* 515:171-195
- Matas J, Morris J, Guazzelli E (2004c) Lateral forces on a sphere. *Oil & gas science and technology* 59:59-70
- McCarthy KL, Kerr WL (1998) Rheological characterization of a model suspension during pipe flow using MRI. *Journal of food engineering* 37:11-23
- Meinhart C, Wereley S, Gray M (2000) Volume illumination for two-dimensional particle image velocimetry. *Measurement Science and Technology* 11:809
- Meinhart CD, Wereley ST, Santiago JG (1999) PIV measurements of a microchannel flow.

Experiments in fluids 27:414-419

- Merlin A, Angly J, Daubersies L, Madeira C, Schoder S, Leng J, Salmon JB (2011) Time-resolved microfocused small-angle X-ray scattering investigation of the microfluidic concentration of charged nanoparticles. *Eur Phys J E Soft Matter* 34:58
- Mikulencak DR, Morris JF (2004) Stationary shear flow around fixed and free bodies at finite Reynolds number. *Journal of Fluid Mechanics* 520:215-242
- Miltenyi S, Müller W, Weichel W, Radbruch A (1990) High gradient magnetic cell separation with MACS. *Cytometry* 11:231-238
- Mishima K, Hibiki T (1998) Development of high-frame-rate neutron radiography and quantitative measurement method for multiphase flow research. *Nuclear Engineering and Design* 184:183-201
- Nakagawa N, Yabu T, Otomo R, Kase A, Makino M, Itano T, Sugihara-Seki M (2015) Inertial migration of a spherical particle in laminar square channel flows from low to high Reynolds numbers. *Journal of Fluid Mechanics* 779:776-793
- Nam J, Lim H, Kim D, Jung H, Shin S (2012) Continuous separation of microparticles in a microfluidic channel via the elasto-inertial effect of non-Newtonian fluid. *Lab Chip* 12:1347-1354
- Pamme N (2007) Continuous flow separations in microfluidic devices. *Lab Chip* 7:1644-1659
- Park JS, Choi CK, D. Kihm K (2004) Optically sliced micro-PIV using confocal laser scanning microscopy (CLSM). *Experiments in Fluids* 37:105-119
- Petersson F, Åberg L, Swärd-Nilsson A-M, Laurell T (2007) Free flow acoustophoresis: microfluidic-based mode of particle and cell separation. *Analytical chemistry* 79:5117-5123
- Poiseuille J (1836) Observations of blood flow. *Ann Sci Nat STrie* 5
- Powell RL (2008) Experimental techniques for multiphase flows. *Physics of Fluids* 20:040605
- Prasad V, Semwogerere D, Weeks ER (2007) Confocal microscopy of colloids. *Journal of Physics: Condensed Matter* 19:113102
- Raguin LG, Ciobanu L (2007) Multiple echo NMR velocimetry: fast and localized measurements of steady and pulsatile flows in small channels. *J Magn Reson* 184:337-343
- Reinecke N, Petritsch G, Boddem M, Mewes D (1998) Tomographic imaging of the phase distribution in two-phase slug flow. *International journal of multiphase flow* 24:617-634
- Rogers SS, Waigh TA, Zhao X, Lu JR (2007) Precise particle tracking against a complicated background: polynomial fitting with Gaussian weight. *Physical Biology* 4:220

- Rubinow S, Keller JB (1961) The transverse force on a spinning sphere moving in a viscous fluid. *Journal of Fluid Mechanics* 11:447-459
- Saffman P (1965) The lift on a small sphere in a slow shear flow. *Journal of fluid mechanics* 22:385-400
- Sandison DR, Webb WW (1994) Background rejection and signal-to-noise optimization in confocal and alternative fluorescence microscopes. *Applied optics* 33:603-615
- Santiago JG, Wereley ST, Meinhart CD, Beebe D, Adrian RJ (1998) A particle image velocimetry system for microfluidics. *Experiments in fluids* 25:316-319
- Schonberg JA, Hinch E (1989) Inertial migration of a sphere in Poiseuille flow. *Journal of Fluid Mechanics* 203:517-524
- Scott R, Sethu P, Harnett CK (2008) Three-dimensional hydrodynamic focusing in a microfluidic Coulter counter. *Rev Sci Instrum* 79:046104
- Segre G, Silberberg A (1962a) Behaviour of macroscopic rigid spheres in Poiseuille flow Part 1. Determination of local concentration by statistical analysis of particle passages through crossed light beams. *Journal of Fluid Mechanics* 14:115-135
- Segre G, Silberberg A (1962b) Behaviour of macroscopic rigid spheres in Poiseuille flow Part 2. Experimental results and interpretation. *Journal of fluid mechanics* 14:136-157
- Semwogerere D, Morris JF, Weeks ER (2007) Development of particle migration in pressure-driven flow of a Brownian suspension. *Journal of Fluid Mechanics* 581:437
- Seo J, Lean MH, Kole A (2007) Membrane-free microfiltration by asymmetric inertial migration. *Applied Physics Letters* 91:033901
- Stitou A, Riethmuller M (2001) Extension of PIV to super resolution using PTV. *Measurement Science and Technology* 12:1398
- Sugaya S, Yamada M, Seki M (2011) Observation of nonspherical particle behaviors for continuous shape-based separation using hydrodynamic filtration. *Biomicrofluidics* 5:24103
- Takenaka N, Fujii T, Ono A, Nakazawa T, Turuno A (1993) Application of neutron radiography to flow visualization.
- Tallarek U, Van Dusschoten D, Van As H, Bayer E, Guiochon G (1998) Study of transport phenomena in chromatographic columns by pulsed field gradient NMR. *The Journal of Physical Chemistry B* 102:3486-3497
- Tasadduq B, Wang G, El Banani M, Mao W, Lam W, Alexeev A, Sulchek T (2015) Three-dimensional particle tracking in microfluidic channel flow using in and out of focus diffraction. *Flow Measurement and Instrumentation* 45:218-224

- Thompson NL, Lieto AM, Allen NW (2002) Recent advances in fluorescence correlation spectroscopy. *Current opinion in structural biology* 12:634-641
- Uijttewaal WS, Nijhof E-J, Heethaar RM (1994) Lateral migration of blood cells and microspheres in two-dimensional Poiseuille flow: a laser-Doppler study. *Journal of biomechanics* 27:35-42
- Van Dinther A, Schroën C, Vergeldt F, Van der Sman R, Boom R (2012) Suspension flow in microfluidic devices—A review of experimental techniques focussing on concentration and velocity gradients. *Advances in colloid and interface science* 173:23-34
- Voigt A, Bayer C, Shirai K, Büttner L, Czarske J (2008) Laser Doppler field sensor for high resolution flow velocity imaging without camera. *Applied optics* 47:5028-5040
- Voldman J (2006) Electrical forces for microscale cell manipulation. *Annu Rev Biomed Eng* 8:425-454
- Wang T, Wang J, Ren F, Jin Y (2003) Application of Doppler ultrasound velocimetry in multiphase flow. *Chemical Engineering Journal* 92:111-122
- Webb RH (1996) Confocal optical microscopy. *Reports on Progress in Physics* 59:427
- Westerweel J (1997) Fundamentals of digital particle image velocimetry. *Measurement science and technology* 8:1379
- Williams R, Jia X (2003) Tomographic imaging of particulate systems. *Advanced Powder Technology* 14:1-16
- Williams SJ, Park C, Wereley ST (2010) Advances and applications on microfluidic velocimetry techniques. *Microfluidics and Nanofluidics* 8:709-726
- Winer MH, Ahmadi A, Cheung KC (2014) Application of a three-dimensional (3D) particle tracking method to microfluidic particle focusing. *Lab Chip* 14:1443-1451
- Wu C, Cheng Y, Ding Y, Wei F, Jin Y (2007) A novel X-ray computed tomography method for fast measurement of multiphase flow. *Chemical Engineering Science* 62:4325-4335
- Wu L, Guan G, Hou HW, Bhagat AAS, Han J (2012) Separation of leukocytes from blood using spiral channel with trapezoid cross-section. *Analytical chemistry* 84:9324-9331
- Xiang N, Yi H, Chen K, Sun D, Jiang D, Dai Q, Ni Z (2013) High-throughput inertial particle focusing in a curved microchannel: Insights into the flow-rate regulation mechanism and process model. *Biomicrofluidics* 7:44116
- Xuan X, Li D (2005) Focused electrophoretic motion and selected electrokinetic dispensing of particles and cells in cross-microchannels. *Electrophoresis* 26:3552-3560
- Yamanaka G, Kikura H, Takeda Y, Aritomi M (2003) Flow measurement on oscillating pipe flow near the entrance using the UVP method. *Experiments in Fluids* 34:307-315

- Yang R-J, Chang C-C, Huang S-B, Lee G-B (2005) A new focusing model and switching approach for electrokinetic flow inside microchannels. *Journal of Micromechanics and Microengineering* 15:2141-2148
- Yang S, Undar A, Zahn JD (2006) A microfluidic device for continuous, real time blood plasma separation. *Lab Chip* 6:871-880
- Zeng L, Najjar F, Balachandar S, Fischer P (2009) Forces on a finite-sized particle located close to a wall in a linear shear flow. *Physics of Fluids* 21:033302
- Zerrouki A (2012) Etude du phénomène de migration latérale de particules iso-densités dans des micro-canaux : Développement d'un dispositif expérimental. Master, Université Paul Sabatier
- Zhang J, Yan S, Yuan D, Alici G, Nguyen NT, Ebrahimi Warkiani M, Li W (2016) Fundamentals and applications of inertial microfluidics: a review. *Lab Chip* 16:10-34
- Zhao Y, Fujimoto BS, Jeffries GD, Schiro PG, Chiu DT (2007) Optical gradient flow focusing. *Optics express* 15:6167-6176
- Zhou J, Giridhar PV, Kasper S, Papautsky I (2013a) Modulation of aspect ratio for complete separation in an inertial microfluidic channel. *Lab Chip* 13:1919-1929
- Zhou J, Giridhar PV, Kasper S, Papautsky I (2014) Modulation of rotation-induced lift force for cell filtration in a low aspect ratio microchannel. *Biomicrofluidics* 8:044112
- Zhou J, Kasper S, Papautsky I (2013b) Enhanced size-dependent trapping of particles using microvortices. *Microfluid Nanofluidics* 15
- Zhou J, Papautsky I (2013) Fundamentals of inertial focusing in microchannels. *Lab Chip* 13:1121-1132
- Zhu J, Tzeng TR, Xuan X (2010) Continuous dielectrophoretic separation of particles in a spiral microchannel. *Electrophoresis* 31:1382-1388
- Zurita-Gotor M, BŁAwzdiewicz J, Wajnryb E (2007) Swapping trajectories: a new wall-induced cross-streamline particle migration mechanism in a dilute suspension of spheres. *Journal of Fluid Mechanics* 592



# Résumé

Cette thèse a pour objectif de mieux comprendre les mécanismes physiques qui contrôlent les trajectoires de particules dans des écoulements confinés, afin d'en améliorer la prédiction. Nous avons dans un premier temps développé des outils expérimentaux basés sur la microscopie et le traitement d'images afin d'analyser les positions de particules en écoulement confiné dans des microcanaux de section carrée. Ces outils ont ensuite permis l'obtention de résultats originaux sur la migration latérale de particules sphériques dans des écoulements faiblement inertiels. Nous avons montré en particulier que les particules migrent au centre du canal à faible nombre de Reynolds et à proximité du centre de chaque face à Reynolds plus élevé et que ces deux régimes co-existent pour des Reynolds intermédiaires. Parallèlement à leur migration latérale, les particules en écoulement confiné peuvent s'espacer régulièrement sous certaines conditions pour former des trains. Ce travail a donc consisté à mener une étude statistique pour quantifier et localiser la formation des trains. Il a été montré que la formation des trains était contrôlée par la configuration de l'écoulement dans le sillage des particules et que leurs caractéristiques, i.e., le pourcentage de particules en trains et la distance interparticulaire, étaient fonction du nombre de Reynolds particulaire. Enfin, des résultats préliminaires sur le cas d'écoulements bi-disperses ont été obtenus. Pour terminer, les perspectives et développements futurs de ce travail sont dégagés.

## Mots clés:

focalisation inertielle; microfluidique; interaction hydrodynamique; suspensions; microscopie